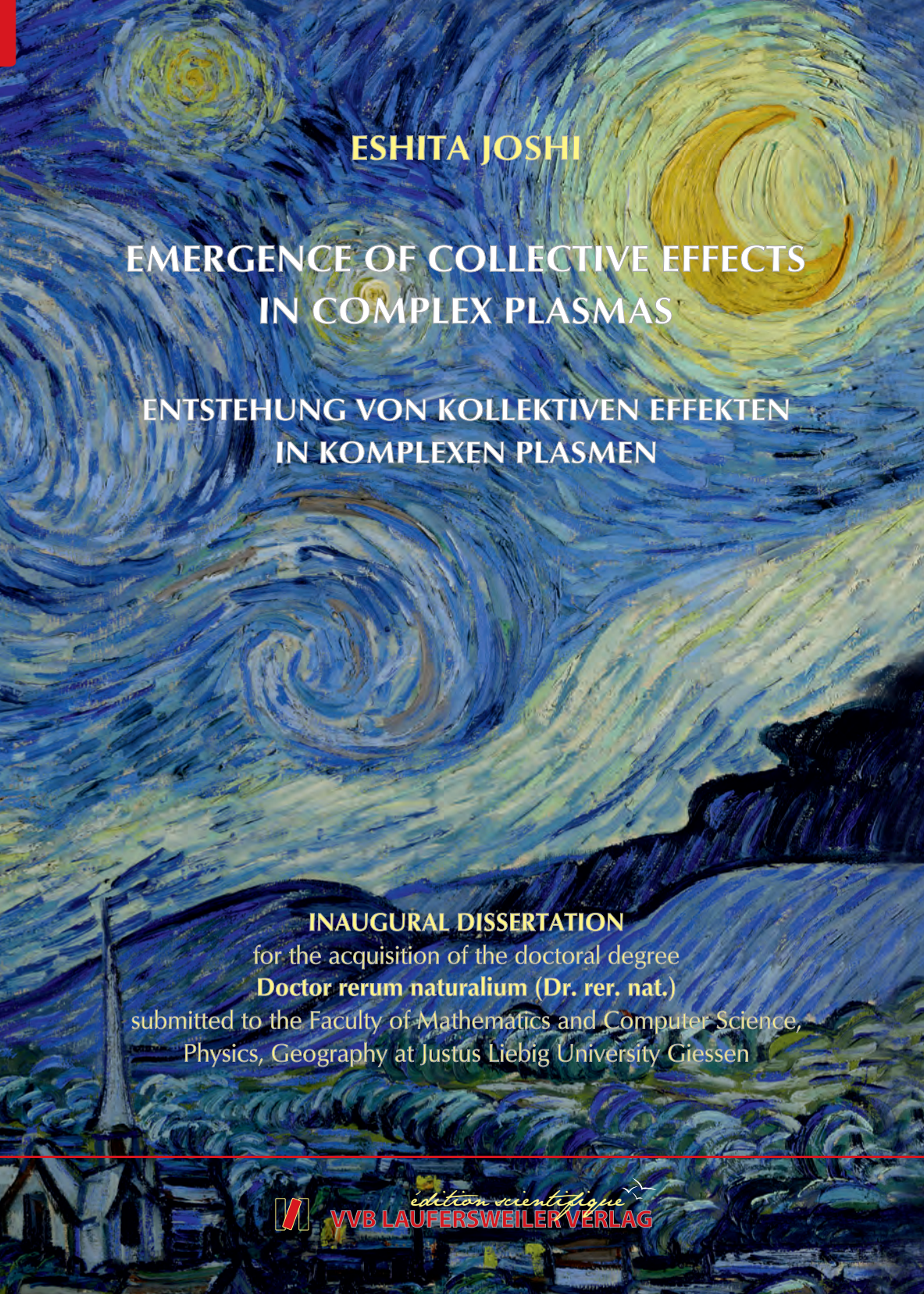

ESHITA JOSHI

EMERGENCE OF COLLECTIVE EFFECTS IN COMPLEX PLASMAS

ENTSTEHUNG VON KOLLEKTIVEN EFFEKTEN IN KOMPLEXEN PLASMEN

INAUGURAL DISSERTATION
for the acquisition of the doctoral degree
Doctor rerum naturalium (Dr. rer. nat.)
submitted to the Faculty of Mathematics and Computer Science,
Physics, Geography at Justus Liebig University Giessen

édition scientifique
VVB LAUFERSWEILER VERLAG

1. Auflage 2024

1st Edition 2024

Printed in Germany

édition scientifique
VVB LAUFERSWEILER VERLAG

STAUFENBERGRING 15, 35396 GIESSEN, GERMANY
Tel: 0641-5599888 Fax: 0641-5599890
email: redaktion@doktorverlag.de

www.doktorverlag.de

Emergence of collective effects in complex plasmas

Entstehung von kollektiven Effekten in komplexen Plasmen

INAUGURAL DISSERTATION

for the acquisition of the doctoral degree

Doctor rerum naturalium (Dr. rer. nat.)

submitted to the Faculty of Mathematics and Computer Science,

Physics, Geography at Justus Liebig University Giessen

by

Eshita Joshi

München, 2023

Examination Committee:

Herr Prof. Dr. Markus Thoma

Herr Prof. Dr. Hartmut Löwen

Herr Prof. Dr. Christoph Scheidenberger

Herr PD Dr. Bernd-Jochen Schaefer

Date of disputation: 17.10.2023

Zusammenfassung

In dieser Doktorarbeit wird die Entstehung von kollektiven Effekten in ionisierten Gasen mit eingebetteten Mikroteilchen, sogenannten komplexen Plasmen, untersucht. Diese werden häufig als Modellsysteme zur Untersuchung einer Vielzahl von emergenten Phänomenen verwendet, da die Teilchen groß genug sind, um direkt abgebildet zu werden.

Basierend auf kürzlich durchgeführten Experimenten in schwerelosen komplexen Plasmen, präsentiere Ich ein theoretisches Modell der Selbstbildung von Tröpfchen, welches den Ausgleich der Ionenwiderstandskraft mit elektrostatischer Abstoßung nutzt um die Bildung stabiler Tröpfchen in komplexen Plasmen zu erklären. Es liefert quantitative Ergebnisse für die Vorhersage der Größe eines stabilen Tröpfchens, die mit den experimentellen Beobachtungen übereinstimmen. Dieses Modell ermöglicht es erstmalig, anhand von Parametern komplexer Plasmen die Struktur und Größe von selbstformenden Tröpfchen vorherzusagen und umgekehrt aus der Größe eines Tröpfchens die Parameter des Plasmas, insbesondere die Elektronentemperatur, abzuleiten. Dies ermöglicht es, die Beobachtung von Tröpfchen als Diagnoseinstrument zur Bestimmung der Plasmaparameter in Experimenten einzusetzen.

Darüber hinaus untersuche ich in dieser Arbeit mit Hilfe von Simulationen komplexer Plasmaströmungen um ein kugelförmigen Hindernis weitere kollektive Flüssigkeitseffekte wie Stoßwellen und Turbulenz. Diese Doktorarbeit ist eine der ersten systematischen teilchenaufgelösten Untersuchungen der Turbulenz. In dieser zeige ich, dass die Bildung von Stoßwellen für das Einsetzen von Turbulenz in gedämpften Systemen notwendig ist. Durch die Simulation einer Überschallströmung können Stoßwellen wie Mach-Kegel und Bugschocks vor und hinter dem Hindernis wiederholbar erzeugt werden. Erstmalig demonstriere ich in dieser Arbeit die Entstehung doppelter Bugschocks, ähnlich wie sie in astrophysikalischen Plasmen beobachtet werden, in Simulationen von komplexen Plasmen. In Bereichen, in denen Partikel direkt in eine Schockfront hinein strömen, löst unter bestimmten Bedingungen die erhöhte Teilchenanzahldichte - und damit die größere Stärke der Wechselwirkungen - das Einsetzen von Turbulenz aus. Ich zeige, dass das Einsetzen von Turbulenz in den Simulationen von Parametern wie der Partikelladung und der Strömungsgeschwindigkeit abhängt. Durch Änderung eines dieser beiden Parameter konnte ich in zunächst laminaren Simulationen Turbulenz wiederholbar induzieren. Beide Parameter können experimentell kontrolliert werden, so dass die Simulationen das Auftreten von Turbulenz in komplexen Plasmen selbst unter dem Einfluss von Dämpfung vorhersagen und kontrollieren können.

Schließlich untersuche ich das Auftreten von elektrorheologischen Effekten durch die Bildung von „string-like clusters" (SLCs). Ich reproduziere mit Hilfe von Molekulardynamiksimulationen qualitativ Ergebnisse aus Mikrogravitationsexperimenten, die die Bildung, Zerstörung und Rekristallisation von Mikropartikel-SLCs zeigten. Ich verwende die Simulationen, um zu zeigen, dass keine effektive langreichweitige Anziehungskraft zwischen den Teilchen erforderlich ist, um SLCs zu bilden. Die ausgezeichnete qualitative Übereinstimmung zwischen Experiment und Simulation belegt, dass effektive langreichweitige Anziehung zwischen Teilchen keine Voraussetzung für elektrorheologische Effekte in komplexen Plasmen ist.

Insgesamt erweitert diese Arbeit das Wissen darüber, wie kollektive Effekte in komplexen Plasmen unter einer Vielzahl von Bedingungen entstehen.

Abstract

This work is dedicated to studying the emergence of collective effects in ionised gases with micrometre sized particles immersed in them, also known as complex plasmas. These are often used as model systems to study a variety of emergent phenomena since the particles are large enough to be imaged directly.

I present a theoretical model of the self-formation of droplets based on recent experiments performed in weightless complex plasmas. The model is based on balancing the ion drag force with electrostatic repulsion to explain the formation of stable droplets. It produces quantitative results that predict the size of a droplet as a function of the plasma parameters in agreement with the experimental observations. For the first time, this model causally connects the size of the droplet to plasma parameters (such as the electron temperature). Not only can the model predict what size and shape of droplets may form in the experiment given the parameters, but it can also determine the parameters from the size of the observed droplet. This allows the observation of droplets to be used as a diagnostic tool to determine plasma parameters in complex plasma experiments.

Beyond this, I investigate additional collective fluid effects such as the formation of shocks and the onset of turbulence by simulating a flow of microparticles past a spherical obstacle in a complex plasma. This work is one of the first systematic particle-resolved investigations of turbulence, in which I demonstrate that the formation of shocks is important for the onset of turbulence in damped systems. By simulating a supersonic flow, I can reliably generate Mach cones and bow shocks both up- and downstream of the obstacle. I report the observation of double bow shocks in these simulations for the first time in complex plasmas, showing a similar structure as observed in astrophysical plasmas. In regions where particles flow directly into a shock, the increased microparticle density - and hence, strength of interactions - triggers the onset of turbulence. This link between increased microparticle density and the onset of turbulence in damped fluids is in agreement with previous complex plasma experiments. I report that the onset of turbulence in the simulations depends on parameters such as particle charge and flow speed. A non-turbulent simulation can be made turbulent by changing one of these two parameters. Both of these parameters can be controlled in experiments, allowing the simulations to predict and control the onset of turbulence in complex plasma experiments even under the influence of damping, opening the pathway towards detailed studies of the onset and control of turbulence at the level of individual particles.

Finally, I study the onset of electrorheological effects through the formation of string-like clusters (SLCs) based on microgravity experiments. This process is led by the deformation of the ion shielding cloud around the particles due to an alternating ion flow. I mimic this in the simulations by placing a positive wake charge in-front of and behind the particle to modify the interparticle potential. By doing so, I can reproduce the formation, destruction, and recrystallisation of SLCs as seen in the experiments with qualitatively similar results. I test whether an effective long-range interparticle attraction is required to produce SLCs, and report that this is not the case. The excellent qualitative agreement between experiment and simulation is definitive proof that effective long-range interparticle attraction is not a necessity for electrorheological effects in complex plasmas.

Overall, this thesis advances the knowledge of emergent phenomena in complex plasmas in a variety of conditions. As complex plasma experiments can resolve individual particle dynamics, this work can be used to inform future investigations of collective effects at the particle-resolved level.

Declaration

I declare that I have completed this dissertation single-handedly without the unauthorised help of a second party and only with the assistance acknowledged therein. I have appropriately acknowledged and cited all text passages that are derived verbatim from or are based on the content of published work of others, and all information relating to verbal communications. I consent to the use of an anti-plagiarism software to check my thesis. I have abided by the principles of good scientific conduct laid down in the charter of the Justus Liebig University Gießen „Satzung der Justus-Liebig-Universität Gießen zur Sicherung guter wissenschaftlicher Praxis“ in carrying out the investigations described in the dissertation.

Erklärung

Ich erkläre: Ich habe die vorgelegte Dissertation selbstständig und ohne unerlaubte fremde Hilfe und nur mit den Hilfen angefertigt, die ich in der Dissertation angegeben habe. Alle Textstellen, die wörtlich oder sinngemäßaus veröffentlichten Schriften entnommen sind, und alle Angaben, die auf mündlichen Auskünften beruhen, sind als solche kenntlich gemacht. Ich stimme einer evtl. Überprüfung meiner Dissertation durch eine Antiplagiat-Software zu. Bei den von mir durchgeführten und in der Dissertation erwähnten Untersuchungen habe ich die Grundsätze guter wissenschaftlicher Praxis, wie sie in der „Satzung der Justus-Liebig-Universität Gießen zur Sicherung guter wissenschaftlicher Praxis“ niedergelegt sind, eingehalten.

Eshita Joshi, München 2023

Contents

Chapter 1

Introduction

"Plasma seems to have the kinds of properties one would like for life. It's somewhat like liquid water - unpredictable and thus able to behave in an enormously complex fashion. It could probably carry as much information as DNA does. It has at least the potential for organizing itself in interesting ways."

Freeman Dyson (1986) [1]

1.1 Complex plasmas

A *plasma* is the stuff that stars are made of. Lightning striking a tree is made of plasma. The flame of a hot fire, and a neon sign above a restaurant both contain plasmas. A plasma is simply a state of matter where an electron gets separated from a gas particle, resulting in a mix of free electrons and gas ions. This ionisation process results in a plasma that is overall electrically neutral as it has the same number of negatively charged electrons as it does positively charged ions. Despite this, due to the long-range interactions between electrons and ions, a plasma can be affected by electric and magnetic fields [2]. A gas can be ionised into a plasma at relatively low temperatures and pressures by applying an electric field, and this allows for applications in various fields of medicine and technology. Plasmas can be used not just in fusion reactors, but also in various medical treatments from sterilising wounds to tissue regeneration [3, 4], to enhance food quality and safety [5, 6], treatment of hazardous waste [7], and development of materials for solar cells and circuitry [8, 9].

A recurring problem across all uses of plasma technology is the problem of contamination by 'dust'. Any unwanted solid grains of matter that enter the system are referred to as 'dust', and can disturb or damage the system and render its application useless. Dust particles may cause damage to intricate integrated circuits or threaten the safety of a fusion reactor [10]. Particles in a reactor can often join together to form large agglomerates, which poses multiple safety hazards including the risk of triggering an explosion [11]. As dust particles increase in size, they collect a large quantity of electrons on their surfaces, which can strongly affect the performance of a fusion reactor by depleting electrons from the plasma. Furthermore, as the particles become highly negatively charged, they generate additional electric fields within the plasma and interfere with the plasma dynamics [12, 13].

The presence of dust in plasmas is thus a serious problem for fusion reactors. However, the properties that makes dust particles dangerous inside a fusion reactor also make them incredibly useful and interesting outside of it. In a protoplanetary disk, agglomeration processes that would

be a safety hazard in a fusion reactor can instead lead to planet formation [14, 15]. Plasmas with dust immersed in them, also known as *dusty plasmas*, are prevalent across the universe. They can be found in interstellar clouds (Fig. 1.1**a**) [16], comets [17], accretion disks [18], and even in the rings of Saturn [19] (Fig. 1.1**b**). Understanding the dynamics of dusty plasmas can not only help us solve the problems posed by dust in industrial applications, but also help us understand how planets and galaxies form.

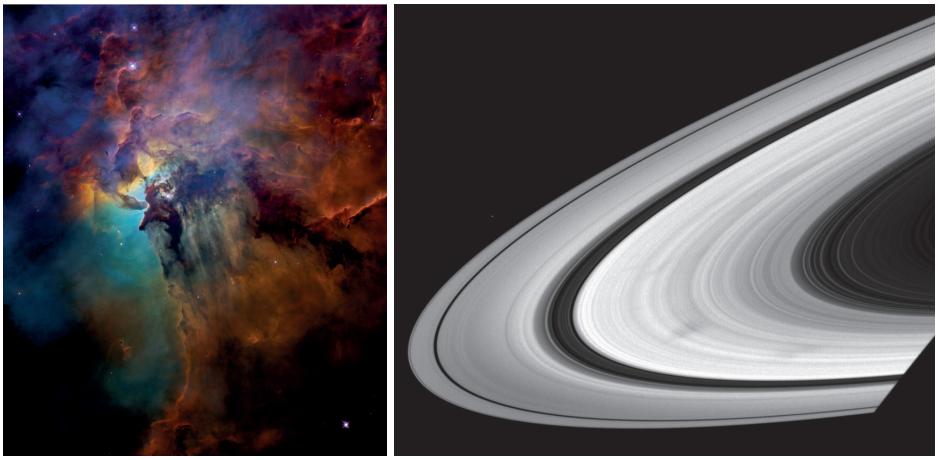

Figure 1.1: Dusty plasmas as seen in **a**) the Lagoon nebula, pictured by the Hubble Space Telescope [20] (Courtesy: NASA, ESA, and STScI), and **b**) spokes in Saturn's rings as seen by the Cassini-Huygens mission [19] (Courtesy: NASA/JPL/Space Science Institute).

The dynamics of dust in plasmas are made more interesting as the subsystem of particles can become strongly coupled due to their high negative charges. This can lead to fascinating collective behaviour as the dust particles form a complex system[1]. This can then be used to model and perform studies of condensed matter phenomena and complex collective behaviour. In laboratory conditions where properties of the dust particles such as shape, size, material, number density, and mass can be controlled, the plasmas are referred to as *complex plasmas*. The dust particles here are also known as *microparticles* as they are a few micrometres in diameter. These particles are big enough to be captured directly on camera as shown in Fig. 1.2. The ability to resolve each individual particle provides a unique advantage for studying various emergent behaviours and condensed matter phenomena. As it allows us to study such phenomena at the microcanonical level, we can investigate unsolved problems in physics, such as turbulence, at the level of individual particles with great detail.

[1]The use of the word 'complex' here does not mean 'complicated'. Instead, it indicates that the system is composed of multiple individual parts with nonlinear interactions that can self-organise and display collective behaviour.

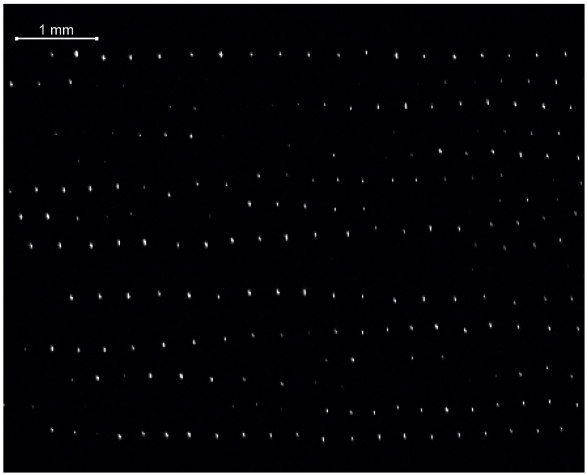

Figure 1.2: Picture of microparticles in the PK-4 chamber involving complex plasmas with argon gas at a pressure of $32\ \mathrm{Pa}$ with a particle diameter of $3.4\ \mu\mathrm{m}$. Each individual particle can be resolved by the camera as it reflects the light from the illumination laser. It should be noted that due to light scattering the size of the dots is larger than the particle diameter. From [21].

The field of complex plasmas combines plasma physics, condensed matter physics, and complexity science to understand how interactions between individual microparticles lead to larger scale emergent phenomena. The system of microparticles embedded in a low-temperature plasma is greater than the sum of its parts. The complexity in these systems is a result of many interparticle interactions, and the heart of the research lies in understanding how complexity in pattern and structure can emerge from simplicity in individual interactions. The collective behaviour of a flock of birds is exemplary of how simple rules governing individual birds can lead to surprising effects for the entire flock [22]. In the most basic model, each bird only follows two rules: 1. don't fly too far from your neighbours, and 2. don't fly too close to your neighbours[2]. The first rule ensures they don't get separated from the flock, and the second rule ensures they avoid collisions. Together, they form the rules determining the interaction between individual birds. Over many individual interactions, large-scale patterns emerge in the behaviour of the flock. Such a flock consisting of hundreds to thousands of birds is called a *murmuration* and looks like a shape-shifting entity that bends and turns and twists and swirls into many shapes as though it's alive. An exemplary photograph is presented in Fig. 1.3 showing emergent phenomena as the flock of birds behaves like a collective.

[2]Often, the simplest models also include a third rule which says that the birds must fly as close to the mean velocity of the flock as possible.

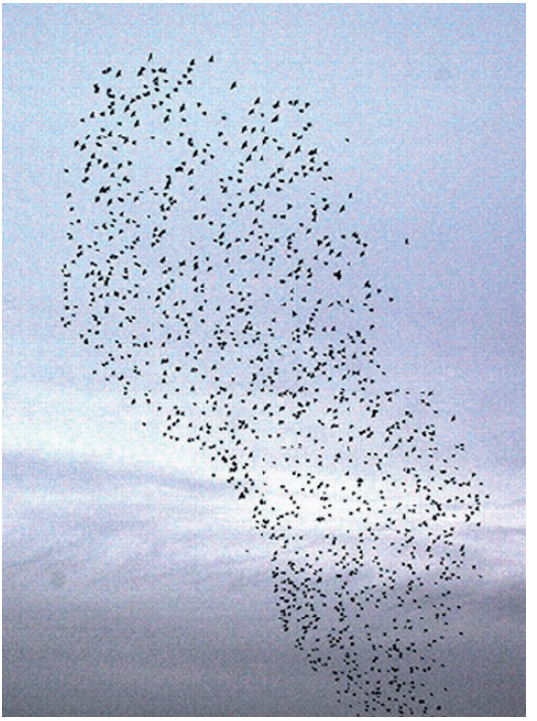

Figure 1.3: A murmuration of starlings displaying collective behaviour. From [23].

Just like individual birds in a flock, individual dust particles follow a simple rule that governs how they interact with each other. This rule is presented as an equation for the interaction potential of these particles, and it leads to fascinating collective behaviour over a multitude of interactions. This work is dedicated to understanding how surprising collective behaviour in complex plasmas emerges from the simple rule of interparticle interaction.

1.2 Collective effects

Collective effects in complex plasmas arise from the interparticle interactions of many charged microparticles within the plasma. These effects manifest themselves through the emergence of self-organised structure formation, as well as emergent behaviour and excitations. The microparticle suspensions in complex plasmas are optically thin and transparent, which gives them the great advantage that the processes can be observed at the kinetic (particle) level via non-disruptive methods. This makes complex plasmas excellent model systems for studying a variety of phenomena such as phase transitions, particle transport, and waves with a difficult to match level of detail and precision.

In this chapter, I present some examples of the collective behaviour of microparticles leading to emergent phenomena in complex plasmas. Furthermore, I will briefly outline the phenomena investigated in this work.

1.2.1 Model systems for conventional fluids

Droplets

Droplets form in conventional fluids such as water as a result of balancing interparticle forces. Water molecules weakly attract each other due to hydrogen bonding and the van der Waals force. Inside the drop of water, each water molecule is pulled in all directions equally as it is surrounded entirely by other water molecules, resulting in a net zero pull. However, water molecules on the surface are not surrounded by other water molecules on every side. This results in *surface tension* and a net force inwards. This inwards pressure from the surface molecules compresses the droplet. However, the Brownian motion of the water molecules inside the droplet creates an outwards pressure that counteracts the cohesive force due to surface tension. The two forces balance each other out and result in a stable droplet.

The traditional view of droplet formation as described above only works because each water molecule attracts the other water molecules to itself. This traditional view therefore does not apply to droplet formation in complex plasmas, as the microparticles repel each other. This means that typically there should not be a surface tension-like force pulling the particles together. Despite this, surface tension effects have been observed in complex plasmas, with one example being the self-ordering of microparticles into a droplet. While observations of droplets in complex plasmas have been a relatively recent development, multiple experiments have noted the condensation of microparticles into spheres in different experimental conditions [24–27], even in cryogenic plasmas [28, 29]. These droplets can be as small as a few hundreds of microns or as big as a few millimetres in size. So far there has been little investigation into what makes it possible for a droplet to form and remain stable in a complex plasma. Experimental observations and our theoretical model of the formation of these droplets can be found in Chapter 4.

Shock waves

In both complex plasmas and conventional fluids, a supersonic flow past an obstacle generates pressure waves. If a wavefront travels faster than the speed of sound in the system, it is known as a shock wave. These shock waves can form both in front of and behind the obstacle in the form of hemispherical bow shocks and cone-shaped Mach cones respectively. Examples of these shock waves can be seen in Fig. 1.4. The pressure waves generated due to a supersonic bullet are visualised in a shadowgraph image shown in Fig. 1.4**a**, showing a bow shock in front of the bullet[3]. A defining characteristic of shock fronts is that they mark the boundary where the flow speed changes from supersonic to subsonic. The fluid velocity, temperature, and pressure all rapidly decrease once the flow passes the shock front. This can be seen in Fig. 1.4**b**, as the Mach cones behind the aircraft are made visible due to the condensation of water in the air as temperature, pressure, and velocity of the air rapidly drops past the shock front. Complex plasmas can be used to study the formation of shock fronts at the level of individual particles, and in turn, shock fronts in complex plasmas can be used to determine certain plasma parameters. A theoretical discussion of shock fronts in complex plasmas is presented in Section 2.6, and simulation results in Chapter 5.

Turbulence

Turbulence is one of the oldest unsolved problems in physics. The first known use of this term in its modern form was by Leonardo da Vinci in the 1500s, who studied how water flowing into a pool generated eddies and vortices, and called the phenomenon '*turbolenza*'. This is documented in his famous illustration shown in Fig. 1.5**a**. Since then, turbulence has held a special place in both

[3] A bow shock is a three-dimensional hemispherical structure, however it looks like an arc in the image as a shadowgraph is a 2D flow visualisation method.

a) 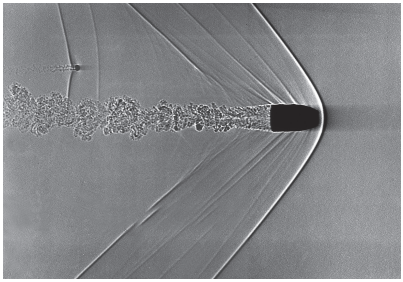 **b)** 

Figure 1.4: **a**) A shadowgraph image of a supersonic bullet showing an arc-like bow shock in front of it. From [30] (Image courtesy of Andrew Davidhazy/Rochester Institute of Technology). **b**) Mach cones behind the F/A-18C Hornet visible due to condensation as air pressure, temperature, and velocity rapidly decrease after passing the boundary of the shock wave. From [31] (U.S. Navy).

a) 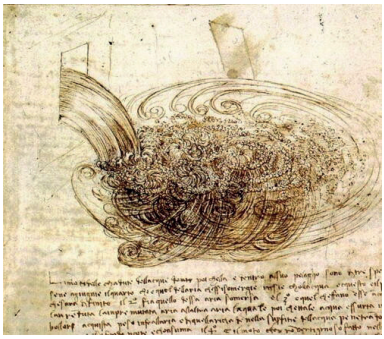 **b)** 

Figure 1.5: **a**) Leondaro da Vinci's studies on turbulence in water in 1510. From [32] (RCIN 912660 The Windsor Collection. Royal Collection Trust Copyright Her Majesty Queen Elizabeth II 2021). **b**) The starry night, beautifully painted by Vincent van Gogh in 1889, vividly portrays the essence of turbulence in the swirls and vortices painted in the sky. From [33].

scientific and artistic endeavours. It is the main focus of one of the most famous and recognisable paintings in the world, *The Starry Night*, shown in Fig. 1.5**b**. It is not simply an intellectual problem, but a ubiquitous phenomenon present in the flow of water [34, 35], in the motion of atmospheric currents [36], and even in the shifting electromagnetic fields on the Sun [37].

As it is so widespread in nature, the study of turbulence spans a wide range of scientific disciplines including fluid dynamics, meteorology, astrophysics, engineering, and biophysics. Understanding turbulence is not only a scientific pursuit but also a practical necessity for optimising designs, improving efficiency, and ensuring safety in various applications. It represents a state of fluid motion characterised by chaotic, irregular, and highly unpredictable behaviour, in stark contrast with the ordered and smooth motion observed in laminar flow regimes. Turbulence manifests itself as a complex phenomenon with vortices, eddies, and chaotic fluctuations in flow properties such as velocity and pressure. Despite being one of the oldest investigated problems in physics, a complete description of turbulence as well as the ability to predict its onset well is missing to this day.

The problem of studying turbulence is further exacerbated by the lack of a clear definition for it. There are only signatures and hallmarks which can be used to recognise that the flow is turbulent. One of the main signatures is that turbulence has swirls and vorticies in it, as seen in Fig. 1.5. Another signature of 3D isotropic turbulence is that kinetic energy is carried by vortices from larger to smaller spatial scales until it is consumed by the viscous forces between particles. The many vortices are often visualised in conventional fluids with the help of dyes or tracer particles, which only provide information about the averaged flow properties.

In recent decades, significant progress has been made in understanding turbulence through experimental observations, theoretical analyses, and advanced computational simulations. Turbulence has been observed many times in complex plasmas [38–43], which are ideal systems for investigating the onset of turbulence as each individual particle can be imaged directly. These microparticles in a complex plasma *do not* behave as passive tracers to provide information about the average flow behaviour. Instead, the flow of the microparticles *themselves* becomes turbulent, which means they can be used to study turbulence at the *kinetic* level of the individual carriers of turbulent interactions. This allows for a more comprehensive understanding of the underlying physics of the onset of turbulence, which will be the main focus of Section 5.2.

1.2.2 Model systems for electrorheological fluids

Under the right conditions, microparticles in a complex plasma can arrange themselves in string-like clusters (SLCs), as seen in Fig. 1.2. This behaviour was first observed in 2008 by Ivlev et al. [44]. Since then, many similar observations have been reported [45–48]. Upon the application of an electric field to the plasma, the microparticles form SLCs along the direction of the electric field.

This is an example of *electrorheology*. The term "electrorheology" is derived from the words "electro" (related to electricity) and "rheology" (the study of the flow and deformation of materials). Thus, the study of electrorheology focuses on how the rheological properties of a fluid, such as its viscosity and dynamic modulus, can be changed by applying an electric field. A conventional electrorheological (ER) fluid is an electrically insulating fluid with polarisable particles immersed in it [49–51]. Upon the application of an electric field, the surface of the particles becomes polarised resulting in a dipole, thereby causing both interparticle attraction and repulsion. This can drastically affect the properties of the fluid as the particles within the fluid restructure and rearrange themselves according to the electric field.

The changes to the rheological properties of the fluid are rapid and reversible, which is a unique characteristic of ER fluids. Their sensitivity to changes in strength and frequency of the electric field gives rise to a wide variety of applications [52]. The properties of an ER fluid depend on multiple factors, such as the number density, size, and charge of the particles, as well as the the strength, frequency, and direction of the electric field, and the characteristics of the electrically insulating

medium. All of these parameters can be easily controlled in experiments. This enables manipulation of the rheological properties of the fluid and guide the phase transitions of the system depending on the desired outcome. Since the response time of the fluid to changes in the electric field is near instantaneous, ER fluids are ideal for use in manufacturing products that require speed and precision control, such as smart materials and electronics. Some applications of ER fluids include dampers and shock-absorbers for vehicles [53], adaptive vibration control systems [54], robotic grippers [55], haptic devices for minimally invasive surgery [56, 57], and smart fluids for energy dissipation and impact mitigation [58].

In conventional ER fluids, the SLCs form due to attraction between the particles once they become polarised by the electric field. Till now, it was unclear whether this is also the case in complex plasmas as the microparticles are like-charged and tend to repel each other. It was suspected that focusing of ions behind the microparticles by the external electric field may result in effective interparticle attraction. However, past simulations of such an attractive force between the particles became unstable due to high particle acceleration [59, 60]. In this work, I study the cause of SLC formation in complex plasmas by using experimental data to develop simulations in order to investigate whether such an effective attraction between the particles is necessary. The details and results of this study are discussed in Chapter 6.

1.3 Complex plasmas in experiments

Condensation into droplets, ordering into strings, and the onset of turbulence are all examples of collective behaviour observed in complex plasma experiments. There are various different types of complex plasma experiments being conducted in a variety of conditions. The main factor to consider is the effect of gravity on the structure of the microparticle collection.

The experiments discussed in this work use melamine formaldehyde (MF) particles with a mass density of $1510\ \mathrm{kg/m^3}$. The particle size is of the order of a few micrometres[4] (usually between $1 - 8\ \mu\mathrm{m}$), which is why they are also called *microparticles*. They have a uniform mass density, and so the larger the particles the heavier they are.

1.3.1 Ground-based experiments

Complex plasma experiments in ground-based laboratories are strongly influenced by gravity. Microparticles are much heavier than electrons and ions. As such, they sediment in the plasma making it difficult to perform 3D studies of the system. The particles thus need to be levitated in the plane of the illumination laser so that they can be observed. This can be done by using strong electric fields, which limits them to a small region above the lower electrode of the experimental setup and leads to a vertical gradient in the interparticle distance. A setup like this allows for the study of particle dynamics in 2D, with limited usability in 3D as the height is restricted only to a few layers.

Particles can be levitated against gravity using multiple other techniques to allow for a 3D investigation of the system. One method is to provide a temperature gradient within the chamber causing a net upwards force on the particles in the direction opposite to the gradient [61]. Another method is to optically trap the particles in a laser beam, similar to the *optical tweezers* used in colloidal suspensions [62]. Even magnetic fields could be used for particle levitation [63] (given that the particles are magnetisable[5]).

A better way of mitigating the effects of gravity is to conduct the experiment in an environment with as little gravitational force as physically possible - i.e., free-fall. In this case, even weak electric fields used to confine the microparticle cloud are enough and the system is isotropic in full 3D. The

[4] The particles in an experiment are usually *monodisperse*, i.e., they are all the same size within a few percent.

[5] This can be achieved by using plastic microparticles with a magnetic filler.

condition where gravity is reduced until its effects are negligible is known as *microgravity*. It allows for long-term suspension of microparticles within the plasma, enabling the study of microparticle dynamics without sedimentation. Conducting the experiment under microgravity conditions allows for the study of intrinsic complex plasma dynamics, without the interference of convective forces and instabilities that can be caused by levitation techniques. There are multiple ways to achieve this.

Drop towers

On Earth, the simplest way to balance the force of gravity on an object is to induce free-fall. Drop towers are tall structures specifically designed to facilitate free-fall experiments. One such drop tower is located at the University of Bremen[6]. It consists of an approximately $150\ \mathrm{m}$ vertical tower with a $120\ \mathrm{m}$ drop tube inside. The experimental setup is placed at the top of the tower, and allowed to fall freely through the drop tube. The primary objective of drop tower complex plasma experiments is to create a microgravity environment, which typically lasts only for about $5\ \mathrm{s}$. Drop towers are particularly useful as they are cost effective, easy to operate, and can in principle conduct thousands of tests per day.

Parabolic flights

Another route to free-fall on Earth is through a *parabolic flight*[7], so called due to the parabolic trajectory of the plane. These flight campaigns typically involve multiple parabolic manoeuvres[8] over a single flight, allowing researchers to conduct multiple trials of experiments with $22\ \mathrm{s}$ of consecutive microgravity. During parabolic flights, the aircraft follows a trajectory that includes an ascend, the parabola, and a descend. In the ascending and descending phase, the aircraft experiences *hypergravity* conditions at $1.8\ \mathrm{g}$, much higher than Earth's gravity. The most important phase for complex plasma experiments, however, is the microgravity phase during the parabolic arc. During this period, the aircraft enters free fall to mimic a lunar ($0.2\ \mathrm{g}$) or martian ($0.4\ \mathrm{g}$) gravitational environment or even go as low as $10^{-2}\ \mathrm{g}$ depending on the parabola.

1.3.2 Experiments on the ISS: history and future

An even better method to mitigate gravity would be to place the laboratory such that it is in constant free-fall - for instance, on the International Space Station (ISS). The microgravity experimental conditions at $10^{-6}\ \mathrm{g}$ (which can be sustained for *years*) provided by the ISS are unmatched by anything on Earth. The Plasmakristall (PK) program was launched in 2001 to study microparticles in plasmas in microgravity conditions on the ISS. These were not dedicated *experiments*, but *laboratories* where various experiments could be performed. The previous generation of experiments within this research program, such as those performed using the PKE-Nefedov (2001 - 2005), enabled us to study the dynamics of particle interactions without the sedimentation or agglomeration that occurs under normal gravity [64]. Since then, further sophistications in technology have enabled microgravity experiments to significantly advance our understanding of complex plasma physics. The second generation of microgravity experiments using the PK-3 Plus laboratory (2005 - 2013) allowed us to study a homogeneous and isotropic distribution of complex plasmas, which was not possible earlier [65]. The current generation of experiments using the PK-4 facility (2014 - Present) equip us to study flowing complex plasmas and how the flow behaves when perturbed [66]. Now, the next generation of

[6]More information on the drop tower at the University of Bremen is available at `https://www.zarm.uni-bremen.de/en/drop-tower`

[7]The parabolic flights in Europe are performed using the Airbus A310. More information about these flight campaigns can be found at: `https://www.airzerog.com`.

[8]For the experiments done on the Airbus A310, a total of 31 parabolic manoeuvres are performed in a one flight, with each manoeuvre providing $22\ \mathrm{s}$ of microgravity. In total, a single flight can provide more than $10\ \mathrm{minutes}$ of microgravity.

complex plasma experiments are being planned with the as-yet unlaunched COMPACT facility for more precise and systematic measurements of transport properties, phase transitions, nonlinear and non-equilibrium phenomena [67, 68].

PK-3 Plus was the second generation of complex plasma microgravity experiments on the ISS. Compared to PKE-Nefedov, the PK-3 Plus facility had an updated hardware, software, and diagnostics which allowed for major advances in research [65]. The lab was launched in December 2005 and first used in January 2006. After a total of 21 missions, the facility was de-orbited in 2013 [69]. With a diameter of $6\ \mathrm{cm}$, it had larger electrodes than the $4.2\ \mathrm{cm}$ ones in PKE-Nefedov. These (as well as other metallic parts) were made out of aluminium to avoid propagating magnetic disturbances and to prevent the formation of temperature gradients. The new thermal improvements to the facility reduced the buildup of thermophoretic effects that may have otherwise ruined the microgravity conditions. Amongst the many improvements was the ability to use two types of working gases, namely argon and neon. PK-3 Plus also had an increased number of microparticle dispensers compared to PKE-Nefedov (6 instead of 2), as well as a higher number of cameras (4 instead of 2) with double the frame rate ($50\ \mathrm{FPS}$ instead of $25\ \mathrm{FPS}$) [65].

Building upon the success of the previous labs, the PK-4 facility was launched in 2014 as a continuation of the investigation into complex plasmas on the ISS. It explores the dynamic behaviour of microparticles in flowing complex plasmas and primarily focuses on the evolution and manipulation of the complex plasma flow. Its experimental geometry sets it apart from its predecessors, which were designed to study static complex plasmas. The PK-4 lab has six microparticle dispensers, the same number as in PK-3 Plus. The number of cameras is reduced from 4 to 2, but they are capable of providing a much higher frame rate in the range of $35-210\ \mathrm{FPS}$, with $70\ \mathrm{FPS}$ being more practically used [70].

The next generation of the complex plasma experiments in microgravity are being planned using the complex plasma facility, COMPACT. This is intended to be a multipurpose experimental facility accessible to the wider international scientific community [67, 68, 71]. A core part of this new facility is the 'Zyflex' chamber ("zylindrisch" and "flexibel" in German). This is a cylindrical plasma chamber with the capability to flexibly change its inner volume to allow for a variety of different plasma conditions as well as discharge aspect ratios. The unique multiple electrode setup enables a better control of the plasma geometry and the electric fields. The updated technology is equipped to handle much lower gas pressures than ever before, further reducing the damping of microparticle motion. This design is highly versatile and adaptable to a wide variety of complex plasma experiments in microgravity, opening up new research avenues as well as allowing for higher precision measurements.

This plasma chamber builds on and advances the previously existing technology in microgravity experiments. For comparison, at a diameter of $12\ \mathrm{cm}$, the electrodes in the Zyflex chamber are much larger than those in the PK-3 Plus chamber which were only $6\ \mathrm{cm}$ across [68]. Moreover, these electrodes are segmented with each segment being electrically insulated and independently operational, allowing for more precise control of the plasma parameters. Additionally, the distance between the top and bottom electrodes can now be varied from $25\ \mathrm{mm}$ to $75\ \mathrm{mm}$ [68], which was not possible in the PK-3 Plus chamber.

The Zyflex plasma chamber (as a part of COMPACT) marks the beginning of the next generation of microgravity experiments by bringing together innovative technological capabilities and advancements that significantly enhance the range of parameters accessible for complex plasma research in microgravity. The chamber allows for studying larger microparticle suspensions in precision-controlled plasma environments with reduced damping and a variety of manipulation techniques. The COMPACT facility is yet to be launched.

1.4 Contribution of this thesis

The aim of this thesis is to understand the various emergent phenomena that occur in complex plasmas in the context of individual interparticle interactions that lead to collective behaviour. In this work, I focus on simulations and theoretical models of microparticles that were informed by experimental observations. These simulations have served to complement experiments, offering insights and aiding the interpretation of the underlying physics. Moreover, the findings from the simulations will guide and inform future experiments in the field of complex plasma research.

The emergent phenomena covered in this work are as follows. Firstly, I discuss experimental observations of microparticle condensation into droplets in both the ground-based modified PK-3 Plus chamber and the Zyflex chamber during a parabolic flight. These observations help construct a theoretical picture to understand the self-formation of a stable droplet without interparticle attraction leading to a surface tension force. By connecting the observed droplet radius with plasma parameters, this work allows droplets to be used as a diagnostic tool to estimate plasma parameters in experiments for the first time.

Secondly, I simulated complex plasmas flowing past an obstacle in 3D. This led to the formation of structures such as shock waves (Mach cones and bow shocks) as well as the onset of turbulence. Studying turbulence with complex plasmas provides the unique advantage of being able to resolve each particle individually and track changes to its flow profile. In this work, I investigated how the parameters such as flow speed, particle charge, and gas pressure affected the formation of these shock fronts and the ability for the flow to become turbulent. I was able to reliably trigger the onset of turbulence by changing one of these parameters, and studied the transition of flow from laminar to turbulent. The parameter regime used can be reproduced in most experimental setups designed to study flowing complex plasmas. This work can thus be used to inform future experiments and open up new research avenues for detailed particle-resolved studies of the onset of turbulence using complex plasmas.

Finally, I discuss the recent experimental observations of particles crystallising into SLCs in the PK-4 lab experiment, and compare them with my computer simulations. Together with the PK-4 team, I investigated whether the focusing of ions behind the particles leads to effective long-range attraction, and in turn the formation of SLCs. We found an excellent qualitative agreement between experiments and simulation, which surprisingly showed that there is no effective long-range attraction between the microparticles. We found that - in agreement with previous simulations [59, 60] - effective long-range attraction leads to simulations becoming unstable and deviating from experimental observations. We show in this work that the the ion focusing leads to a reduction in repulsion instead of an effective attraction. We conclusively demonstrate that in order to form SLCs, the interparticle potential only needs to be slightly less repulsive, and that interparticle attraction is not necessary.

I will first lay the theoretical groundwork as well as give details on the simulation and discuss the relevant experimental setups. Then, I will focus on the results from each of the aforementioned emergent phenomena in detail.

Chapter 2

Theory

"Except near the electrodes, where there are sheaths containing very few electrons, the ionized gas contains ions and electrons in about equal numbers so that the resultant space charge is very small. We shall use the name plasma *to describe this region containing balanced charges of ions and electrons."*

Irving Langmuir (1928) [72]

2.1 Plasma conditions

The plasma ionisation process via collisions with a high-energy electron is as follows:

$$e^- + A \longrightarrow 2e^- + A^+, \tag{2.1}$$

where A refers to the atoms of the gas being ionised into a plasma. The plasma is therefore a gas made of two charged species: the electrons e^-, and the ions A^+, as well as the neutral unionised gas atoms, A. Complex plasmas are a special case which contain a third charged species, the negatively charged 'dust' or microparticles. The fraction of gas atoms converted into ions is measured by the ionisation fraction of the plasma, given by

$$\alpha = \frac{n_i}{n_i + n_n}, \tag{2.2}$$

where n_n and n_i are the neutral gas atom number density and the gas ion number density respectively. For fully ionised plasma, $\alpha = 1$. The plasma used in complex plasma experiments is *weakly ionised*, which means that the ionisation fraction is very low, $\alpha \ll 1$. As a result of this, the collisions between the neutral gas atoms and the ions dominate over the ion-ion collisions. The ions in the plasma then enter thermal equilibrium with the gas, $T_i = T_n$, where T_i and T_n are the temperatures of the ions and the neutral atoms respectively. This is why these plasmas are also referred to as *low temperature* plasmas. The electrons, in comparison, are much hotter than the ions despite having the same charge as they are smaller and lighter. They get accelerated easily, and as a result, heat up. This results in a *non-equilibrium plasma* in experiments, where the electron temperature $T_e \gg T_i$, in contrast with *isothermal plasmas* like the solar wind where $T_e = T_i$.

2.1.1 Shielding

As the plasma contains both positive and negative charges, the electric fields of any charged particles introduced in the system will be strongly shielded. Consider a test charge, q, introduced in the plasma. It attracts unlike-charges and repels like-charges, bending their trajectories around itself as well as collecting them on its surface. The bent trajectories of charges around the test charge create a reduced space charge in its vicinity, thus reducing and weakening its electric field. The colder (and hence slower) the ions and electrons are, the more their trajectories bend around the test charge, leading to a stronger shielding effect. If the ions are streaming very fast, the shielding is primarily due to the slower electrons and *vice versa*.

The effect on the electron and ion densities due to the test charge can be written as

$$n_e(\mathbf{r}) = n_{e,0} \exp\left(+\frac{e\phi(\mathbf{r})}{k_B T_e}\right) \approx n_{e,0}\left(1 + \frac{e\phi(\mathbf{r})}{k_B T_e}\right), \tag{2.3}$$

$$n_i(\mathbf{r}) = n_{i,0} \exp\left(-\frac{e\phi(\mathbf{r})}{k_B T_i}\right) \approx n_{i,0}\left(1 - \frac{e\phi(\mathbf{r})}{k_B T_i}\right). \tag{2.4}$$

Here, $\phi(\mathbf{r})$ is the potential due to the test charge at position $\mathbf{r}$, and $n_{e,0}$ and $n_{i,0}$ are the electron and ion number densities at equilibrium. The approximation is a result of assuming that the disturbances to the potential energy due to the test charge are small compared to the thermal energies of the electrons and ions. The electric potential, ϕ, of the test charge can be obtained by using Equations 2.3 and 2.4 to solve Poisson's equation, given by

$$\nabla^2\phi = -\frac{e}{\epsilon_0}(n_i - n_e). \tag{2.5}$$

A well-known solution of this is the *shielded Coulomb* or *Yukawa* potential:

$$\phi(r) = \frac{q}{4\pi\epsilon_0 r} e^{-r/\lambda_D}. \tag{2.6}$$

The contribution to the electric shielding by ions and electrons is given by

$$\lambda_{Dx}^2 = \frac{\epsilon_0 k_B T_x}{n_{x,0} e^2}, \quad \text{where} \quad x \in \{i,\ e\}. \tag{2.7}$$

Here, λ_{Dx} and $n_{x,0}$ refer to the Debye length and equilibrium number densities of ions, i, and electrons, e, given by the subscript x. The combined or *linearised Debye length*, λ_D, is then just

$$\lambda_D^{-2} = \lambda_{De}^{-2} + \lambda_{Di}^{-2}. \tag{2.8}$$

In a complex plasma, the negatively charged microparticle is surrounded by positive ions in a sphere of radius λ_D around it, known as the *Debye sphere* or the ion shielding cloud. All microparticles in the plasma within a few Debye lengths interact with each other. Beyond this distance, the interparticle force is low enough to be negligible.

Sheath

Near the walls of the experimental chamber, electrons are lost to the wall faster than the ions. The wall charges up negatively and provides a confinement potential to the electrons in the bulk of the plasma. This repels the electrons and so acts as a 'barrier' around the plasma. This boundary layer is known as the *sheath*.

Microparticles in complex plasma experiments are often levitated in the sheath region by electric forces to perform quasi-2D experiments in ground laboratories, where their electric potential is screened mainly by the electrons. In an (over-)simplified view, this is because the ions stream much

faster in the sheath region than the electrons, and so the contribution of the ions to the screening is negligible. Bohm [73] showed in 1949 that ions enter the sheath at a velocity greater or equal to the ion speed of sound (also known as the Bohm velocity), $v_{\mathrm{Bohm}} = \sqrt{k_B T_e / m_i}$. This condition fulfils energy conservation as well as ion continuity conditions. The Debye length can thus be approximated by the electron Debye length, $\lambda_D \approx \lambda_{De}$ in the sheath. Conversely, the bulk of the plasma contains slow subthermal ions. Here, the electron temperature is much higher than the ion temperature resulting in $\lambda_{De}^{-2} \ll \lambda_{Di}^{-2}$. Hence, in the plasma bulk the Debye length is approximated well by the ion Debye length $\lambda_D \approx \lambda_{Di}$ instead.

In a more realistic view, the suprathermal (directed) ion flow in the sheath region creates an anisotropy in the ion shielding cloud. The general expression of the shielding length is given by Khrapak et al. [74] as:

$$\lambda_D = \lambda_{De} \frac{1}{\sqrt{1 + f(\chi)\tau}}, \tag{2.9}$$

where

$$f(\chi) = \frac{1}{1 + 2\chi^2} \quad \text{and} \quad \chi = \mathcal{M}_i \sqrt{\tau/2}. \tag{2.10}$$

The parameter χ is a measure of the ion streaming velocity, expressed in terms of the ion Mach number, and $\tau = T_e/T_i$ is the ratio of the electron to ion temperature. For an isotropic case with low ion streaming velocities (such as in the bulk of the plasma), $\chi = 0$, and the expression simplifies to $\lambda_D = \lambda_{Di}$. For an anisotropic case with fast streaming ions (such as in the sheath), $f(\chi)\tau \to 0$, and the expression simplifies to $\lambda_D = \lambda_{De}$. For intermediate ion streaming velocities, the expression provides a smooth transition by interpolating the screening length between these two regimes.

2.1.2 Quasineutrality

Except for the sheath region, the number densities of positive and negative charges in the plasma are equal at equilibrium. This is known as the *quasineutrality* condition:

$$n_i = n_e + Z_d n_d, \tag{2.11}$$

where Z_d is the average number of electrons collected by a microparticle on its surface.

Due to the shielding in the plasma, any electric perturbation decays exponentially for distances larger than the Debye length. For values of $r \gg \lambda_D$, the electron and ion number densities return to their equilibrium value as seen from Equations 2.3 and 2.4. An analogous calculation shows that the microparticle number density similarly returns to equilibrium. This means that the plasma is overall electrically neutral on length scales $r \gg \lambda_D$. Correspondingly, the charge densities in a plasma (when disturbed) fluctuate at the plasma frequency, ω_x, with the subscript $x \in \{i,\ e,\ d\}$ referring to the ions, i, electrons, e, or dust, d. This means that it takes the charges $\tau_x = 1/\omega_x$ to reach a new equilibrium number density. As the frequency depends inversely on the mass of the charged species, $\tau_e \ll \tau_i \ll \tau_d$, lighter species have a higher plasma frequency and return to equilibrium faster.

The plasma is thus *quasineutral* for length scales $r \gg \lambda_D$ and time scales $t \gg \tau_d$ [2].

2.2 Particle charging

There are multiple ways in which particles immersed in a plasma can collect charge. The particles can be charged through high-velocity ballistic collisions, UV radiation, heating (thermionic emission), or via secondary electron/ion emission. Most of these charging mechanisms are not relevant for complex plasmas, and so will not be covered here.

The particles themselves may or may not be electrically neutral when they are dispensed into the plasma. It is common for particles to charge each other through a process called *triboelectric charging* [75]. Similar to how a balloon accumulates static charge on its surface, the microparticles become positively or negatively charged by exchanging electrons with each other. Once in the plasma, the particles experience a large flux of electrons on their surfaces and become highly negatively charged. The particle charge is thus a function of parameters such as electron density and temperature[1]. As electrons have a significantly lower mass than ions, they have a significantly higher thermal velocity $T_e \gg T_i$. The resulting electron flux onto the microparticles is much greater than the ion flux, causing them to be highly negatively charged. The charging of microparticles therefore depends on a lot of parameters such as the size of the particle, electron and ion number densities, temperatures, etc. All of these parameters affect the microparticles, and *vice versa*. This makes calculating the charge on the microparticles a very complicated task. Here, I will ignore the effects of the microparticles on the plasma, and provide an idealised case [76].

Consider a single microparticle when it is first dispensed into the plasma. The particle is electrically neutral, and much larger than the electrons and ions present in the plasma. As it is a big target which doesn't repel the electrons and ions, it will collide with many of them. Multiple electrons or ions moving towards the particle and colliding with it can be thought of as an electric current, I_e or an ion current, I_i. Once the particle has accumulated a certain charge on its surface, this charge also starts influencing the currents. Eventually, the microparticle charge reaches a stable value (neglecting charge fluctuations) as all the currents flowing to the microparticle sum to a net zero. The potential reached by the microparticle at this point is known as the *floating potential*, ϕ_{fl}. The floating potential is defined by

$$\Sigma_x I_x(\phi_{fl}) = \frac{dq_d}{dt} = 0, \quad \text{where} \quad x \in \{i,\ e\}. \tag{2.12}$$

Determining the floating potential is the first step to calculating the particle charge at equilibrium. This is done by calculating and then equating the electron and ion currents, $I_e = I_i$.

The most common way to calculate the electron and ion currents flowing to the particle is to use Orbital Motion Limited (OML) theory. The name of the theory stems from the fact that the model is equivalent to the Keplerian model of planetary motion. The OML model assumes that electrons and ions move towards the dust particle from infinity without any obstacles or collisions along the way. The only interactions they have are the electrostatic interactions with the dust particle.

For a charged species like an ion moving towards the particle, the impact parameter, b, is a measure of its displacement from the particle in the direction perpendicular to its motion. At the critical value of the parameter, b_c, the ion just grazes the particle. This means that for all $b \leq b_c$ the ion will impact the particle and contribute to its charging, and for all $b > b_c$ the ion will simply be deflected by the particle.

The critical parameter, b_c can be found by considering the conservation of energy and angular momentum as it passes by the particle. The conservation equations are:

$$L = m_i v_{i,0} b_c = m_i v_i a, \tag{2.13}$$

$$\frac{1}{2} m_i v_{i,0}^2 = \frac{1}{2} m_i v_i^2 + e\phi_p, \tag{2.14}$$

where a is the microparticle radius, $v_{i,0}$ is the initial ion velocity at infinity, and ϕ_p is the potential of the microparticle.

This results in the following expression for the critical parameter:

$$b_{c,i}^2 = a^2 \left(1 - \frac{2e\phi_p}{m_i v_{i,0}^2}\right). \tag{2.15}$$

[1] In the experiments, the particle charge can also be a function of spatial coordinates via the local plasma parameters.

The cross section of the collisions of ions with the particle is then just $\sigma_i = \pi b_{c,i}^2$. The analogous calculation for electrons leads to the expression

$$b_{c,e}^2 = a^2 \left(1 + \frac{2e\phi_p}{m_e v_{e,0}^2}\right), \tag{2.16}$$

with the electron-particle collision cross section as $\sigma_e = \pi b_{c,e}^2$. Note the change of sign between the equations 2.15 and 2.16. The potential on the particle is negative, $\phi_p < 0$, and so the impact parameter for electrons is smaller than that for ions. This difference arises due to the electrons being repelled from the microparticle as it charges up negatively, thus reducing the cross-section of collisions.

Using the critical parameter to calculate the cross sections, the electron and ion currents to the particle can then be calculated to be:

$$I_i = \pi a^2 n_i e \sqrt{\frac{8k_B T_i}{\pi m_i}} \left(1 - \frac{e\phi_p}{k_B T_i},\right) \tag{2.17}$$

$$I_e = -\pi a^2 n_e e \sqrt{\frac{8k_B T_e}{\pi m_e}} \exp \frac{e\phi_p}{k_B T_e}. \tag{2.18}$$

Setting $I_i = I_e$ results in the floating potential

$$1 - \frac{e\phi_{fl}}{k_B T_i} = \sqrt{\frac{m_i T_e}{m_e T_i}} \frac{n_e}{n_i} \exp \frac{e\phi_{fl}}{k_B T_e}. \tag{2.19}$$

The charge of the microparticle can finally be calculated by assuming it is a spherical capacitor as $q_d = C\phi_{fl}$, where the capacitance, C in a plasma with shielding is $C = 4\pi\epsilon_0 a \left(1 + \frac{a}{\lambda_D}\right)$. Typically, the radius of the particle is much smaller than the Debye length, $a \ll \lambda_D$, and so the capacitance reduces to $C = 4\pi\epsilon_0 a$.

The OML model of particle charging only works well if the mean free path of the ion-neutral collisions is much larger than the Debye length, $l_{i-n} \gg \lambda_D$. In the event that $l_{i-n} \sim \lambda_D$, the ions no longer have a collisionless path to the particles, and the theory overestimates the particle charge. The reason for this is because if ions lose energy to ion-neutral collisions, they are more likely to get collected by the microparticle, and thus reduce the particle charge.

Another model of particle charging is provided by the Drift Motion Limited (DML) theory, which takes into account the effect of ion-neutral collisions [77]. This theory modifies the ion current on the particle depending on the ion mean free path and the particle radius by defining a new parameter ξ as:

$$I_i = \pi a^2 n_i e \sqrt{\frac{8k_B T_i}{\pi m_i}} \left(1 - \xi \frac{e\phi_p}{k_B T_i},\right). \tag{2.20}$$

In the collisionless case, $\xi = 1$, and the ion current from OML theory is recovered. In the collisional case, for values of $l_{i-n} < \lambda_D/3$, the parameter is given by

$$\xi = \sqrt{\frac{2\pi}{3}} \frac{l_{i-n}}{a}. \tag{2.21}$$

For values of $l_{i-n} > 0.1\ \lambda_D$, where OML theory is known to overestimate particle charge, the following fit works well by replacing the particle radius in Equation 2.21 with:

$$a \to a + \sqrt{\frac{2\pi}{3}} \frac{l_{i-n}^2}{3\lambda_D + l_{i-n}}. \tag{2.22}$$

2.3 Forces acting on the particles

2.3.1 Electric force

As microparticles in complex plasmas are highly negatively charged, they are affected by various electric fields in the plasma. These are often used for confinement, levitation, or manipulation of the particles during an experiment to induce changes in the system. The particles are affected by these external fields and at the same time are repelled by each other.

The electrical potential between two charged particles in a vacuum is given by the Coulomb potential,

$$\Phi_C = \frac{q^2}{4\pi\epsilon_0 r}, \tag{2.23}$$

where q is the particle charge, r is the interparticle distance, and ϵ_0 is the free space permittivity. The same is true for microparticles immersed in a plasma, except that their interparticle potential is screened at large distances due to the presence of electrons and ions in the plasma. The interparticle potential of microparticles in a complex plasma is therefore given by the Yukawa potential, which is simply a Coulomb potential with an exponential decay term from the plasma shielding:

$$\Phi_Y = \Phi_C \exp\left(-\frac{r}{\lambda_D}\right), \tag{2.24}$$

where the parameter λ_D, known as the Debye length, quantifies the effect of the screening. This length measures the distance at which the magnitude of the interparticle potential is reduced by e^{-1}.

The total electric force acting on the particles, F_e, is then simply the sum,

$$\mathbf{F}_e = \mathbf{F}_Y + \mathbf{F}_{Ex} = \frac{-d}{dr}\Phi_Y + q\mathbf{E}_{Ex}, \tag{2.25}$$

of the force due to the Yukawa interparticle interactions, F_Y, and the force due to an external electric field, F_{Ex}.

The interparticle force decays with increasing interparticle distances as $r^{-2}e^{-r/\lambda_D}$. This means that every particle is interacting with all other particles within several Debye lengths from it. As the interparticle force decays exponentially, the interparticle interactions become very weak further away.

2.3.2 Gravity

The electric force of the sheath is often used for levitation in ground-based experiments to counteract the force of gravity on the microparticles, as they would otherwise fall to the bottom of the chamber. The gravitational force is given by the simple equation

$$\mathbf{F}_g = \frac{4}{3}\rho_d \pi a^3 \mathbf{g}. \tag{2.26}$$

where $\rho_d = 1510\ \mathrm{kg/m^3}$ is the mass density of the MF particles often used in experiments. The larger the microparticles, the more massive they are, and hence the stronger the force of gravity pulling them down.

2.3.3 Thermal forces

Another way to counteract gravity in ground-based experiments is through the use of external thermal forces, applied on the microparticles by using a temperature gradient in the background gas. This was first done in 1991 by Jellum et al. [78] by heating up an electrode in the experimental setup. It was

later shown in 2002 by Rothermel et al. [61] that this thermophoretic force can be used to mitigate the effects of gravity in complex plasma experiments. Due to this temperature gradient, the neutral gas atoms on the side closer to the hot electrode transfer a larger momentum to the microparticles than those on the side closer to the cold electrode. This results in a net force on the microparticles in the direction opposite to the temperature gradient. A levitation force acting against gravity can therefore be applied by heating the bottom electrode in the experimental chamber. Using the kinetic theory of gases, the thermophoretic force can be calculated to be [79]:

$$\mathbf{F}_{th} = -\frac{32}{15}\frac{a^2 k_n}{v_{th,n}}\nabla \mathbf{T}_n, \tag{2.27}$$

where k_n and ∇T_n are the thermal conductivity and temperature gradient of the gas. The magnitude of the thermophoretic force scales as $F_{th} \propto a^2$, which means that given the right parameters, it is possible to mitigate the effect of gravity to a certain extent by using a temperature gradient, but doing so causes the particles to be sorted by size if no monodisperse particles are used (which is also the case for levitation by electric fields in the sheath).

2.3.4 Ion drag force

Similar to the neutral atoms, the motion of ions and electrons in the plasma also has an effect on the microparticles. The motion of the ions relative to the microparticles results in a transfer of momentum from the ions to the particles in the form of an ion drag force, F_{id}. In comparison, the electron drag force is many orders of magnitude smaller and therefore often neglected as the electrons are much lighter than the ions and thus impart a negligible amount of momentum to the particles.

The total ion drag force has two main components. The first is the force exerted via direct collisions between the ions and the particle, F_{id}^{dir}, as the ions are collected on the particle surface. The second is due to the Coulomb scattering of the ions around the microparticle, F_{id}^{Coul}. The total magnitude of the ion drag force directed along the ion motion is then $F_{id} = F_{id}^{dir} + F_{id}^{Coul}$. The deformation of the ion cloud around the microparticle by the ion flow is ignored as the effect is too small in comparison.

Barnes model

The following is a model of the ion drag force developed by Barnes et al. [80]. It follows the particle charging calculation from OML theory.

The direct charging component and the Coulomb collisional component of the ion drag force are given by the general expression:

$$\mathbf{F}_{id}^{x} = \sigma_x m_i \bar{v_i} n_i \mathbf{v}_{i,\mathrm{drift}}. \tag{2.28}$$

Here, the index x refers to whether the force is due to direct collisions or Coulomb collisions, and σ_x is the relevant collision cross section. The momentum transferred to the particles is $m_i \bar{v_i}$, where $\bar{v_i}$ is the mean ion velocity defined as $\bar{v_i}^2 = v_{i,\mathrm{drift}}^2 + v_{i,\mathrm{thermal}}^2$, and n_i is the ion number density.

The ions collected on the particle surface during the microparticle motion result in the F_{id}^{dir} component of the ion drag force. As a result, the associated cross section is

$$\sigma_{dir} = \pi b_c^2, \tag{2.29}$$

where b_c is the charge collection parameter.

For Coulomb collisions, the cross section is given by

$$\sigma_{Coul} = 4\pi b_{\pi/2}^2 \ln \Lambda, \tag{2.30}$$

where $b_{\pi/2}$ is the impact parameter where the ions get deflected by $90°$. The Coulomb logarithm, given by $\ln\Lambda$, accounts for the screening of Coulomb collisions in the plasma. This means that only the Coulomb collisions within one Debye length, λ_D, are considered in the calculation.

The total ion drag force in the Barnes model is then just

$$\mathbf{F}_{id} = m_i \bar{v}_i n_i \mathbf{v}_{i,\mathrm{drift}}(\sigma_{dir} + \sigma_{Coul}) \tag{2.31}$$

directed along the direction of the ion motion.

Hutchinson/Khrapak model

The Barnes model does not account for Coulomb collisions outside the Debye sphere, which means it underestimates the ion drag force for highly charged microparticles [76]. Khrapak et al. [81] and Hutchinson [82] modified the Coulomb logarithm, $\ln\Lambda$, to

$$\ln\Lambda = \ln\frac{b_{\pi/2} + \lambda_s}{b_{\pi/2} + a} \tag{2.32}$$

in order to accommodate for collisions that happen further than one Debye length away. Here, λ_s is the modified screening length. This interpolates the Debye length for ion velocities ranging from the thermal velocity to high streaming velocities, and is given by the expression:

$$\lambda_s^2 = \frac{\lambda_{De}^2}{1 + 2k_B T_e/(m_i v_i^2)} + a^2. \tag{2.33}$$

Not only does this model account for collisions further away than one Debye length, it also accounts for the changes in Debye length based on the ion streaming velocities. The bulk of the plasma contains slow subthermal ions, in which regime the Barnes model and the Hutchinson/Khrapak model disagree by a factor of two or more. As the ion collisionality is not taken into account in the Barnes model, the Hutchinson/Khrapak model is a more accurate theory.

2.3.5 Neutral drag force

Neutral gas atoms provide a frictional drag force if there is a directed motion relative to the microparticles. This is known as the neutral drag force. This force is a result of the momentum transfer due to direct ballistic collisions of the microparticles with the neutral gas atoms in the plasma. Since this is a frictional force, the magnitude of the force increases with the speed of the microparticles relative to the neutrals as they collide with more gas atoms. This force can be modelled by the Epstein damping formula first derived for Millikan's famous oil drop experiment as follows [76]:

$$\mathbf{F}_n = -m_d \mathbf{v}_d \gamma_{Ep} \tag{2.34}$$

with

$$\gamma_{Ep} = \delta_{Ep}\sqrt{\frac{8}{\pi}}\frac{P}{a\rho_d v_{th,n}} \tag{2.35}$$

as the Epstein damping coefficient. Here, P is the gas pressure, a is the particle radius, ρ_d is the mass density of the particles, $m_d \propto a^3$ is the mass of the dust particles, and $v_{th,n} = \sqrt{k_B T_n/m_n}$ is the thermal speed of the neutral gas atoms. As a result, we have

$$F_n \propto a^2, \tag{2.36}$$

such that the neutral drag force increases for increasing particle size. The force also depends on how the neutral gas atoms are reflected from the microparticle surface, which is accounted for by the

Gases	Argon		Neon	
Radius / Pressure	10 Pa	20 Pa	10 Pa	20 Pa
1.7 μm	35.8 Hz	71.6 Hz	25.5 Hz	50.9 Hz
3.4 μm	17.9 Hz	35.8 Hz	12.7 Hz	25.5 Hz

Table 2.1: Dependence of the Epstein damping coefficient, γ_{Ep}, on gas pressure and particle radius for argon and neon. Increasing gas pressure increases γ_{Ep}, whereas increasing the particle radius decreases it. For the same parameters, argon has a larger γ_{Ep} than neon as argon atoms are much heavier.

parameter δ_{Ep}. The value of the dimensionless constant δ_{Ep} has been experimentally measured to be $\delta_{Ep} = 1.44 \pm 0.19$ for MF particles suspended in argon gas using the vertical resonance method [83].

In experiments, it is most common to use either argon or neon as the working gas. The Epstein damping coefficient depends on the type of working gas used, as shown in Table 2.1. Argon atoms ($m_n = 6.6 \times 10^{-26}$ kg) are much heavier than neon atoms ($m_n = 3.4 \times 10^{-26}$ kg). This means that for the same gas temperature, the neon atoms will have a $1.4\times$ larger thermal velocity than argon atoms, and hence have a $1.4\times$ smaller damping coefficient, leading to a $1.4\times$ smaller neutral drag force under otherwise identical conditions.

2.4 Important frequencies

The Epstein damping coefficient determines the damping rate of particle dynamics. As this frequency is increased, particle dynamics get damped out more strongly. Similarly, there are a few other important frequencies to consider in order to characterise the system. Amongst these is the data collection frequency, which is important to note for determining the measurement capabilities. Given the data sampling rate, the highest frequency that can be accurately resolved is the Nyquist frequency, given by half the sampling rate. Any signal at a frequency higher than the Nyquist frequency will not be reconstructed fully or without distortion. As such, the Nyquist frequency is often also called the Nyquist *limit*, and no frequency in the data analysis should be higher than it. Furthermore, the frequencies associated with a particle crossing the interparticle distance and its own diameter depend on the particle velocity. They are different depending on whether particles are in thermal equilibrium, or turbulent, or part of a directed flow. For instance, in a turbulent simulation the frequencies of a particle crossing the interparticle distance and its own diameter are $\sim O(100\ \text{Hz})$ and $\sim O(3000\ \text{Hz})$, respectively.

2.4.1 Plasma frequency

Arguably one of the most important frequencies in a plasma is the frequency of charge density oscillations, given by the plasma frequency

$$\omega_x = \sqrt{\frac{n_x q_x^2}{\epsilon_0 m_x}}, \tag{2.37}$$

where the subscript $x \in \{i,\ e,\ d\}$ refers to the different charge species of ions, electrons, and dust in the plasma.

The frequency of the density oscillations is inversely proportional to the square root of the mass of the species, $\omega \propto m^{-1/2}$. This means that the more massive the charged species is, the slower its density fluctuates in the plasma. As the dust particles are orders of magnitude heavier than electrons or ions, the dust plasma frequency is much lower, with $\omega_d \ll \omega_i \ll \omega_e$.

	Radius			Charge		
	Scaling	1.5 μm	3.0 μm	Scaling	-2500 e	-5000 e
γ_{Ep}	a^{-1}	40.6 Hz	20.3 Hz	-	40.6 Hz	40.6 Hz
ω_d	$a^{-1.5}$	493.9 Hz	174.6 Hz	q	411.6 Hz	823.1 Hz
Ω_E	$a^{-1.5}$	285.1 Hz	100.8 Hz	q	237.6 Hz	475.2 Hz

Table 2.2: Dependence of frequencies on particle radius (assuming a charge of -3000 e) and charge (assuming a radius of 1.5 μm). The particle number density is taken to be $n_d = 2 \times 10^{11}$ m^{-3} at 10 Pa in argon gas.

2.4.2 Einstein frequency

The rattling frequency of particles in the 'cages' formed by their nearest neighbours is known as the Einstein frequency. This is a resonant frequency generally only defined for crystals. However, particles in fluids can be thought of as being confined in temporary cages made by their nearest neighbours, hence making it relevant for fluids too. This frequency essentially indicates the rate at which energy and momentum get redistributed in the system. As such, the Einstein frequency is related to the plasma frequency by the following relation for Yukawa fluids [84]:

$$\Omega_E \approx \frac{\omega_d}{\sqrt{3}}. \tag{2.38}$$

The exact value of the proportionality factor depends on how strongly the interparticle interactions are screened, but the value of $1/\sqrt{3}$ is generally used [84, 85].

2.4.3 Comparison of frequencies

A comparison of some of the frequencies is shown in Table 2.2 and how they depend on particle radius and charge. As shown, in complex plasmas the Epstein frequency is typically smaller than the Einstein frequency. In this example, it is smaller by a factor of about $4 - 5$. It can even be up to two orders of magnitude smaller [86, 87]. Comparing the damping and the Einstein frequency in complex plasmas can help estimate how damped the system of microparticles is. The dependence on particle radius can also be seen in this table: larger particles are heavier, hence the associated frequencies are slower. Conversely, particles with a higher charge have stronger interparticle interactions and thus higher frequencies.

2.5 Diagnostic parameters

Beyond the factors I have already discussed, certain dimensionless parameters are required to characterise the system. As previously mentioned, the microparticles collect electrons on their surfaces and become highly negatively charged. If the ratio of the interparticle potential energy to the kinetic energy is larger than unity, the microparticle system is said to be strongly coupled. This ratio, Γ, is known as the *coupling parameter* and is given by

$$\Gamma = \frac{q^2}{4\pi\epsilon_0 \Delta k_B T_d}. \tag{2.39}$$

Here q, T_d, and Δ are the microparticle charge, temperature, and average interparticle distance respectively, with ϵ_0 and k_B as the vacuum permittivity and the Boltzmann constant. Often in complex plasma experiments, the subsystem of microparticles is *strongly coupled* as $\Gamma >> 1$.

The second parameter often used alongside Γ is known as the *screening parameter*, given by the ratio of the average interparticle distance, Δ, to the Debye length, λ_D: Δ/λ_D. It determines the strength and range of the interparticle interactions.

For flowing complex plasmas, diagnostic parameters from conventional fluid mechanics such as the *Reynolds number* and *Mach number* are used to characterise the flow. The Reynolds number, $\Re$, measures the ratio between inertial and viscous forces on the system. It is given by

$$\Re = \frac{vL}{\nu}, \tag{2.40}$$

where v is the flow velocity of the particles, L is a characteristic length, and ν is the kinematic viscosity. The Reynolds number is an important parameter to consider when studying turbulence. In conventional fluid dynamics, turbulence usually occurs in flows with a high Reynolds number of $\Re \sim O(1000)$ [88, 89]. However, low $\Re$ turbulence has been observed in multiple biological systems and active matter [90]. In complex plasmas, low-$\Re$ turbulence can be observed around $\Re \sim O(10)$.

Another parameter used to characterise flows, similar to conventional fluid mechanics, is the Mach number, $\mathcal{M}$. It is the ratio of the flow speed, v, to the speed of sound in the system, C_s, and is given by

$$\mathcal{M} = v/C_s. \tag{2.41}$$

A flow is called *subsonic* if $\mathcal{M} < 1$, *supersonic* if $\mathcal{M} > 1$, and sometimes even *hypersonic* if $\mathcal{M} \gg 1$ [91]. Multiple experimental and computational studies of supersonic flows in complex plasmas have been conducted so far [92–95].

2.6 Collective effects

Complex plasmas are ideal model systems to study a wide range of emergent phenomena [27]. Here, I will review the literature on the various collective effects which will be discussed in this thesis.

2.6.1 Shock fronts

The formation and propagation of shocks has been studied extensively in complex plasma experiments and simulations over the years [96–102]. These are wavefronts that travel through the medium at a supersonic velocity. The two types of shock fronts I will focus on are Mach cones and bow shocks, which can be produced by a supersonic flow past an obstacle.

Mach cones can be used as a diagnostic tool to get information on several relevant parameters for describing conditions in a complex plasma [103]. A Mach cone can be described by its opening angle of the cone, θ, which is related to the Mach number in the following way:

$$\sin\theta = \frac{1}{\mathcal{M}} = \frac{\mathrm{v_{sound}}}{\mathrm{v_{flow}}} = \frac{C_s}{v}. \tag{2.42}$$

Through the above relation, knowing the opening angle of the Mach cone and the relative speed between the obstacle and the flow allows for an experimental determination of the speed of sound in the system. This can then be compared to the theoretically predicted speed of sound, given as

$$C_s = \sqrt{\frac{Z_d k_B T_d}{m_d}}. \tag{2.43}$$

Sometimes, the conditions in a complex plasma are inhomogeneous in space or vary over time, and as such the shape of the Mach cone can become curved to form a *dynamical* Mach cone. By looking at the shape of a Mach cone - whether it is conical, convex, or concave - deviations in plasma

conditions can be traced [103, 104]. The general expression for using a Mach cone to find the speed of sound (assuming homogeneity in space) at a given time t_0 is

$$C_s(t_0) = v\frac{\left|\frac{\partial y}{\partial x}\right|}{\sqrt{1+(\frac{\partial y}{\partial x})^2}}, \tag{2.44}$$

where $\frac{\partial y}{\partial x}$ is the gradient at a given point on the Mach cone wavefront at Vt_0 which was excited at time t_0. In the limit of the Mach cone shape approaching a conical shape (as opposed to convex or concave, and in the limit of constant speed of sound) the previous relation $C_s = v\sin\theta$ is recovered.

The other variety of shock fronts that can be observed are *bow shocks*. Observations of bow shocks generated in a 2D complex plasma flow past an obstacle were first reported in 2012 in experiments and simulations by Nakamura et al. [105]. In fluid dynamics, a bow shock is defined to be a curved bow-shaped disturbance wave in front of the obstacle accompanied by an abrupt change in flow speed, temperature, and density. An identifying feature of a bow shock is the nearly discontinuous change in flow speed as the flow decelerates to keep the mass around the obstacle constant [106], and to balance the dynamical pressure from the incoming flow with the increased thermal pressure.

2.6.2 Turbulence

Another collective effect observed in complex plasmas is turbulence, seen in both experiments [38, 41, 43] and simulations [40], as well as in 2D [107–110] and 3D [42, 111]. One of the main difficulties with studying this topic is that 'turbulence' is ill-defined. There exists no clear definition, rather only signatures and clusters of dynamic behaviour that are widely recognised to be associated with turbulence. The generally accepted signatures of turbulence are as follows: turbulent flows are chaotic, rotational, diffusive, resistive, and self-similar.

Chaotic flow

Turbulence is characterised by flow irregularities in the form of rapid changes in velocity vectors, temperature, pressure, density, etc. These high frequency random fluctuations in flow parameters across space and time are often referred to as *intermittency* in the case of fully-developed turbulence [112]. Intermittency also exists in flows during the transition to turbulence, manifesting as transient turbulent puffs that form and decay over space and time.

Rotational flow

Turbulent flow has non-zero angular momentum. It is accompanied by eddies and swirls, known as vortices. A way to quantify how many vortices there are in the flow is to calculate the flow vorticity, which is defined as the curl of the flow velocity

$$\boldsymbol{w} = \nabla \times \boldsymbol{v} \quad \text{where} \quad \begin{pmatrix} w_x \\ w_y \\ w_z \end{pmatrix} = \begin{pmatrix} \frac{\partial}{\partial y}v_z - \frac{\partial}{\partial z}v_y \\ \frac{\partial}{\partial z}v_x - \frac{\partial}{\partial x}v_z \\ \frac{\partial}{\partial x}v_y - \frac{\partial}{\partial y}v_x \end{pmatrix}. \tag{2.45}$$

Vorticity is a three-dimensional quantity. Even for a 2D flow along x and y with $v_z = 0$, the vorticity vector has a non-zero z-component, w_z. Turbulence therefore, by strict definition, is always a 3D phenomenon. Two-dimensional studies of turbulence are always 'quasi-2D' with some degree of restricted motion in the third dimension, albeit negligible. To be technical, purely 2D turbulence does not and *can not* exist physically [113]. However, many physical systems (such as geophysical [114] or planetary [115] systems) benefit from being modelled after it. Constraining the system to two spatial dimensions to study turbulence results in a completely different phenomenology. In this work, I solely focus on 3D turbulence.

Diffusive flow

Turbulent flows exhibit a higher rate of fluid mixing than laminar flows. As a laminar flow is characterised by smooth sheets of flow with parallel velocity vectors, there is very little fluid motion perpendicular to the flow direction. This results in very little mixing between the fluid layers. On the other hand, turbulent flow contains vortices and a non-zero angular momentum. The three-dimensional vorticity of the flow causes an increased mixing of the fluid layers in the directions perpendicular to the flow direction. The mixing of fluid in turbulence is also known as *turbulent diffusion*. This is because the mean square displacement of the particles grows linearly with time, which is characteristic of diffusion. Turbulence enhances diffusion in the system, in the sense that the turbulent diffusion coefficient (characterising the diffusion due to the vortices) is always greater than or equal to the molecular diffusion coefficient [116]. Interestingly, over long time scales, turbulent flows have also been observed to display *anomalous diffusion*, where the mean square displacement grows non-linearly with time as either a superdiffusive (faster than time) or subdiffusive (slower than time) flow [117].

Resistive flow

Turbulence creates drag. It is well known that turbulence results in an increased flow resistance compared to laminar flow [118]. This has been demonstrated many times, for example through direct measurements in experiments with air flowing through capillary tubes [119]. In the original experiments performed by Reynolds in 1883 [120], the flow resistance (measured via pressure gauges) was observed to be directly proportional to flow velocity, $\propto v$, in a laminar flow and to the square of the flow velocity, $\propto v^2$, in a turbulent flow.

Self-similarity: Energy cascades

In a turbulent flow, vortices transfer turbulent kinetic energy from larger to smaller spatial scales until the energy is dissipated into heat through the molecular friction within the fluid, as shown by Kolmogorov in 1941 [121, 122]. This is illustrated in Fig. 2.1. The largest vortices, of size l_0, carry energy down the spatial scales as their radial size decreases until they are of the size η, which is known as the Kolmogorov length scale. The range of length scales between l_0 and η is known as the *inertial range*. For length scales within the inertial range, the power spectrum of energy cascades follows the power law $E(k) \propto k^{-5/3}$, where k is the wave-number representing length scales. The equivalent power law $E(f) \propto f^{-5/3}$ is true for energy dissipation in time, where f represents frequency[2].

The Kolmogorov length scale η is one of the *Kolmogorov microscales*, along with the Kolmogorov time scale τ_n. These microscales are length and time scales where viscosity becomes dominant and leads to the dissipation of kinetic energy into heat. Kolmogorov showed that these microscales are universal and only depend on two important parameters: the viscosity, ν, and the mean rate of kinetic energy dissipation per unit mass, ε.

The Kolmogorov microscales are thus given by the relations [125]:

$$\eta = \left(\frac{\nu^3}{\varepsilon}\right)^{1/4} \quad \text{and} \quad \tau_n = \sqrt{\frac{\nu}{\varepsilon}}, \tag{2.46}$$

where $\varepsilon = \frac{1}{2}\frac{\partial}{\partial t}\langle \mathrm{v}^2 \rangle$. These microscales mark the smallest scales of turbulence, and hence mark the theoretical minima for length and time (maxima for k and f) where the power spectra of energy cascade is expected to follow the power law.

[2]Interestingly, a turbulent power spectrum can be found when analysing *The Starry Night* by Vincent van Gogh! The power spectrum of luminance averaged over the red-green-blue channels shows a power law consistent with supersonic turbulence found in molecular clouds of star-forming regions in the cosmos [123, 124].

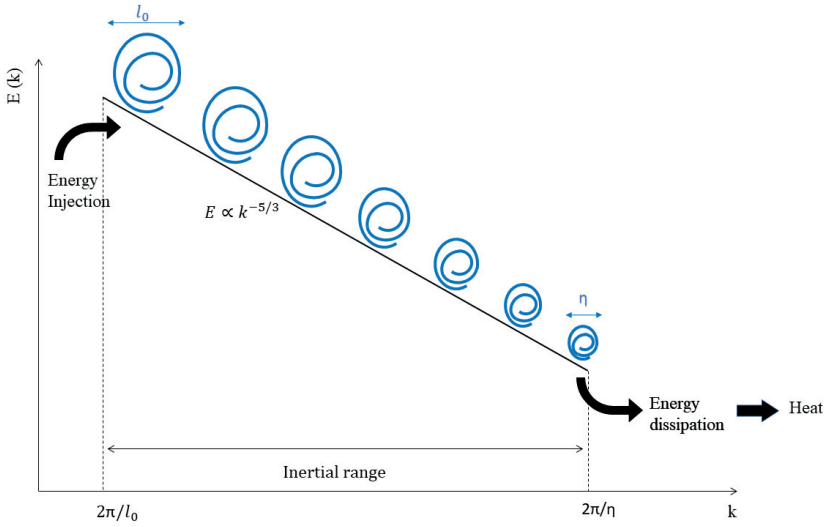

Figure 2.1: Sketch showing how vortices transfer energy from larger scales to smaller scales in 3D isotropic turbulence. As the radial length of the vortex decreases, it carries energy to smaller spatial scales. Simultaneously, the vortex is is stretched thinner in the perpendicular dimension (not shown here) to conserve angular momentum in a process known as *vortex stretching*. This transfer of energy to smaller scales happens without loss until the vortex cross-section reaches the size of the Kolmogorov microscale, η, at which point it decays as the energy is converted into heat.

Energy cascade in turbulence is driven by vortices, in a process known as *vortex stretching* [126]. A three-dimensional vortex with a given radial length carries its energy to smaller spatial scales as its radial size decreases. At the same time, the vortex is lengthened along the perpendicular direction in order to conserve angular momentum. This allows for an energy cascade through spatial scales without loss, until the radial size of the vortex reaches the Kolmogorov dissipation length, η. At this point, the energy carried by the vortex converts to heat through dissipation and the vortex fades. The energy cascade through the spatial scales can be calculated by considering the *turbulent velocity* and *turbulent kinetic energy* carried by the vortices. The velocity of a flow can be broken down via Reynolds decomposition into a mean part, $\overline{\mathbf{v}}$, and a fluctuating part, $\mathbf{v}'$. The turbulent velocity and turbulent kinetic energy can thus be defined as:

$$\mathbf{v}' = \mathbf{v} - \overline{\mathbf{v}} \quad \text{and} \quad \mathrm{TKE} = \frac{1}{2} m \mathrm{v}'^2, \tag{2.47}$$

where $\mathbf{v}'$ is the fluctuating part of the flow used to calculate the power spectra in space, and $\overline{\mathbf{v}}$ is the local Reynolds-averaged flow velocity such that $\langle \mathbf{v} \rangle = \overline{\mathbf{v}}$ and $\langle \mathbf{v}' \rangle = 0$. To calculate $\overline{\mathbf{v}}$ in this work, the turbulent region was divided in 3D bins of size $(250\ \mu\mathrm{m})^3$ where the flow velocity was averaged over one second. This is more suitable than averaging over the entire spatial region in order to separate the vortices from the non-turbulent flow deflected around the bow shock and the obstacle.

One way to calculate the power spectra is to use The Wiener-Khintchine theorem [127, 128]. The theorem states that the power spectra is the Fourier transform of the velocity correlation function. This is given by the relation

$$E(f) = \frac{1}{2\pi} \int_{-\infty}^{+\infty} e^{ifs} \Gamma(s) ds, \quad \text{and} \tag{2.48}$$

$$E(k) = \frac{1}{2\pi} \int_{-\infty}^{+\infty} e^{ikx} \langle \mathrm{v}(0)\mathrm{v}(x) \rangle \, dx, \tag{2.49}$$

where $\Gamma(s) = \langle \mathrm{v}(t)\mathrm{v}(t') \rangle$ is the velocity auto-correlation function averaged over all particles, and $s = |t - t'|$.

Damped flow: cascade rate vs damping rate

The previously discussed properties mark the hallmarks for turbulence in conventional fluids such as water, which is practically undamped. Studying turbulence in fluids with damping (such as complex plasmas) is difficult as it tends to interfere with the generation of vortices and the energy cascade. It was recently shown by Bajaj et al. [111] that it can be feasible to study turbulence despite the presence of damping. They show that for turbulence in damped systems, it is important to check whether the damping is low enough to allow for vortices to develop and continue the energy cascade before they are damped out. This is easily checked by comparing the rate of cascade, $\omega_{cas} = k\sqrt{2kE}$, with the rate of damping, γ_{eps}. If $\omega_{cas} > \gamma_{ep}$, the system is in the regime where turbulent vortices can develop and maintain an energy cascade despite the presence of damping.

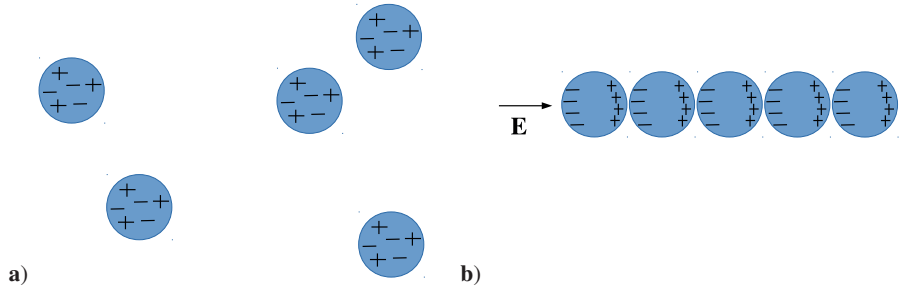

Figure 2.2: Sketch showing the polarisable particles in conventional ER fluids **a**) before and **b**) after the application of an external electric field, **E**. The electric field polarises the particle surfaces and creates an electric dipole, which causes the particles to align themselves along the direction of the field. This is the process by which string-like clusters form in conventional ER fluids.

2.6.3 Onset of electrorheology

Similar to turbulence, complex plasmas can be used to investigate the onset of certain phenomena on a kinetic level, which is not possible in conventional fluids. One such phenomenon is the change in properties of electrorheological (ER) fluids upon the application of an external electric field. This is sketched out in Fig. 2.2, which shows how the electric field polarises the surface of the particles and leads to the formation of 'string-like' structures in conventional ER fluids. Such ER properties have also been observed in complex plasmas in microgravity conditions [44, 129]. Experimental observations of complex plasma string fluids in the PK-4 facility have shown a decrease in speed of sound [60], microparticle density, as well as thickness of the microparticle suspension [48] compared to experiments without strings.

When an external electric field is applied to a fluid complex plasma, the microparticles align themselves along the direction of the field in '*string-like* clusters' (SLCs). A substantial difference between complex plasmas and conventional ER fluids is that microparticle surfaces are not polarisable.

Due to the electric shielding from the surrounding plasma, a sphere of positive charges forms around the microparticles with the radius of one Debye length. This is known as the *ion cloud*[3]. This is illustrated in Fig. 2.3**a**. These positively charged free ions have higher mobility than the microparticles. This means that the externally applied electric field has a greater impact on the ions, causing a directed ion flow relative to the microparticle and thus deforming its ambient ion cloud. This is known as 'ion focusing', which is the build-up of extra ions directly behind a particle. This build-up of positive charge in the wake region is also known as a *wake charge* or an *ion wake*, which is illustrated in Fig 2.3**b**. The development of this wake charge is what causes the microparticles to behave as though they are polarised: the negative particle and the positive wake form a dipole. Such a direct current (DC) field can cause instabilities due to the ion flux [86] such as waves and oscillations [130] as well as particle drift [74]. Often, in experiments, the polarity of the external electric field is switched back-and-forth repeatedly to produce an alternating current (AC). The electric field is alternated faster than the microparticle plasma frequency, $\omega \gg \omega_d$, but slower than the ion plasma frequency, $\omega \ll \omega_i$, which allows the ions to follow the changing field while the particles experience the time-averaged null field. This leads to a build-up of positive charge both up- and downstream of the ion flow. The deformation of the ion cloud due to an AC field is illustrated in Fig. 2.3**c**, where the particle has two positive wake charges - one on either side.

[3]It is important to note that this cloud is not attached to the particle - if the particle is moved from position A to B, the shielding cloud at A will dissipate away and a new cloud will be formed at position B.

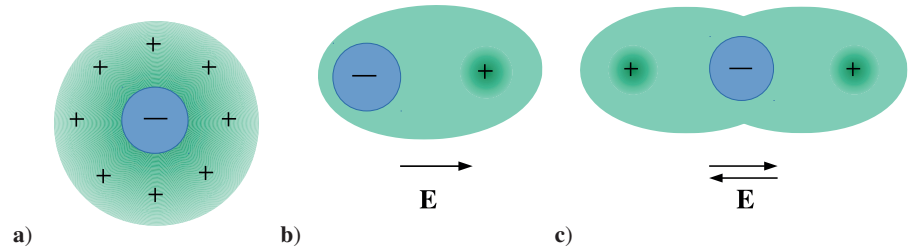

Figure 2.3: Illustration (not to scale) of ion focusing forming a positive wake charge depending on the ion drift due to the external electric field. The **a**) spherical ambient ion cloud around the microparticles gets deformed due to a DC electric field to form a **b**) positive wake downstream the particle. If an AC field is applied, the deformation of the ion cloud is symmetric on both sides of the microparticle, as shown in **c**). This is the process by which string-like clusters form in complex plasmas.

Interestingly, SLC formation seems to preferentially occur in AC fields over DC fields. Ivlev et al. found that the strings were absent in a pure DC field even under otherwise identical conditions [86]. They attribute this to a change in interparticle interactions from non-Hamiltonian (non-reciprocal) in DC and Hamiltonian (reciprocal) under an AC field. Under an external DC field, the interaction between two particles is asymmetric. The ion wake from the leading particle i changes the potential felt by the trailing particle j, however the ion wake behind particle j does not interact with particle i. This results in non-reciprocal interparticle forces, $|F_{ij}| \neq |F_{ji}|$. Due to the symmetry introduced from alternating the field, the interparticle interactions become reciprocal. The ion wake behind particle i interacts with particle j, and the ion wake in front of particle j interacts with particle i, leading to Hamiltonian interparticle interactions.

The transition from a Hamiltonian to a non-Hamiltonian system was studied for the first time in 2018 by Dietz et al. on parabolic flight experiments using the PK-4 setup [129]. The duty cycle of the current was varied from $\delta = 50\ \%$ (symmetric AC) to $\delta = 0\ \%$ (pure DC). Here, an asymmetric AC current with a duty cycle of $\delta = x\ \%$ refers to the sign of the voltage being positive $x\ \%$ of the time, and negative $100 - x\ \%$ of the time. As the duty cycle was decreased, the phase of the system was observed to continuously transition from a well-developed SLC structure to an isotropic system.

The Hamiltonian interparticle interactions in complex plasmas under an external AC field leading to SLC formation are directly analogous and mathematically equivalent to those in conventional ER fluids [44, 131]. Since the process of SLC formation in conventional ER fluids is said to be due to interparticle attraction [132], it has been theorised that the same mechanism of (effective) attraction might be causing the formation of SLCs in complex plasmas too [21, 129, 133–135]. This hypothesis will be investigated and discussed further in this work. Before presenting the results of the study, I will describe the simulation setup and analysis tools required.

Chapter 3

Overview of setups

"In most cases the tiniest differences in the initial conditions—the starting state—leads to large eventual differences in outcomes. This phenomenon is called chaos. If a system is chaotic (most are), then it implies that however good the resolving power may be, the time over which the system is predictable is limited."

Leonard Susskind [136]

The results discussed in this thesis focus on using simulations to enhance the interpretation of experiments. In this section, I will discuss the simulation setup I used for numerical modelling of complex plasmas, as well as outline the relevant experimental setups that support this work.

Computer simulations of complex plasmas are often used alongside experiments to gain a more complete understanding of the underlying physical mechanisms driving the observed phenomena. Using simulations alongside experiments enhances our understanding of complex plasma behaviour by systematically exploring a wider parameter space, identifying and testing potential underlying mechanisms, tracking each particle the entire time, and offering predictive capabilities to propose future experiments. This combined approach enables a deeper investigation of the fundamental physics of the system and facilitates the development of more accurate models and theories.

Combining experimental observations with numerical models facilitates a more comprehensive understanding of complex plasma systems, since the simulations can probe the system as well as explore phenomena in ways that are difficult to access through experiments. A powerful tool for developing computational models of complex plasmas are molecular dynamics (MD) simulations, which follow the microparticle dynamics in the plasma without simulating the plasma dynamics. This allows the runs to be fast and efficient, allowing for easy computation of the dynamics of large microparticle ensembles. MD simulations focus on individual microparticle trajectories and interparticle interactions. They can thus provide kinetic-level insights into the emergence of collective behaviour that is observed in complex plasma experiments.

A great benefit of MD simulations is that they can have orders of magnitude higher rates of data collection than is currently possible for experiments, as well as track each particle at every timestep - a level of detail that is still not achieved in experiments. Moreover, they are flexible and fast, and can therefore be made to run multiple times by systematically varying parameters to judge their effect on the microparticles. Different experimental conditions can be simulated relatively easily and can be repeatedly studied multiple times to identify key parameters and their influence on the microparticle dynamics. This systematic search through the parameter regime can help optimise and guide future experiments or constrain and shape the interpretations of currently existing data.

For all simulations presented in this work, I used an open-source classical MD software called the 'Large-scale Atomic/Molecular Massively Parallel Simulator' (LAMMPS) [137, 138]. The software was designed for smooth and efficient parallel computation, as well as for custom extensions and modifications that could be added in by the community. As a classical MD software, LAMMPS is able to follow ensembles of particles in different phases such as solid, liquid, or gas in 2D or 3D. With this software, it is possible to simulate the dynamics of up to billions of particles, depending on the computational power available. Due to these features as well as the relative ease of use, it has been commonly used for simulating complex plasmas in the past [139–144].

The simple mechanism behind these simulations involves quantising time into discrete timesteps and determining the position of each particle at a given instance in time, then calculating the forces acting on it to compute the new position and velocity of each particle. The updates to particle positions and velocities are a result of integrating Newton's equations of motion for the ensemble of interacting particles. For each particle, LAMMPS tracks a list of neighbours that it interacts with at every timestep and uses that to calculate the forces on it.

The simulations and calculations are controlled in LAMMPS via a text-based input file. The input file is read one line at a time, which means that LAMMPS does not read or compile the entire file before it begins processing. For each command line in the input file, an immediate corresponding action is taken until the input file ends and causes LAMMPS to exit.

One such example of a command that can be given in an input file is known as a 'fix'. This is any operation or action to be carried out on the microparticle system during the time-stepping process. Examples include applying forces or constraints such as a force by a laser, setting boundary conditions, controlling the temperature and pressure of the system, updating particle position and velocities, and so on. Each `fix` needs to be given a unique user-defined identification number, `ID`, as well as the ID of the group of atoms (or here, microparticles)[1] it should be applied to, `group-ID`. If there are only one type of atoms in the system, the keyword `all` can be used instead of the `group-ID`.

Once the input file is read and processed fully, the particle positions as well as the simulation settings and parameters can be saved for future use. This is done in the form of a binary restart file, which is saved to disk through the `write_restart` command. When required, this binary file can be read using the `read_restart` command at the start of a new script.

3.1 Initial simulation

The first few lines in the input file define the units, dimension, boundary, particle type, and the simulation box[2]. I used SI units for all simulations. The dimension of the simulation could either be 2D or 3D, however all results presented in this work are from 3D MD simulations. The size of the simulation box I used was different depending on the specific simulation, but its shape was always rectangular with periodic boundary conditions along all dimensions.

Once the simulation box was defined, it was possible to include microparticles. First, the type of particles to be simulated must be specified. This was done by the `atom_style` command. The choice of `atom_style` affects what quantities are stored by each atom. The default style is '*atomic*', which defines point particles with a given mass. The style '*charge*' was used in these simulations, which defines an atomic system with the additional property of charge. The particle charge was often varied, but a charge of $-3481\ \mathrm{e}$ was used as a default based on the MD simulations in [40]. Finally, the `create_atom` command was used to generate the microparticles inside the simulation box. The particles can either be generated on a defined lattice, at random positions in a given region, or individually at given spatial coordinates. Once the particles are created, the forces acting on the particles need to be specified. This will be covered in the next section.

[1] Please note that LAMMPS refers to the particles as *atoms* even though they are *microparticles*.

[2] Unless a binary restart file is being read, in which case this information is read directly from the file.

Finally, the timestep of the simulation needs to be set and the fix command to update particle positions and velocities needs to be given. In LAMMPS, the timestepping process refers to the iterative advancement of the simulation in discrete time steps. This process involves updating the positions and velocities of particles in the system based on the equations of motion. If the chosen timestep is too large, the particles can move too far and escape if their updated position is computed to be outside the boundary of the simulation box. If the timestep is too small, the simulation takes a long time to complete, and the size of the data to be processed would be very large. I chose the timestep such that it was small enough to resolve interparticle interactions (i.e. compile the neighbour list without errors), but large enough to complete the simulation within a reasonable time-frame. This was different in every simulation, but ranged between $10^{-5} - 10^{-3}$ s. The data acquisition rate (to save the particle position and velocity data) was set as 1000 FPS.

The aim for the initial simulation was to obtain a 3D microparticle suspension at thermodynamic equilibrium so that it can be used for a variety of studies. There are two main ways to do this in LAMMPS: either a given number of particles can be generated at random positions throughout a given region, or particles can be generated on a lattice within a region with a defined lattice spacing. The first method is not ideal, as particles may be generated too close to each other and experience strong enough accelerations to escape the simulation box. For this reason, I generated particles on a 3D face-centered cubic (FCC) lattice in a small region within the larger simulation box. The lattice spacing was chosen depending on the desired number density of particles in the simulation box at the end of the initialisation process. The lattice structure is ultimately irrelevant as it was melted completely before any data was collected. After generation, particles moved throughout the entire simulation box and finally reached a thermodynamic equilibrium. This was checked for by analysing the distribution of particle velocities, which will be discussed in Section 3.3.2. At this point the state of the system was saved to a binary restart file in order to be used for future simulations. An example of this initialisation process is given in Appendix A, where I initialise the simulation with a spherical obstacle in the simulation box. More details on this specific simulation can be found in Chapter 5.

3.2 Simulating forces

In the following, I will outline how the various forces acting on the microparticles can be programmed in a LAMMPS input file. The LAMMPS source code used to read and interpret the input file can be found in [138, 145].

3.2.1 Interparticle force

The interparticle force from a Yukawa potential can be implemented in LAMMPS with the use of the `pair_style coul/debye` command. The syntax used by this command is:

```
pair_style coul/debye kappa cutoff,
```

where `kappa` is the inverse of the Debye length, $\kappa = \lambda_D^{-1}$, which determines how the potential is screened, and `cutoff` is the distance at which the potential gets truncated.

The force applied to the particles is then just $F = -d\Phi_Y/dr$, where Φ_Y is the Yukawa interaction potential between two particles of charge q given by

$$\Phi_Y(r) = \begin{cases} \frac{q^2}{4\pi\epsilon_0 r} e^{-\kappa r}, & r < \texttt{cutoff} \\ 0, & r \geq \texttt{cutoff}. \end{cases} \tag{3.1}$$

The Yukawa interparticle potential as described above can also be modified. A part of this thesis requires a modified Yukawa potential so as to include the effects of the deformation of the ion shielding cloud due to a directed ion flow. This was done by including a positive point wake charge called

a *positive ion wake* on either side of the particle in the potential to mimic an alternating ion flow. The modification to the potential was made available via GitHub and can be found in [146]. The new syntax is:

```
pair_style coul/string kappa kappae cutoff wake_z wake_delta Mth
                                partd,
```

where `kappae` is the electron screening parameter, `Mth` is the ion Mach number, `partd` is the dust radius, `wake_z` is the charge of the positive wake, and `wake_delta` is the distance between the wake and the particle. More information on this modified potential is given in Chapter 6.

The cutoff distance is selected for the simulations to be several times the size of the Debye length, between $7 - 10\ \lambda_D$. At a distance of $10\ \lambda_D$ away from a microparticle, the Yukawa potential has decayed by a factor of e^{10} or 2×10^4. At such distances, the electric potential due to the microparticle is effectively zero, and so the interparticle potential is truncated in order to limit the number of neighbours that need to be considered. This greatly increases the efficiency and speed of the simulation.

3.2.2 Electric force

An electric field can be applied to the microparticles in `LAMMPS` using the `fix efield` command. The command uses the syntax:

```
fix ID group-ID ex ey ez,
```

where `ex`, `ey`, and `ez` are the three components of the simulated electric field, $\mathbf{E}$. The force applied on the microparticles is then just $\mathbf{F} = \mathbf{E}q$. An additional keyword can be added at the end of the command to modify the electric field. For instance, the keyword `region region-ID` can be used to constrain the electric field to a region in the simulation box with the specified user-given ID.

3.2.3 Laser force

Furthermore, a direct force can be applied to the particles using the `fix addforce` command. This can be used to simulate the application of an external force for targeted manipulation of the microparticles (such as by a laser) in an experiment. The command has the following syntax:

```
fix ID group-ID addforce fx fy fz,
```

where `fx`, `fy`, and `fz` are the three components of the additional force applied to the microparticles. The keyword `region region-ID` can also be used here to constrain the additional force to a certain region. Similarly, the keyword `every Nevery` can be used to pulse the force and change how frequently it is applied. The default value for `Nevery` is 1, so that the force is applied continuously.

3.2.4 Thermostat and damping

In MD simulations, thermostatting refers to the process of regulating the temperature of particles. A desired temperature is set by the user, and the thermostat adjusts the system in order to bring it to equilibrium at that temperature. The choice of the desired temperature in the thermostat depends on the specific needs of the simulation and may be changed during it. For instance, to induce crystallisation in the simulations presented in Chapter 6, the thermostat temperature was set to $300\ \mathrm{K}$ to cool down the particles. Later in the same simulation, in order to heat the particles and melt the crystal structure, the thermostat temperature was increased to $1200\ \mathrm{K}$.

Like most changes to the system in LAMMPS, thermostatting is achieved through fixes. Multiple thermostats are available, however it is most common to use a Langevin dynamics thermostat for complex plasma simulations. Interparticle interactions in complex plasmas are non-Hamiltonian[3], as in they do not strictly follow conservative or reciprocal dynamics due to the plasma being neglected. The Langevin thermostat accommodates such systems by introducing non-conservative forces, allowing for more accurate representation of the underlying physics [147].

The Langevin thermostatting in LAMMPS is based on the work by Schneider et al [148]. Langevin dynamics is a specialised form of Brownian dynamics, where random 'Brownian kicks' are provided to the particles from the background gas. The thermostat accounts for both the updated particle positions and velocities, as well as the damping from the friction with the background gas. The following syntax is used in the software to implement the thermostat:

```
fix ID group-ID langevin Tstart Tstop damp seed.
```

The thermostat changes the desired temperature at each timestep by ramping it up during the run from `Tstart` to `Tstop`. The `damp` parameter, given in units of time, determines how quickly the current desired temperature is reached. The parameter `seed`, on the other hand, is simply the seed for generating the random numbers used for providing the random Brownian kicks to the particles. The force due to the thermostat is then just

$$F_{\text{th}} \propto \sqrt{\frac{mk_BT}{\delta t \texttt{damp}}}, \tag{3.2}$$

where m is the mass of the particles specified in the simulation, T is the desired temperature, and δt is the timestep. The magnitude and direction of this force are determined by random numbers chosen from a uniform distribution.

The damping in the simulation is also accounted for within the Langevin thermostat. The thermostat applies a velocity-dependent frictional force, $\mathbf{F} = -\frac{m}{\texttt{damp}}\mathbf{v}$, to the microparticles using the damping coefficient (in time units) provided in the `damp` parameter. For all simulations, I used an Epstein damping coefficient as described in Section 2.3.5.

3.2.5 Integrating forces

The forces obtained in the previous step are used to update the positions and velocities of the particles. This can be done via the `fix nve` command, which performs a time-integration in order to update the position and velocity for particles at each timestep. The fix uses the velocity-Verlet form of the Stoermer-Verlet time integration algorithm in order to do so. This algorithm can be implemented as follows [149, 150]:

1. The timestep, which determines the granularity of the simulation, moves the simulation forward in time by a small increment, δt. First, the particle velocity is updated by only half the step duration: $v(t) \rightarrow v(t + \frac{1}{2}\delta t)$.

2. Using the updated velocity, the particle position is updated: $x(t + \delta t) = x(t) + v(t + \frac{1}{2}\delta t)\delta t$.

3. Using the updated position, the force on the particle is recalculated: $F_{t+\delta t}$.

4. Using the updated force, the acceleration on the particles can be calculated as $a_{t+\delta t} = F_{t+\delta t}/m$. In turn, the velocity of the particles is updated: $v(t + \delta t) = v(t + \frac{1}{2}\delta t) + \frac{1}{2}a_{t+\delta t}\delta t$.

[3]The microparticle subsystem is thermodynamically open. The effect from the neutrals or the ambient plasma is not accounted for in the interparticle interactions, and in experiments the particle charge can even be a function of position as it depends on the local plasma parameters. This means that $|F_{ij}| \neq |F_{ji}|$ for particles i and j.

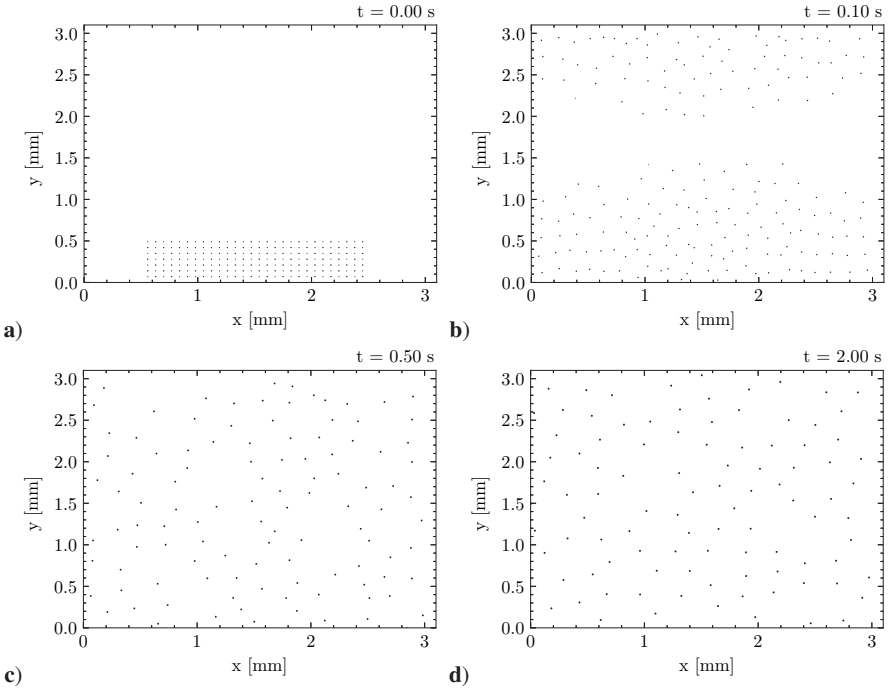

Figure 3.1: Visualisation of the microparticles in a 2D simulation slice from $0.4 - 0.6$ mm in z during the initialisation process. The figure shows **a**) the microparticles generated in a lattice structure which was **b**) subsequently melted. The particles **c**) continued redistributing energy and moving through the simulation box until they **d**) reached an equilibrium state.

The steps $1 - 4$ can be repeated iteratively for the desired number of timesteps. It should be noted that this algorithm assumes that the force on the microparticles at time $t + \delta t$ does not depend on $v(t + \delta t)$, but instead uses $v(t + \frac{1}{2}\delta t)$ if particle velocities are needed.

3.3 Determining system properties

3.3.1 Particle tracking

Each particle in `LAMMPS` is assigned a unique `id` number in order to track it and differentiate it from other particles. The data for each atom can be saved using the `dump` command. An example showing the syntax of this command is:

```
dump ID group-ID custom N file id x y z vx vy vz,
```

where the atom `id`, 3D position, and 3D velocity data is stored every `N` timesteps to a specified `file`. The given `file` determines the format of the output, which could be anything from a text file to a binary or even gzipped file. The `custom` style setting allows any valid per-atom value to be saved in the output file. Other possible values that could be saved include charge, mass, radius, angular velocity, angular momentum, and forces on each particle.

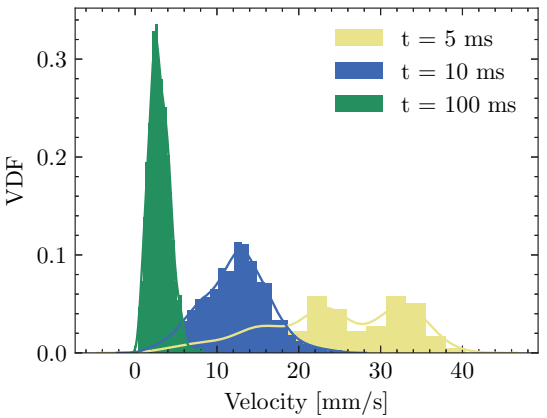

Figure 3.2: Evolution of the VDF for an ensemble of microparticles. The ensemble is not in thermal equilibrium at $t = 5$ ms, as the VDF has multiple peaks indicating hot spots and temperature gradients within the system. Energy is redistributed over time and the peaks merge into one primary peak by $t = 10$ ms. Further redistribution of heat leads to a Maxwell-Boltzmann distribution by $t = 100$ ms.

The particle positions could then be visualised either using an external program or the built-in `dump` command using the `image` style instead of the the `custom` style. In this way, the position and velocity of each particle can be tracked and saved to be used for further analysis. Using this method, the initialisation process is visualised in Fig. 3.1 in a 2D slice of the 3D simulation at $0.4 - 0.6$ mm in z. The lattice structure in 2D can be seen in Fig. 3.1**a** generated at $t = 0$ s, which was subsequently melted. The simulation box has periodic boundary conditions along all dimensions, and the particles continue moving in Figs. 3.1**b** and **c** until they reach an equilibrium state in Fig. 3.1**d**.

3.3.2 Velocity distribution function

After the lattice was melted, the microparticle ensemble relaxed towards thermodynamic equilibrium. The distribution of the microparticle velocities can provide insight into the current state of the system and whether or not they are at equilibrium. For complex plasmas, the rate of damping is much lower than the Einstein frequency (i.e. the rate of energy redistribution in the system). This means that the velocity distribution function (VDF) of an ensemble of particles at thermodynamic equilibrium is expected to be a time-invariant Maxwell-Boltzmann distribution. The VDF is normalised such that the area under the curve sums to unity, making it a probability distribution function. The temperature of the microparticles can be determined from the full width at half maximum (FWHM) of the VDF.

An example of a microparticle VDF relaxing towards a Maxwell-Boltzmann distribution is shown in Fig. 3.2. At the start of the simulation, as the lattice of microparticles is being melted, there exist multiple hot spots and temperature gradients in the system. These manifest themselves in the VDF as multiple peaks, indicating an unequal distribution of heat in the system. As heat flows from hotter regions towards colder regions, the peaks merge into one primary peak. Eventually, energy is redistributed in the ensemble and the system reaches thermal equilibrium. This is signified by the VDF resembling a Maxwell-Boltzmann distribution. Since the temperature of the particles is controlled by a thermostat, the FWHM of this distribution will continue to evolve over time until the ensemble of particles reach thermal equilibrium with the background gas, as compelled by the thermostat. Once the shape of the Maxwell-Boltzmann distribution stops evolving over time, the ensemble of microparticles is said to be in a thermo*dynamic* equilibrium.

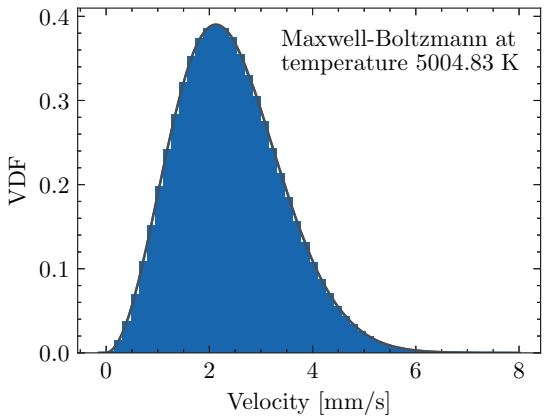

Figure 3.3: Velocity distribution function averaged over one second for an ensemble of microparticles in a simulation with argon gas at 1 Pa. The thermostat temperature is set to 5000 K. The VDF of the ensemble resembles a Maxwell-Boltzmann distribution at a temperature roughly equal to the thermostat temperature suggesting that the ensemble is at thermodynamic equilibrium.

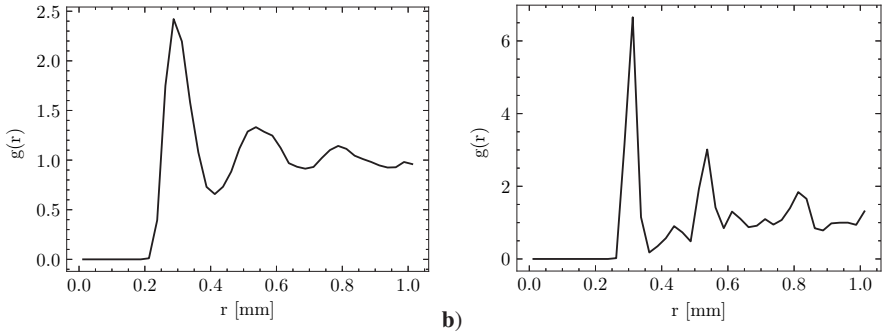

a) **b)**

Figure 3.4: The radial distribution functions (RDFs) for an ensemble of microparticles in a simulation with argon gas at 1 Pa calculated at a resolution of $\delta r = 25$ μm. The particles are at thermodynamic equilibrium at **a)** 5000 K and **b)** 500 K. The ensemble in **a)** is in a liquid state, whereas the ensemble in **b)** is crystalline.

A VDF averaged over one second for a simulation with a thermostat temperature of 5000 K is shown in Fig. 3.3. The VDF at each timestep is also a Maxwell-Boltzmann distribution with the same FWHM. As the time-averaged VDF looks like a Maxwell-Boltzmann distribution, I conclude that the particles are at thermodynamic equilibrium at the desired temperature given to the thermostat. By using the VDF of the particles in this way, it is possible to determine whether or not the simulation has been running for long enough to reach equilibrium.

3.3.3 Radial distribution function

Another useful analysis to determine system properties is to compute the distribution of particle positions. The phase of the system can be determined by its radial distribution function (RDF). This gives the likelihood, g, of finding particle i a distance r away from particle j. The particle-averaged value, $g(r)$, says how the density of particles varies as a function of radial distance from a reference particle. The RDF is defined as:

$$g(r) = \frac{1}{N} \sum_{\substack{i,j=1 \\ i \neq j}}^{N} \delta\left(r_{\mathrm{i,j}} - r\right), \tag{3.3}$$

and is normalised such that $g(r \to \infty) = 1$. The shape of this function can give insight on the cloud structure and the phase of the system. Two examples of the RDF are given in Fig. 3.4 for the same microparticle ensemble at different temperatures of **a** $5000\ \mathrm{K}$ and **b** $500\ \mathrm{K}$. The RDF in Fig. 3.4**a** has one large primary peak corresponding to the average interparticle distance, and then continues to decay in an oscillatory pattern until the amplitude of the oscillations is zero. This is representative of a liquid. Conversely, the RDF in Fig. 3.4**b** shows multiple sharp peaks, characteristic of a crystal. The RDF for a gaseous system is similar to that of a liquid, in that there is one major peak that decays to a constant value of unity, although there are no smaller peaks displaying oscillatory behaviour.

3.3.4 Viscosity calculation

Viscosity is a measure of a fluid's resistance to flow and can serve as a diagnostic tool to understand flow properties. The viscosity for a simulation at thermodynamic equilibrium can be calculated using the following Green-Kubo relation [151]:

$$\nu_{GK} = \frac{1}{V k_B T_d} \int_0^\infty \langle P_{xy}(t) P_{xy}(0) \rangle dt, \tag{3.4}$$

where V is the volume of the simulation box, k_B is the Boltzmann constant, T_d is the dust temperature, and P_{xy} is the off-diagonal element of the stress tensor which can be directly computed in `LAMMPS` as a thermodynamic quantity.

For simulations not at equilibrium, such as those including turbulent flow, the viscosity should be calculated locally. This is done by using the locally-averaged velocity of the particles, v, and the mean free path, l, as $\nu_{\mathrm{local}} \sim \frac{1}{3} v l$. The mean free path was estimated by using the average interparticle distance in the region of interest.

The viscosity values in simulations ranged from $1 - 25\ \mathrm{mm}^2/\mathrm{s}$ depending on microparticle charge, with higher charges leading to higher viscosities. Experimentally, the kinematic viscosity in 3D complex plasmas has been observed to vary between $0.8 - 300\ \mathrm{mm}^2/\mathrm{s}$ depending on the experiment, but recent measurements by Nosenko et al. in microgravity conditions estimate it to be in the range of $0.2 - 6.7\ \mathrm{mm}^2/\mathrm{s}$ [152]. For the majority of the simulations, the Green-Kubo viscosity for a fluid microparticle ensemble with a Yukawa potential was $19.1\ \mathrm{mm}^2/\mathrm{s}$. Conversely, the local viscosity for the same microparticle ensemble after the onset of turbulence was $4.1\ \mathrm{mm}^2/\mathrm{s}$ in the turbulent region.

3.4 Dangerous builds

Resolving interparticle interactions well enough and often enough was the main challenge of these simulations. If the particle accelerations were calculated to be very high - due to very large forces or a large timestep - the updated particle positions would often be placed outside the box boundary. This led to `LAMMPS` losing track of the particles as they escaped the simulation box. In this case, the simulation stops and prints out `ERROR: lost atoms`. In the majority of cases, this warning is an indication of badly resolved dynamics between neighbouring particles.

Most problems in the simulation arose from incorrectly handling the list of neighbours. The neighbour list includes every microparticle pair within the cutoff distance set by the interparticle potential plus an additional *skin* distance. The skin is the distance beyond the cutoff distance to be used when compiling the neighbour list. It mainly changes how often the list is compiled and whether or not the computation of a particle migrates to a different processor. If a microparticle moves a

distance more than half the skin distance since the last time the neighbour list was built, the current updated build of neighbours is marked as a '*dangerous build*'. This means that there is a risk of having missed an interaction between two microparticles that may have happened just before the current neighbour list build. The length scale of half the skin distance is fairly large and therefore forgiving, meaning that it is possible to have dangerous builds present without an actually incorrect list of neighbours. This also means that having zero dangerous builds guarantees that all neighbour lists were produced correctly. For this reason, only simulations with zero dangerous builds were considered in this work.

It is, however, tricky to choose the appropriate neighbour list settings. They can have a significant impact on not just the validity and accuracy of the simulations, but also on their performance and efficiency. Moreover, changing the neighbour list settings also changes the order in which the neighbours are calculated, thereby changing the forces on the particles and hence their trajectories. Building a list of neighbours is very time consuming, and so reducing the number of times a neighbour list is built can speed up the simulation drastically. However, not rebuilding the list enough times will ultimately lead to `LAMMPS` missing interparticle interactions and compromising the accuracy of the simulation. The timestep and skin distance can be changed according to what is needed for the situation. I have managed to find a 'good enough' compromise in these simulations such that they produce zero dangerous builds and are also time-efficient to run.

3.5 Comparing with experiments

Experimental results were used in this work to guide the development of simulations as well as in conjunction with them to help understand the underlying physics of the system. The particle information from the experiment is obtained via high quality video cameras. The images from these cameras then need to be post-processed and particle tracking softwares are required to extract the position and velocity data in the experiment. The following experiments are relevant to this work.

3.5.1 PK-3 Plus thermophoresis setup

The plasma chamber at the heart of the experiment is a compact cuboidal glass cuvette with a quadrilateral cross-section and parallel-plate electrodes on the top and bottom. This is outlined in Fig. 3.5 in 2D. The experiment used a capacitively coupled radio-frequency (RF) discharge, with the RF-power adjusted to produce a weak plasma with a density smaller than $10^9\ \mathrm{cm}^{-3}$. The electrodes were separated by $3\ \mathrm{cm}$. This experimental setup was located on board the ISS [69], and a modified setup to facilitate thermophoresis was located in a ground laboratory [61]. The experimental results relevant to this thesis came from the modified PK-3 Plus thermophoresis chamber on the ground. Here, gravity could be compensated in the ground-based facility by heating up the bottom electrode and cooling the top electrode to cause a temperature gradient in the chamber. The thermophoretic force then counteracted gravity to some extent and levitated the particles. Hotter neutral gas atoms close to the heated plate transferred more momentum to the particles than the colder neutral gas atoms near to the cold electrode. This caused a net upwards force on the particles in the direction opposite to the temperature gradient, and lifted the microparticle cloud.

3.5.2 PK-4 on the ISS

The experimental setup of the PK-4 lab is outlined in the schematic shown in Fig. 3.6. The main experimental setup of the PK-4 lab consists of a tubular glass chamber with electrodes on the side. The PK-4 chamber is a powerful facility to study flowing complex plasma dynamics. In addition to the DC discharge, the facility is equipped to produce an *inductively coupled* RF discharge, generated via a time-varying magnetic field by using a coil mainly used for particle manipulation.

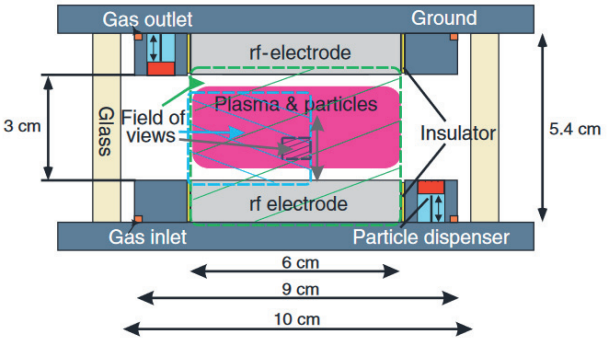

Figure 3.5: Schematic showing the 2D view of the PK-3 Plus experimental chamber. The electrodes at the top and bottom create a capacitively coupled RF discharge plasma in the central glass chamber. From [69].

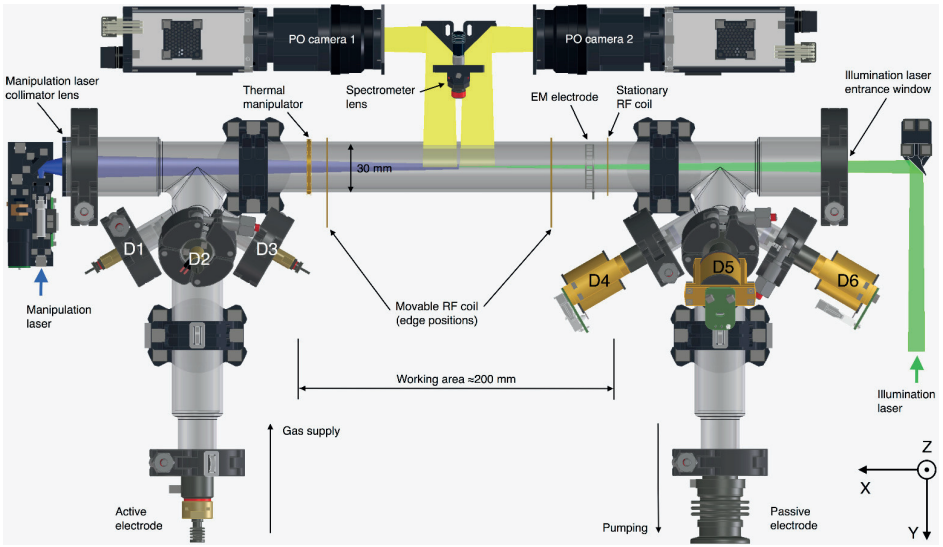

Figure 3.6: A schematic showing the PK-4 experimental setup. The central glass chamber is $3 \times 3 \times 20$ cm^3 in size, fitted with active and passive electrodes, gas supply, and vacuum pumps for plasma generation, as well as six microparticle dispensers (D1-D6). The microparticles are made visible by the illumination laser and can be observed with the moveable particle observation (PO) cameras 1 and 2. Manipulation devices such as RF coils, a thermal manipulation heater, an electric manipulation (EM) electrode, and a manipulation laser are also mounted to be used in experiments. From [70].

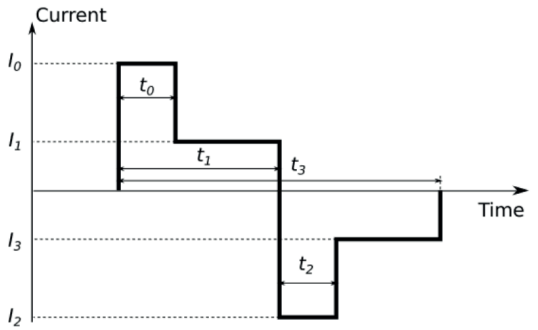

Figure 3.7: A schematic representing the waveform in the pulse generator mode of the high-voltage power supply in the PK-4 laboratory [70]. The waveform is determined by setting values for the currents $I_{0,1,2,3}$ at the corresponding times $t_{0,1,2,3}$. For instance, a DC current of I_3 can be set by setting $t_{0,1,2} = 0$. From [70].

To generate plasma within this glass chamber, first the air inside it is pumped out to create a vacuum, which is then filled with a working gas at a low pressure, either argon (Ar) or neon (Ne). Then the active and passive electrodes are used to create a DC discharge [70]. This is achieved via a high voltage power supply which outputs pulses of current with a period of $\mathcal{T}$. A constant voltage is maintained through the gas to generate either a DC or an AC current. A general waveform of the current pulse generated by the power supply is shown in Fig. 3.7. The figure shows how AC or DC currents can be produced in the experiment by varying the current values $I_{0,1,2,3}$ and times $t_{0,1,2,3}$. The DC current, for instance, can be used by setting $t_{0,1,2} = 0$ to get an output current of I_3. The AC current is characterised by its frequency, $f = 1/\mathcal{T}$, as well as the *duty cycle*, δ. The duty cycle is defined as the percentage of the period where the output current is positive, $\delta = t_+/\mathcal{T}$. Changing the duty cycle affects the electric field in the plasma and can be used to control the drift velocity of the microparticles.

3.5.3 Zyflex chamber on a parabolic flight

The Zyflex chamber is $25\ \mathrm{cm}$ high with a diameter of $27\ \mathrm{cm}$, as shown in Fig. 3.8. It is made up of three separate parts: the main chamber body, the top flange and the bottom flange. The two flanges are identical with a central and a ring electrode, and can be moved vertically. Each of the electrodes can also be operated in a pulsed discharge mode, where the pulse rate and duty cycle can be chosen as required with a minimum on/off time of $50\ \mu$s. This provides additional control over the electron temperature and number density in the plasma independently of changes to the neutral gas. A pulsed discharge is expected to have lower values of T_e and n_e compared to a continuous discharge mode, as electron density and temperature rapidly decrease whenever the plasma discharge is switched off. In this way, the desired electron temperature and density can be reached by choosing the on/off time appropriately.

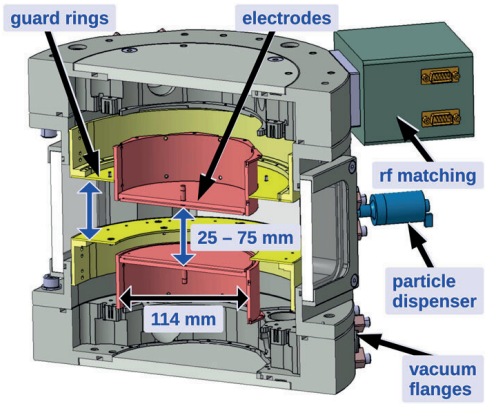

Figure 3.8: Schematic of the Zyflex chamber, a $27 \times 27 \times 25$ cm^3 cylindrical chamber with grounded guard rings shown in yellow and electrodes in red. Both the guard rings and electrodes can be moved vertically to change the chamber volume. The gas can be pumped in and out of the chamber through the vacuum flanges. From [67].

Chapter 4

Formation of droplets

"What we know is a drop, what we don't know is an ocean."

Sir Isaac Newton

Over the last few years, experimental observations have been reported of microparticles forming 'boundary-free' clusters (also known as 'Yukawa balls') under external confinement forces [153]. Recently, there have also been observations of such microparticle clusters without external confinement in different discharge conditions [27] . A microparticle cluster with a large central particle surrounded by multiple smaller particles was observed by Usachev et al. [24] in a dc discharge where the cluster was held stable due to the plasma flux onto the central particle. Compact spherical dust structures were also observed in cryogenic plasmas at $77\ \mathrm{K}$ [28, 29]. The process of forming spherical dust structures in cryogenic plasmas is known as *spheroidizing*, and has been observed at temperatures as low as $4.7\ \mathrm{K}$ [154]. Microparticle condensation into a droplet was also observed in experiments with an RF discharge by Schwabe et al. [25, 26], which will be the focus of the following sections. Investigating the formation of such a system and how to manipulate it in low temperature plasmas is becoming increasingly relevant and popular due to its applications in developing nanotechnology [155]. Despite this, not many theoretical studies have been performed to understand the cause of spontaneous microparticle condensation into *droplet-like* forms, though a few hypotheses have been put forward.

One hypothesis that has been previously suggested is the mutual shadowing of the plasma flow by the microparticles, which would lead to cluster formation in very dense clouds [156–159]. Another hypothesis is the formation of an effective positive charge due to overlapping ion clouds in the space between particles leading to reduced microparticle charge, and reduced electron density in highly dense microparticle clouds [155, 160]. A third hypothesis for how microparticles could self-confine into clusters despite the lack of external confinement suggests that it could also be an artefact of their non-reciprocal interparticle force [161].

Another hypothesis is that the ion drag force due to the ion motion past the microparticles could be responsible for the formation of droplets. My colleagues in this work and I (henceforth referred to as 'we') think the ion drag force is worth investigating in this context for two main reasons. Firstly, a key observation in the experiments listed below is that in both cases droplet formation occurred in the particle-free void. This is a particle-free quasineutral region with $n_i = n_e$ and slow sub-thermal ions. This particle-free void forms in the centre of the chamber because the ion drag force in the centre is larger than the electric confinement force and hence pushes the particles outwards [162–165]. The effect of the ion drag force on the microparticle dynamics is quite significant in the void region, and so it should be considered when discussing droplet formation in the void. Secondly, the ion drag force is well known to lead to effective attraction between microparticles and probe-like objects in the plasma [166–173], and so should be considered in the case of a droplet (which can be assumed to behave like a probe).

In this chapter, I will discuss some experimental observations of droplet formation in weightless complex plasmas. Based on these, a theoretical model was developed by me and my coauthors in the framework of the ion drag force, which is published in [174]. We tested the model by comparing the theoretically predicted results with the experimentally observed data.

4.1 Experimental observations

This work focuses on two examples of the formation of droplets in weightless complex plasma experiments. The first experiment was performed in the ground-based PK-3 Plus laboratory where the effect of gravity on the microparticles was compensated by the thermophoretic force. The second experiment was performed using the Zyflex chamber on a parabolic flight with microgravity. During both experiments, a void formed in the centre of the chamber. In both cases, the droplets only formed when the particles were pushed into this central void and then condensed into droplets.

4.1.1 Ground observations

When gravity was compensated by thermophoresis in the PK-3 Plus ground laboratory, it was observed by Schwabe et al. that microparticles in complex plasmas could condense into self-confined droplets [25, 26]. The bottom electrode of the experiment was heated in order to produce a temperature gradient in the chamber. This setup created a thermophoretic force which counteracted the force of gravity on the microparticles and resulted in an 'artificial' microgravity. Typical of microgravity experiments, a particle-free void formed in the centre of the chamber. The 'convection currents' of the background gas due to the temperature gradient [175, 176] destabilised the boundaries of this void. This led to microparticles entering the void after being accelerated from the region directly below it, and condensing into droplets. This was never observed in the PK-3 Plus chamber on the ISS, presumably because there were no convection currents to accelerate a collection of particles into the void. The droplet observed in the experiment can be seen in Fig. 4.1**a**, with $3.6\ \mu\mathrm{m}$ radius MF particles at $18\ \mathrm{Pa}$ in argon gas and a temperature difference of $\Delta T = 63\ \mathrm{K}$ between the top and bottom electrodes with a distance of $3\ \mathrm{cm}$. The spherical shape of the droplet suggests isotropic conditions in the plasma.

4.1.2 Parabolic flight observations

Recently, droplet formation was also observed in microgravity conditions during a parabolic flight experiment using the Zyflex chamber. The experimentally observed droplet can be seen in Fig. 4.1**b**. The experiment used an RF discharge plasma with an electrode distance of $75\ \mathrm{mm}$ and peak-to-peak voltage of $60\ \mathrm{V}$ in argon gas at $5\ \mathrm{Pa}$ neutral gas pressure. The experiment was performed in a *pulsed discharge* mode, with RF signals pulsing in a repeating diagonal pattern. The top ring and bottom center segments were simultaneously on for $200\ \mu\mathrm{s}$ before being switched off and allowing the top center and bottom ring segments to be turned on for the same duration of time. The reason for this pulsing mechanism was to reduce the time-averaged electron temperature [177]. The frequency of this pulsed discharge was too fast for the microparticles to be affected by it.

The plasma parameters can be obtained from the Particle-in-cell (PIC) simulations (using the `xoopic code version 2.70`, [178]) which were performed by Knapek et al [67]. These simulations were performed for the experimental setup in a *continuous discharge* mode instead, and show that the typical electron densities ranged between $1.2 - 2.4 \times 10^{14}\ \mathrm{m}^{-3}$, and electron temperatures between $2.3 - 2.9\ \mathrm{eV}$. The peak-to-peak voltage in the simulations at $40\ \mathrm{V}$ was slightly lower than the experiments, however the electrode distance and the neutral gas pressure were kept the same. No simulations were available for the pulsed discharge mode at the time of this study. Literature on the topic suggests that the plasma density should remain unchanged between the two modes, however the

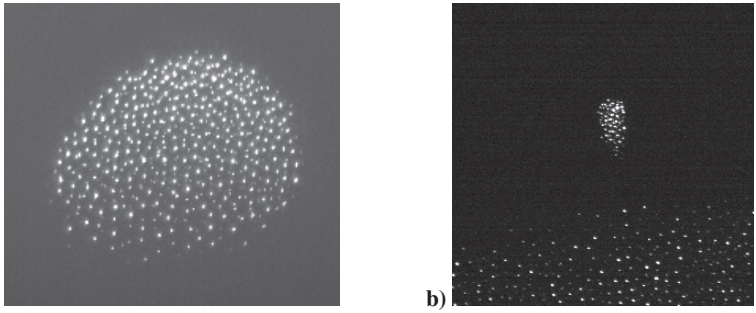

Figure 4.1: Droplet observed in **a**) the PK-3 Plus ground laboratory when gravity was compensated by the thermophoretic force (field of view: $4 \times 4\ \mathrm{mm}^2$, $3.6\ \mu\mathrm{m}$ radius particles, $\Delta T = 63\ \mathrm{K}$, argon gas at $18\ \mathrm{Pa}$). From [26], and **b**) in the Zyflex chamber during a parabolic flight under microgravity conditions (field of view: $11 \times 11\ \mathrm{mm}^2$, $2.2\ \mu\mathrm{m}$ radius particles, argon gas at $5\ \mathrm{Pa}$). The main particle cloud is visible in the bottom of the image. From [174].

electron temperature falls rapidly during the period of a pulse [179]. As such, the time-averaged electron temperature is expected to be much lower in the pulsed discharge mode than in the continuous discharge mode.

The experiment was performed with $2.2\ \mu\mathrm{m}$ radius MF particles which were illuminated in a 2D plane by a thin laser sheet. The light reflected from this quasi-2D cross-section was then recorded by cameras, resulting in the image shown in Fig. 4.1**b**. Similar to the ground-based experiment, the particles condensed into a droplet in the void. As the particles were injected into the chamber, a central void appeared and the droplet formed out of some remaining particles that were still present in the area. A quasi-2D density of the droplet within the illuminated plane was estimated to be $41 \pm 5\ \mathrm{mm}^{-2}$, which corresponds to a quasi-2D interparticle distance of $177 \pm 11\ \mu\mathrm{m}$.

The droplet in this experiment was seen to move inside the void relative to the rest of the microparticle cloud. This motion was tracked over time and can be seen in Fig. 4.2. The particles in the droplet are seen to move together as one. The colour indicates the microparticles at a given instance in time, clearly showing the relative motion of the droplet with respect to the microparticle cloud. The droplet is also seen to be more ellipsoidal than spherical, indicating anisotropic plasma conditions (presumably due to the pulsed discharge).

4.2 Theoretical model

Here we attempt to lay down a foundation to build a theoretical model for the formation of droplets. We consider a possible mechanism for this in terms of the ion drag force. The ion drag force has been extensively studied [81, 164, 180, 181], as understanding the interaction between ions and microparticles are fundamental to understanding various processes in complex plasmas, particularly in the context of stable structure formation or immersion of probe-like bodies.

We propose the following mechanism: once a group of microparticles manage to penetrate the void, they form a sheath around them and attract ions towards them. The ions get accelerated to high streaming velocities, and thereby exert a pressure on the microparticles. This process is sketched out in Fig. 4.3. This ion pressure is higher on the 'outside' of the microparticle collection than it is 'inside' (or in the region between the microparticles). This remains true as long as the microparticles are close enough that they do not need to be treated as isolated particles. In this work we will disregard the effect of charge cannibalism and ion shadowing in order to test whether this simple hypothesised mechanism is valid.

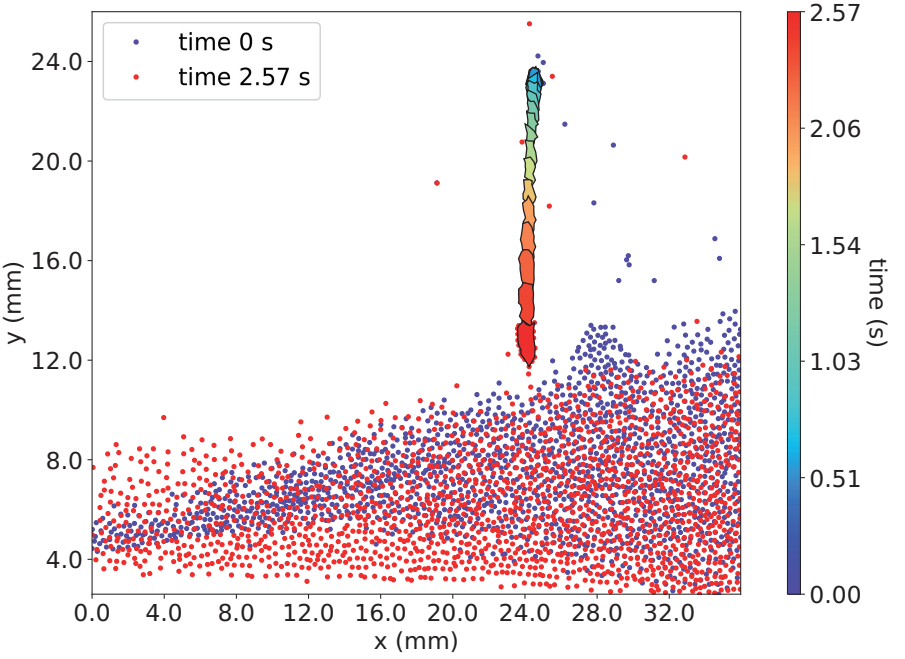

Figure 4.2: Superposition of particle positions over time with colours used to indicate a single instance in time. The droplet is moving down relative to the main microparticle cloud in the bottom. Only the first (blue) and final (red) frame of the particle positions in the main cloud are shown. The droplet is shown with filled contours above the cloud. From [174].

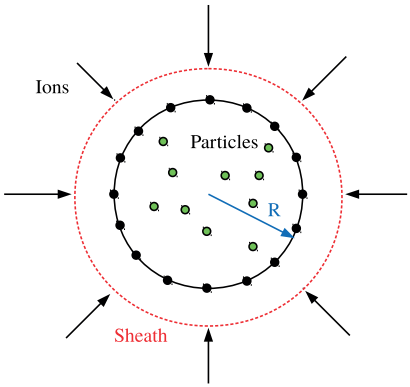

Figure 4.3: Sketch showing a droplet with microparticles bounded by a spherical surface with radius R with a sheath around the droplet (not to scale). Ions enter the sheath at the Bohm velocity such that the shielding is entirely due to electrons and the resulting sheath is thin. The particles on the droplet surface (black) experience an inwards force due to the ions, and an outwards force due to the electric repulsion from the particles inside the droplet (green), resulting in a stable structure.

We expect the anisotropic pressure from the ion flux to push the particles closer together. Since all the particles are strongly negatively charged, they repel each other more the closer they get. The decreasing interparticle distance causes an increase in electric repulsion. This repulsive force increases in magnitude until it reaches a balance with the force due to the ion flow. Once a balance is reached, the microparticles are said to have "*condensed into a droplet*". Whether this equilibrium state is stable or unstable can be tested using a thought experiment. The equilibrium state is reached when the two forces due to the inward ion pressure and the outward electric repulsion are balanced. Disturbing the equilibrium state by increasing the inward ion pressure would force the particles to move closer together. This, in turn, would lead to an increased electric repulsion and the outward repulsive force would increase to match the higher ion pressure, thereby returning to the equilibrium state of balanced forces. Disturbing the equilibrium state in the other direction by reducing the ion pressure would cause the particles to move away from each other. This would reduce the electric repulsion until the outward repulsive force is once again in equilibrium with the inward ion pressure. Disturbing the equilibrium in either direction leads the system back to equilibrium, thus demonstrating that the droplet is in a state of a stable equilibrium.

We can now develop the theoretical model by deriving the forces on a particle at the droplet boundary and studying the dependence of the droplet radius on the various plasma parameters. We will then test the hypothesised mechanism by comparing and checking its consistency with experimental observations.

4.2.1 Parameter regime

Before describing the theoretical model, the parameter regime being investigated and the relevant length scales need to be described. The theoretical results are calculated with parameters from the parabolic flight experiment for comparison.

The smallest length scale is given by the particle radius, $a = 2.2\ \mu\mathrm{m}$. From the experimental data, the average interparticle distance inside the droplet is of the order $\Delta \sim 100\ \mu\mathrm{m}$. We assume a homogeneous particle density inside the droplet. Based on the PIC simulation of the experiment, the electron number density is estimated to be $n_e \sim 2 \times 10^{14}\ \mathrm{m}^{-3}$. The electron temperature is taken to be $k_B T_e \sim 1\ \mathrm{eV}$ despite the estimate from the PIC simulation for continuous discharge being $k_B T_e \sim 2$ eV because the experiment was performed using a pulsed discharge, which is expected to have a lower temperature than a continuous discharge. This resulted in an electron Debye length of $\lambda_{De} \sim 500\ \mu$m.

The radius of droplets was experimentally observed to be of the order of a few millimetres, $R \sim 1\ \mathrm{mm}$. To estimate how many particles it contains, we assume a cuboidal packing of microparticles within the droplet such that the number density of particles $\sim \Delta^3$. This implies

$$\frac{1}{\Delta^3} = \frac{N}{\frac{4}{3}\pi R^3}, \quad \text{thus} \quad \Delta^3 = \frac{4\pi}{3N} R^3. \tag{4.1}$$

This allows us to estimate the number of particles contained in a droplet as

$$N = \frac{4\pi}{3}\left(\frac{R}{\Delta}\right)^3. \tag{4.2}$$

This results in a few thousand particles in a millimetre-sized droplet. To calculate a rough estimate of the equilibrium radius, we will assume $N = 1000$.

4.2.2 The ion drag force

As the next step, we derive an expression for the ion drag force acting on a particle at the droplet surface.

We assume that an isolated self-contained droplet inside the bulk plasma effectively acts as an object (or a probe) immersed in the plasma. As a result, the droplet's electric potential is negative with respect to the surrounding plasma, thus causing a flow of ions towards it. This leads to the formation of a sheath between the bulk plasma and the droplet. The thickness of this sheath is usually of the order of the screening length. Ions travel through the sheath at velocities so high that they do not contribute much to shielding. Since most of the shielding is from the electrons, the Debye length (and hence the thickness of the sheath) is given by $\lambda_D \simeq \lambda_{De} = 500\ \mu$m. As the thickness of the sheath is smaller than the droplet size, we can say that the sheath is "*thin*".

Ions enter the sheath with a velocity which must be greater than or equal to the Bohm velocity [73], $v_{\rm Bohm} = \sqrt{k_B T_e/m_i}$. Due to this *Bohm sheath criterion* and the small size of the sheath in this case, the ion velocity can be estimated by $v_i \simeq v_{\rm Bohm}$ near the droplet surface. Furthermore, for such high ion flow velocities the contribution to the ion flux on a particle from the ion-neutral collisions can be neglected [74, 182]. The momentum transfer from the ions with such a velocity, and hence the ion drag force, can be estimated from [76, 80, 81, 183]

$$F_{\rm id} = n_i m_i v_i^2 \sigma, \tag{4.3}$$

where σ is the momentum transfer cross section. The two mechanisms contributing to the total momentum transfer cross section are direct collisions between ions and microparticles, and the scattering of ions from the particle's electric potential. The direct collection cross section depends just on the geometry of the particles, and is hence given by

$$\sigma_{\rm dir} = \pi a^2. \tag{4.4}$$

On the other hand, the scattering cross section from the Coloumb collisions is simply the conventional Coulomb cross section [164, 184]

$$\sigma_{\rm Coul} = 4\pi b_{\pi/2}^2 \ln\Lambda, \tag{4.5}$$

where $b_{\pi/2}$ is the ion-dust collision impact parameter such that the ions are deflected by 90° given by [76]

$$b_{\pi/2} = \frac{qe}{4\pi\epsilon_0 m_i v_i^2}, \tag{4.6}$$

and $\ln\Lambda$ is the Coulomb logarithm given as

$$\ln\Lambda = \ln\frac{b_{\pi/2} + \lambda_{De}}{b_{\pi/2} + a}. \tag{4.7}$$

We use the electron screening length λ_{De} here since for high ion streaming velocities the screening is entirely due to electrons. For ions moving at the Bohm speed, we get

$$\sigma_{\rm Coul}/\sigma_{\rm dir} = 4\left(\frac{qe}{4\pi\epsilon_0 a k_B T_e}\right)^2 \ln\Lambda. \tag{4.8}$$

The distance of closest approach (as given by $b_{\pi/2}$) between a microparticle and an ion with near-sonic speed is of the order of the particle radius, $b_{\pi/2} = qe/4\pi\epsilon_0 k_B T_e \sim a$. The value of the Coulomb logarithm can then be determined to be $\ln\Lambda \approx 5$ for the given parameter regime. As a result, the ratio of the direct collision and Coulomb scattering cross sections is found to be $\sigma_{\rm Coul}/\sigma_{\rm dir} \gg 1$. The

ion drag force is, therefore, mostly a result of Coulomb scattering. The ion drag force can thus be estimated by ignoring the contribution of direct ion-dust and ion-neutral collisions by simply using

$$F_{\text{id}} = \frac{n_i q^2 e^2}{4\pi\epsilon_0^2 k_B T_e} \ln\Lambda. \tag{4.9}$$

The momentum transfer to the particles from the electron flux has also been neglected. This is because even though their flux onto the particles is the same as the ions, they are much lighter and thus their momentum transfers are much smaller [185].

4.2.3 Force balance

Besides the ion drag force, the main force acting on the microparticles is the electric force of repulsion from interparticle interactions. The microparticles are pushed closer together by the ion drag force, and pushed further apart by the electric force. The two forces, therefore, must balance out if a stable droplet is to be formed. Since the droplet boundary is a Gaussian surface[1], as per Gauss' law the electric field at the boundary of the droplet is simply due to the sum of the charges inside the droplet[2]

$$E = \frac{qN}{4\pi\epsilon_0 R^2}. \tag{4.10}$$

The electric force acting on a microparticle at the droplet surface is then simply

$$F_e = Eq = \frac{q^2 N}{4\pi\epsilon_0 R^2}. \tag{4.11}$$

By balancing the forces in Equations (4.9) and (4.11),

$$\frac{n_i q^2 e^2}{4\pi\epsilon_0^2 k_B T_e} \ln\Lambda = \frac{q^2 N}{4\pi\epsilon_0 R^2}, \tag{4.12}$$

we see that the particle charge cancels out of the equation. Using the quasineutrality condition in the void of $n_i = n_e$ (assuming a comparably small amount of charges trapped on the microparticles) along with the definition of λ_{De} we get

$$R = \lambda_{De} \left(\frac{N}{\ln\Lambda}\right)^{1/2}. \tag{4.13}$$

This results in a droplet radius of $R \simeq 7\ \text{mm}$ for the parameters specified earlier. This value is much larger than what is observed experimentally, and can be thought of as an upper estimate of the droplet size. One reason for this is that the electric repulsion should be calculated for a particle on the droplet surface only due to its nearest neighbours. We neglected to account for the partial compensation of the electric field due to the electrons and ions inside the droplet. As the screening experienced by the ions is mostly due to the electrons, the screening is negligible in the first approximation since $\Delta < \lambda_{De}$. In this case, the repulsive force is just given by the Coulomb force between two particles at the average interparticle distance,

$$F_e = \frac{q^2}{4\pi\epsilon_0 \Delta^2}. \tag{4.14}$$

[1] A Gaussian surface is defined as a closed surface that fully encloses a 3D volume. These surfaces are used to calculate a surface integral to determine the flux of a vector field. As such, surfaces with exploitable symmetries are often chosen. Spheres and cylinders are examples of Gaussian surfaces.

[2] For a Gaussian sphere encircling N particles of charge q, Gauss' law states $\oint \mathbf{E} \cdot d\mathbf{A} = qN/\epsilon_0$.

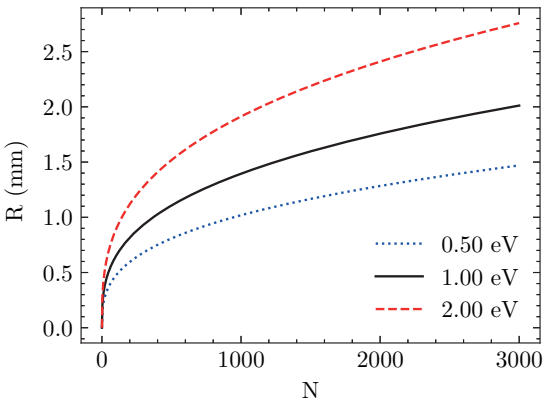

Figure 4.4: Plot of how the droplet radius depends on the number of particles inside the droplet, N, for various values of electron temperatures, $k_B T_e$ according to Equation 4.16. Lower electron temperatures at a fixed N result in better agreement with experimental data. It should be noted that our assumption that $\lambda_{De} < R$ does not hold true for $R < 0.5$ mm. Replotted from Ref. [174]

Using the relation between the average interparticle distance and the droplet radius from Equation 4.1:

$$\Delta = \left(\frac{4\pi}{3N}\right)^{1/3} R, \tag{4.15}$$

and equating Equations (4.9) and (4.14) we get

$$R = \lambda_{De} \left(\frac{3N}{4\pi}\right)^{1/3} (\ln \Lambda)^{-1/2} \tag{4.16}$$

as an equation for the lower estimate of the droplet radius. For the parameters specified earlier, this estimate yields a value of $R \simeq 1.4$ mm, which is similar to the size of the droplet observed experimentally. We have thus shown that this simple mechanism can provide an explanation for how a droplet may form in complex plasmas, and can predict its size. This simple model presented above can be tested by studying how it predicts the radius of the droplet to vary with experimental parameters, and then by checking whether it is consistent with experimental data.

Looking at Equation 4.16, the two parameters we can change are the number of particles in the droplet, N, and the electron temperature, $k_B T_e$. The number of particles is seen to vary between $O(100)$ to $O(1000)$ across experiments. In the ground-based experiment, N was observed to be between $3000 - 5000$, whereas in the parabolic flight experiment N ranged from $100 - 700$. The dependence of R on N according to our model is shown in Fig. 4.4. It can be seen in the figure that for the first few hundred particles, the droplet radius increases dramatically. This increase in radius slows down as $N \sim O(1000)$ and the curves flatten out. This tendency was also observed in experiments, where the droplet in the ground-based experiment shown in Fig. 4.1 was seen to have an order of magnitude more particles than the droplet in the parabolic flight, and yet was only larger by about 1 mm.

The figure also shows the effect of changing the electron temperature on the radius of the droplet. Fig. 4.4 plots three values of the electron temperature: 2 eV as the value predicted by the PIC simulations of continuous discharge, and 1 eV and 0.5 eV as the smaller values for the pulsed discharge. It can be seen in the figure that decreasing $k_B T_e$ decreases the radius of the droplet even if the number of particles is kept constant. In the parabolic flight experiment, the droplet radius as observed in a 2D laser sheet was estimated to be 0.9 mm $\times$ 1.4 mm in size. For a number of particles $N = 500$ and a particle radius of $a = 2.2$ μm in the droplet in the parabolic flight experiment, Equation 4.16 yields

values of $R = 0.8$ mm for $k_B T_e = 0.5$ eV, $R = 1.1$ mm for $k_B T_e = 1$ eV, and $R = 1.5$ mm for $k_B T_e = 2$ eV. These values are in agreement with the experimental observations for electron temperatures significantly lower than those predicted by the PIC simulations of a continuous discharge. The lower the electron temperature used, the better the agreement. This is consistent with the idea that the time-averaged electron temperature for experiments with a pulsed discharge are much lower than those with a continuous discharge.

We have thus demonstrated that the simple theoretical model we built from the foundation of the balance of forces can explain the formation of droplets and predict their size as seen in experiments.

4.3 Discussion and summary

The condensation of microparticles into droplets has been observed multiple times in complex plasma experiments over the recent years. Droplets in complex plasmas are different from droplets in conventional fluids because the microparticles strongly repel each other. It is therefore difficult to explain the surface tension-like effect of the formation and stability of a droplet. So far, theoretical studies on the process leading to the self-formation of these droplets have been lacking. In this work, my colleagues and I laid the foundations for a theoretical understanding of and ability to predict the structure and stability of droplets that could self-form in experiments.

We considered two observations of droplet formation: one in a ground-based laboratory and another on a parabolic flight experiment. In both cases, the microparticles got pushed into the central particle-free void and subsequently condensed into droplets. As the formation of the void is primarily attributed to the imbalance of the ion drag force and electric force on the particles, we suggested a mechanism by which the ion drag force can lead to droplet formation. Furthermore, the ion drag force is also known to lead to an effectively attractive potential between microparticles and probes in the plasma at intermediate distances from the probe.

We then developed a model based on the framework of the balance of the ion drag force as a cohesive force pushing the microparticles inside the droplet together and the electric force as a repulsive force pushing the microparticles apart. We performed a thought experiment that demonstrated that the droplet formed this way would be at a stable equilibrium, and compared its theoretically predicted radius with the experiment. The theoretical results of the droplet size agreed with the experimentally observed droplet in the parabolic flight experiment. In the 2D plane visible in the experiment, the droplet was estimated to be 0.9×1.4 mm^2. The predicted values for the droplet radius yielded by the theoretical model ranged between $0.8 - 1.5$ mm obtained assuming 500 particles in the droplet at an average electron temperature of $0.5 - 2.0$ eV. This average temperature is considerably colder than the continuous discharge PIC simulations estimate, consistent with our expectation of a lower electron temperature.

Despite the good agreement between theory and experiment, the theoretical model assumed spherical symmetry of the droplet. This is not entirely correct as the droplet in the parabolic flight experiment displayed structural anisotropies and was not spherical. This is a clear limitation of the model as it does not take these anisotropies into consideration. The radial anisotropies in the droplet suggest anisotropic plasma conditions which could be caused by the pulsed discharge used for the experiment. Since the droplet size depends on the electron temperature (which is primarily affected by the pulsing of the discharge), a different electron temperature along the horizontal and vertical directions (of the 2D illuminated plane) could be the cause of the different horizontal and vertical size of the droplet. As a crude first estimate, the vertical and horizontal directions could be treated independently, and the model can be used to predict the electron temperature in each direction depending on the droplet size. From the observed size of the droplet of 0.9×1.4 mm^2, the different electron temperatures in the horizontal and vertical directions could be estimated to be about 0.5 eV and about 2.0 eV respectively. Unfortunately, as yet there are no PIC simulations to check whether this prediction is correct, but the

model can in principle be used to predict the electron temperature in the plasma given the observation of a droplet. This allows observations of droplets to be used as a diagnostic tool to estimate the electron temperature in complex plasma experiments.

Though the first estimate is good, a future study could build on this model and explicitly account for radial anisotropies by taking into account the position of the droplet and corresponding local plasma conditions inside the void. Future studies of the experimental parameters during the pulsed discharge in the Zyflex chamber are also planned, leading to a more direct comparison with the theoretical model. The model also ignored the effects of ion shadowing and charge cannibalism. It also did not attempt to estimate the effect of the particle charge on the droplet radius, since the model is independent of particle charge. A further extension of the model could try to include the particle charge, the size of the sheath, or microparticle number density anisotropies and investigate their effect on the droplet radius and stability.

Chapter 5

Flow past an obstacle

"When I meet God, I am going to ask him two questions: Why relativity? And why turbulence? I really believe he will have an answer for the first."

Werner Heisenberg

The study of fluid flow past an obstacle has been of interest to researchers in a wide variety of fields for decades. Its relevance spans an array of disciplines, from aerospace engineering and astrophysics to bio-mechanics and oceanography. Studying the behaviour of fluids encountering obstacles in their path and how it leads to chaotic flow patterns is a well-researched problem due to it's wide applicability. As an example, it can be used to improve the design of vehicles such as cars and planes [186] or to reduce the drag and aerodynamic load on skyscrapers [187–189]. It could be used to study blood flow around clots in the human body [190], or to conduct investigations of how turbulence develops. In this chapter, I will focus on my simulations of fluid complex plasmas flowing past a spherical obstacle, a canonical problem that provides a well-defined framework for studying the onset of turbulence. The results of this study are available in the pre-print [191]. I will start by setting up the simulation, defining the geometrical and physical parameters that characterise the system.

I simulated 24225 microparticles as point charges using `LAMMPS` in a simulation box with dimensions $10 \times 3 \times 3$ mm^3 and periodic boundary conditions. Each microparticle had a charge of $q = -Z_d$ e, with $Z_d = 3481$ unless stated otherwise. The particle mass was set to 3×10^{-14} kg, consistent with particles of diameter 3.38 μm and mass density $\rho = 1510\ \mathrm{kg/m}^3$. The microparticles had an average interparticle distance of 150 μm with a Yukawa interparticle potential and a Debye length of $\lambda_\mathrm{D} = 100$ μm. The time step used in the simulations was 0.1 ms with a typical data acquisition rate of 1000 FPS[1]. Along with the interparticle force and the force driving particle flow, the force due to the Langevin dynamics thermostat [148] and due to the Epstein damping from the friction with the background gas form the main forces acting on the particles. The thermostat was set to 2000 K, and the Epstein damping coefficient [192] used corresponded to argon gas at a given pressure, mainly 10 Pa unless stated otherwise.

I mimicked the presence of an obstacle in the simulations by using a point charge of -3×10^7 e with a fixed position at the coordinates $(x, y, z) = (4.5, 1.5, 2.0)$ mm. This works on the principle that as per Gauss' law[2], the electric field due to a charged sphere is identical to that of a point charge. Therefore, simulating a point charge is equivalent to using a charged sphere as an obstacle, albeit easier. The strong negative charge of the obstacle is four orders of magnitude higher than the negative

[1]The data acquisition rate was increased to $10,000$ FPS when calculating the power spectrum in time of turbulent flow.

[2]For a charged sphere with radius R, Gauss' law, $\oint \mathbf{E} \cdot d\mathbf{A} = Q/\epsilon_0$, simplifies to Coulomb's law $E = Q/4\pi r^2\epsilon_0$ for values of r $\geq$ R. This is identical to the electric field due to a point charge Q.

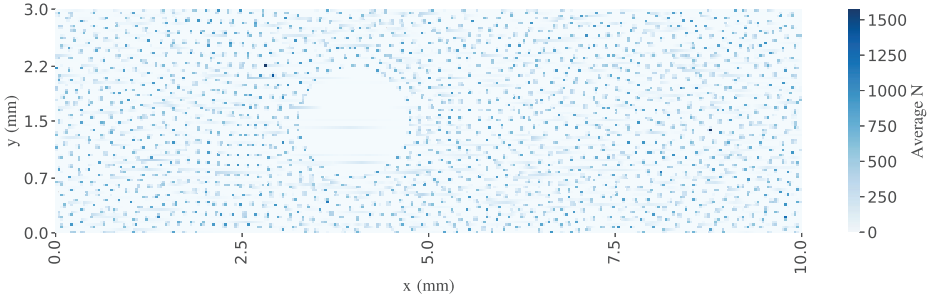

Figure 5.1: Number density plot of a 2D slice of the 3D simulation at equilibrium without a net flow of particles. The number of particles is averaged over 1 s in time in bins of size $0.03 \times 0.03 \times 0.2$ mm^3. Empty bins are coloured in white. The spherical cavity around the point charge acts as the obstacle with a diameter of 1.4 mm.

charge of the microparticles. This created a strong repulsion and led to the formation of a cavity around the point charge, consistent with what is observed in experiments [193–195]. For simulations at thermodynamic equilibrium without a flow (or with a very small flow velocity), the cavity was spherical with a diameter of 1.4 mm as can be seen in Fig. 5.1. The figure plots a 2D slice in z of the 3D simulation from $z = 1.9 - 2.1$ mm. The number of particles is averaged over 1 s in time in bins of size $0.03 \times 0.03 \times 0.2$ mm^3 to produce the number density map. In this chapter, the use of the term *obstacle* refers to the point charge and this cavity around it.

A laminar flow of particles was created by applying a constant external force to the particles in the range of $F_{\text{ext}} = 10^{-11} - 10^{-13}$ N along the x-direction depending on the desired bulk flow speed. In experiments, an external force of $F_{\text{ext}} = 10^{-13}$ N can be produced by using an electric field with a magnitude of 180 V/m. This constant external force, when balanced with the damping force, resulted in a steady laminar flow of the particles along the x-axis.

Periodic boundary conditions were used in all three dimensions of the simulation box in order to simulate an infinite laminar flow directly towards the obstacle. The size of the simulation box had to be much larger along the x-axis in order to allow the disturbances to die out before the flow encounters the obstacle again. Due to these periodic boundary conditions, there exists an infinite grid of obstacles along each dimension in the simulation. Increasing the size of the simulation box had no effect on the analysis results, and so I conclude that the infinite grid of obstacles are sufficiently far apart that they can be ignored for the purposes of this study.

There are two parameters that can be used to characterise the flow. The Mach number, $\mathcal{M} = \mathrm{v}/C_s$, can be used to characterise the flow into the obstacle at speed v. Here, $C_s = \sqrt{Z_d k_B T_d / m_d}$ is the speed of sound in the system. A flow velocity with $\mathcal{M} > 1$ is called *supersonic*, whereas that with $\mathcal{M} < 1$ is called *subsonic*. Similarly, the Reynolds number, $\Re = \mathrm{v}L/\nu$, can also be used here to characterise the resulting turbulent flow. Here, we use the flow speed, obstacle diameter, and kinematic viscosity for v, L, and ν respectively.

Both $\mathcal{M}$ and $\Re$ change with changing fluid properties such as flow speed and particle charge. As they change, the emergent phenomena in the fluid motion undergoes visible and predictable changes too. I will first review the observation and formation of shock fronts, and then analyse the resulting chaotic flow patterns that lead to fully-developed turbulence in the simulations.

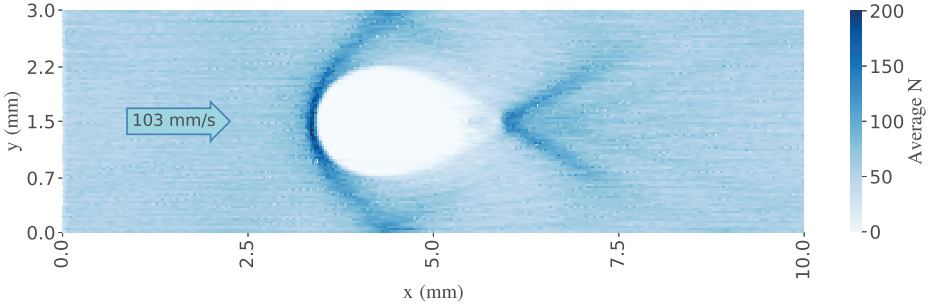

Figure 5.2: Example of shock fronts produced in the wake and fore-wake of the obstacle as seen in a 2D slice of the 3D simulation. The bulk flow speed and direction are indicated on the plot. The number of particles is averaged over $1\ \mathrm{s}$ in time in bins of size $0.03 \times 0.03 \times 0.2\ \mathrm{mm}^3$. Multiple Mach cones as well as a bow shock are clearly visible.

5.1 Shock fronts

A shock wave, or a *shock front*, is a supersonic disturbance in the flow characterised by discontinuous and nonlinear changes in fluid properties. This shock front acts as a boundary, compressing and decelerating the fluid, leading to a rapid transition from supersonic to subsonic flow. In general, the structure of shock fronts depends on factors such as $\mathcal{M}$, the shape of the obstacle, and the properties of the fluid. Higher Mach numbers result in stronger shock waves and more pronounced changes in flow properties. The geometry and size of the obstacle also influence the shock front characteristics, such as rounder or sharper objects leading to spherical or conical bow shocks respectively. I observed two distinct type of shock fronts in my simulations, namely bow shocks and Mach cones.

A bow shock is a curved hemispherical shock front that forms in front of an obstacle when it encounters supersonic flow. The abrupt deceleration of the fluid as it flows into the obstacle leads to flow compression and thus the formation of a bow shock directly in front of the obstacle. Mach cones, on the other hand, are conical shock waves that emerge behind the obstacle. They are formed due to the superposition of spherical waves generated by different points on the obstacle's surface. Similar to bow shocks, Mach cones are regions of compression that mark the boundary between supersonic and subsonic flow where the flow velocity and pressure change abruptly. The opening angle of a Mach cone depends on the Mach number of the incoming flow, with higher Mach numbers leading to smaller opening angles.

Both bow shocks and Mach cones can offer insights into the behaviour of supersonic flows and shock wave propagation, as well as plasma conditions and complex interparticle interactions. Both types of shocks were observed in these simulations to be stationary with respect to the obstacle. An example of the shock fronts observed in the simulations is given in Fig. 5.2. Multiple mach cones can be seen behind the obstacle, along with a single bow shock in front of it. These shock fronts are visible in the heatmap as regions of compression with high number density.

It is therefore possible to determine the position of the Mach cone and its opening angle, θ, directly from the number density plot. The position of the Mach cone can be tracked by finding the x and y coordinates of the bin with the highest number density. Only particles in the upper half ($x \geq 1.5\ \mathrm{mm}$) of the simulation box were considered for simplicity. An example of the Mach cone position obtained via this method is plotted in Fig. 5.3. The gradient of the linear fit is given by $\tan\theta$, resulting in an opening angle of $\theta = 30.4°$. The outlying point around $x = 7.4\ \mathrm{mm}$ and $y = 1.5\ \mathrm{mm}$ is not counted in the fit as it belongs to the secondary Mach cone. Using the relation $\sin\theta = 1/\mathcal{M}$, results in a Mach number of $\mathcal{M} \approx 2$. This can then be used to determine the speed of sound in the system, as it is

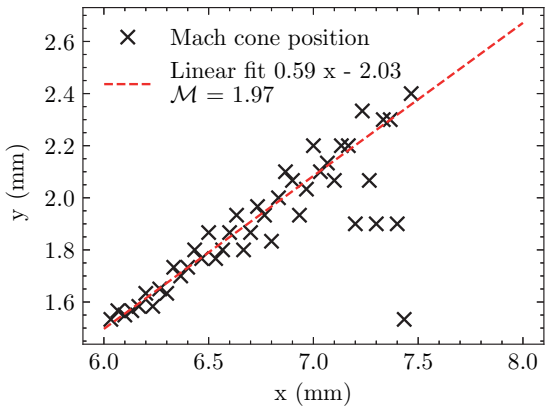

Figure 5.3: Determination of $\mathcal{M}$, and hence the speed of sound, using the Mach cone opening angle. The position of the cone was determined from the location of the bins with the highest number density. The gradient of the linear fit results in an opening angle of $\theta = 30.4°$ and a mach number of $\mathcal{M} = 1.97$.

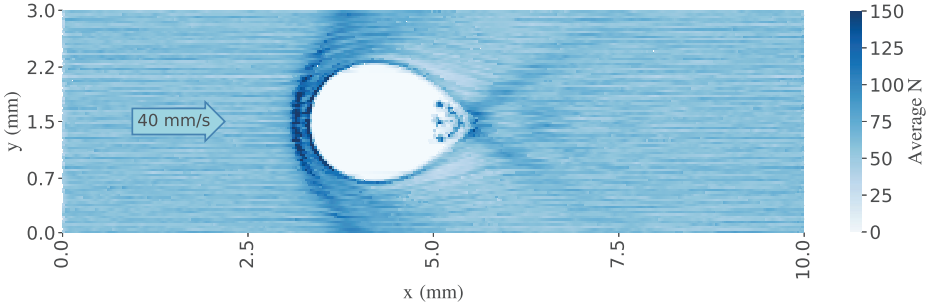

Figure 5.4: Example of a secondary 'reflected' bow shock as seen in a 2D slice of the 3D simulation. The number of particles is averaged over 1 s in time in bins of size $0.03 \times 0.03 \times 0.2$ mm^3. The particle charge used for this simulation was -2000 e with the flow speed and direction indicated on the plot.

related to the Mach number by the relation $\mathcal{M} = \mathrm{v}/C_s$. For a given flow speed of 155.7 mm/s and $\mathcal{M} = 1.97$, the speed of sound in the system with charge -5000 e comes out to be $C_s = 78.8$ mm/s. Observations of a Mach cone can thus be used to determine plasma parameters such as the speed of sound in the system.

While the speed of sound can be measured using the Mach cone opening angle, simulations with multiple Mach cones reported different opening angles for each cone. Secondary Mach cones were commonly observed to have a similar but smaller opening angle than primary cones. This is consistent with experimental observations of Mach cones in strongly-coupled dusty plasmas [93, 196, 197]. A smaller opening angle implies that the secondary Mach cones 'see' a smaller speed of sound. This may be due to the strong-coupling between the microparticles acting as a restoring force in the regions with reduced number density directly behind the primary cone.

Similar to Mach cones, bow shocks were also observed to have a multi-part structure in some simulations. Secondary 'reflected' bow shocks were observed behind the obstacle multiple times. An example of this is shown in Fig. 5.4. A possible mechanism for the development of these 'reflected' bow shocks is the formation of a recirculation zone. In a recirculation zone, the flow may reverse its direction and flow back towards the obstacle, thus forming a smaller bow shock facing in the opposite direction to the primary bow shock. This would also explain the more conical shape of the secondary

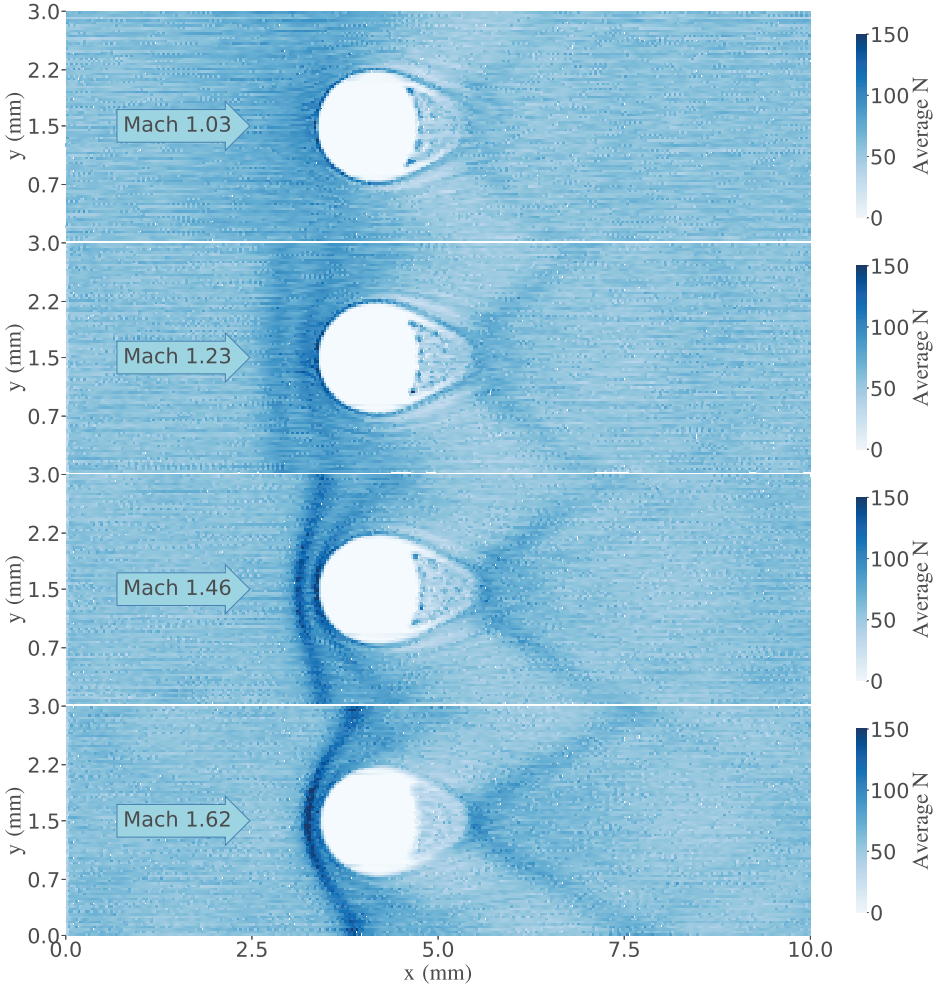

Figure 5.5: Formation of bow shocks as the bulk flow speed is increased. The flow speeds (in terms of the Mach number) and direction are indicated in the plots. Here, a particle charge of -5000 e was used. A double bow shock appears first. As the speed is increased further, the second shock collapses and only one shock front remains.

bow shock compared to the primary shock, as the cavity around the point charge is deformed by the flow to be more elongated downstream. Sharper obstacles result in conical bow shocks, whereas rounder obstacles result in spherical ones.

Another form of multi-part structure observed in bow shocks was the formation of a *double bow shock*, with two shock fronts seen in front of the obstacle. This structure was primarily observed in the process of bow shock formation. The multiple stages of the formation of bow shocks with increasing flow speeds are depicted in Fig. 5.5. As the flow speed (and hence $\mathcal{M}$) was increased, the particles in front of the obstacle were compressed further and further. The first structure to appear in this region is a double bow shock with two shock fronts. The first front is further away from the obstacle and flatter (less curved), whereas the second is closer and rounder (more curved). This sort of a structure has been observed multiple times in astrophysical plasmas[3] [198–200]. However, to my best knowledge, double bow shocks have yet to be observed in complex plasma experiments.

As the flow speed is increased further, the second shock front becomes dramatically more curved until it collapses, leaving behind the familiar shape of a single-fronted bow shock. It can also be noticed that as the flow speed increases, the secondary reflected bow shock near the Mach cone eventually disappears around the same time as the double bow shock. The flow speed may be too high for large enough recirculation zones to form in order to produce a reflected bow shock.

Increasing the flow speed even further, past the point of the development of a bow shock, triggered the onset of turbulence. The formation of shock fronts was essential in these simulations for the development of turbulence. No turbulence was observed in the region in front of the obstacle without the presence of a bow shock. This might be due, in part, to the presence of damping in the system. In a damped system, disturbances and vortices may die out before turbulence has the chance to develop. The presence of shock fronts provides a region with uncharacteristically high number density, thereby allowing stronger interparticle interactions leading to stronger disturbances. I found that I could reliably trigger the onset of turbulence in my simulations by increasing the flow speed further after the formation of shocks. This enabled investigations of the onset of turbulence in a damped system at the level of individual particles using complex plasmas.

5.2 Particle-resolved study of turbulence

As laminar flow encounters the obstacle, the flow gets disrupted and deflected around it, generating localised disturbances and vortices. As these disturbances and vortices grow and propagate, the flow becomes increasingly chaotic, eventually triggering the onset of turbulence. Using complex plasmas as the fluid makes it possible to investigate this onset of turbulence at the level of the carriers of the turbulent interactions - the individual particles. This enables particle-resolved studies of turbulence in damped systems, a task impossible to accomplish in conventional fluids such as water or air.

The main area of investigation for studies involving the flow past an obstacle is the wake-region directly behind the obstacle [189, 201, 202]. The disturbances in the region upstream from the obstacle, known as the *fore-wake*, are rarely studied [140, 203]. In these simulations, turbulence was observed both upstream and downstream of the obstacle near bow shocks and Mach cones. I have thus decided to focus on the flow in the less-studied fore-wake region instead.

Despite being one of the earliest investigated problems in physics, a complete description of turbulence is missing. Moreover, the ability to predict the onset of turbulence remains poor to this day. Turbulence is not a well defined concept [204]. It is only recognised by the characteristic patterns of fluid dynamics that accompany it [205]. The hallmarks of turbulence, as discussed in Section 2.6.2, are as follows.

[3]It should be noted that bow shocks form in astrophysical systems when the plasma flows into the magnetosphere of an obstacle, such as the Earth. There, plasma interacts with the obstacle's magnetic field to produce the bow shock. Here, the microparticles in the complex plasma interact with the obstacle's electric field instead.

In general, turbulent flow is [206]:

1. **Rotational**, and has vortices and non-zero angular momentum.
2. **Chaotic**, with high-frequency fluctuations in flow profile and velocities.
3. **Diffusive**, as the vortices increase the rate of fluid mixing.
4. **Resistive**, as it creates drag and causes an increase in flow resistance.
5. **Self-similar**, as the power law describing the energy cascade from larger to smaller spatial scales follows the relation $E(k) \propto k^n$, where $n = -5/3$ for fully developed turbulence [116].

I will use the hallmarks of turbulence listed above as a checklist or a working definition to determine whether a flow is turbulent. If all of these conditions are satisfied, I can say that the flow is turbulent consistent with the definition given above. I will review these hallmarks in the context of an example turbulent simulation. Next, I will discuss the transition of laminar flow to turbulent flow in a damped simulation. Finally, I will examine turbulence in an undamped system and compare it with previous results.

5.2.1 Evidence of turbulence

In the following, I focus on the flow in two main regions. I define a laminar region along $0 - 1$ mm in x, $1 - 2$ mm in y, and $1 - 2$ mm in z, and a fore-wake region along $2.5 - 3.5$ mm in x, $0.8 - 2.2$ mm in y, and $0.8 - 2.2$ mm in z. In this section, I will demonstrate that the flow in the fore-wake region is turbulent, consistent with the working definition.

Presence of vortices

Strong vortices are emblematic of turbulent flow. Vortices are present both upstream and downstream of the obstacle, as can be seen in Fig. 5.6. The figure is split into three parts. The number density (top), z vorticity component (middle), and kinetic energy (bottom) in a 2D slice of the simulation are averaged over 1 s in time in bins of size $0.03 \times 0.03 \times 0.2$ mm^3. The kinetic energy plot shows the kinetic energy of the particles in the rest frame of the flow, by subtracting the velocity due to the driving force from the particle velocity. This, in effect, ignores the kinetic energy due to the external driving force. Fig. 5.6 shows the time-averaged spatial distribution of vortices around the obstacle. The vorticity value in a given bin was calculated by averaging the difference in $\mathrm{v_x}$ and $\mathrm{v_y}$ across neighbouring horizontal and vertical bins respectively.

A few important observations should be made in Fig. 5.6. Firstly, there is a strong presence of vortices in the flow, satisfying Condition 1 listed above. Secondly, the position of the vortices is correlated with the position of shock fronts such as Mach cones and bow shocks. There are two main regions where vortices were generated: in front of the bow shock, and in front of the Mach cone. The primary areas for vortex generation are the regions where the incoming flow of particles is perpendicular to a shock front. In regions with high vorticity, particles either flow directly into the bow shock due to the bulk flow velocity, or they are redirected by the obstacle to flow directly into the Mach cone. This phenomenon is similar to an experimental observation of turbulence discussed in Section 2.6.2 where turbulence was induced due to particles flowing directly into a dust-acoustic wavefront [111]. Finally, the regions with high vorticity also correlate with the regions of high kinetic energy in the rest-frame of the flow. This implies that as the vortices are generated and propagated, they carry kinetic energy with them. The vortices are thus responsible for the transfer of energy from larger scales to smaller scales in an energy cascade.

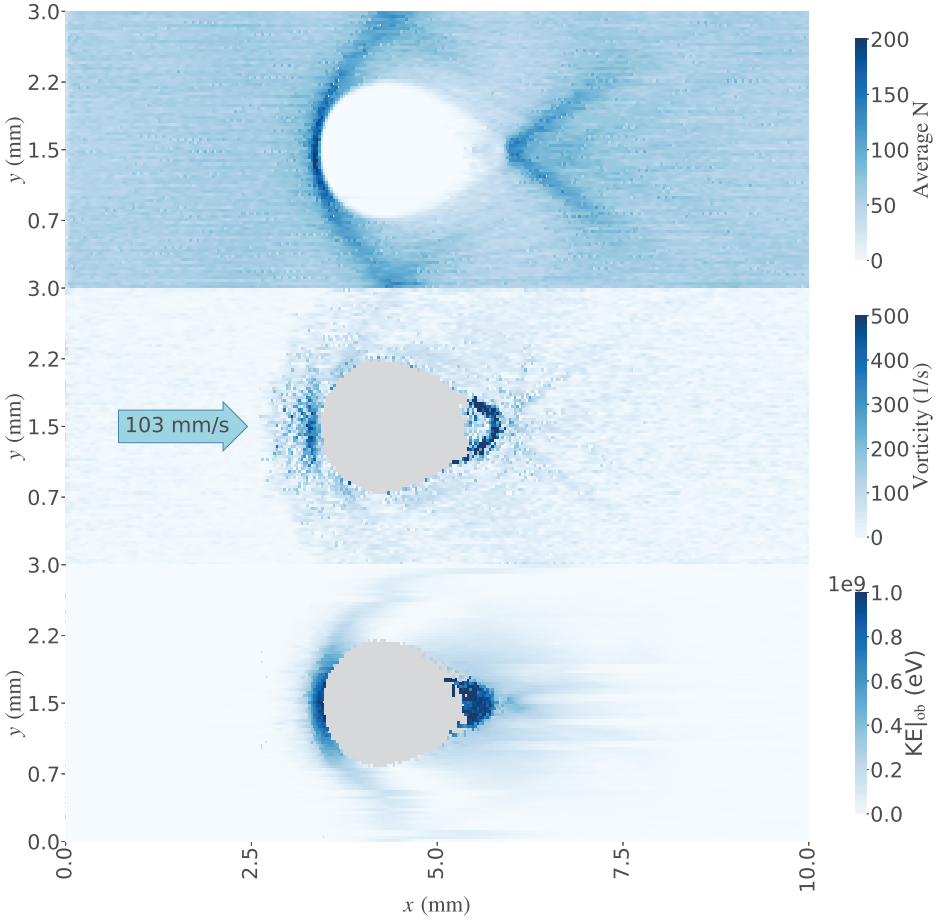

Figure 5.6: An example turbulent simulation showing (top) number of particles, (middle) vorticity, and (bottom) kinetic energy (in the frame where the obstacle is moving) averaged in bins of size $0.03 \times 0.03 \times 0.2$ mm^3. The bulk flow speed and direction are indicated on the plot. Empty pixels coloured in grey to mark the obstacle and the void around it. Vortices can be seen in the fore-wake region in front of the bow shock, and in the wake region near the Mach cones, correlating with areas of high kinetic energy.

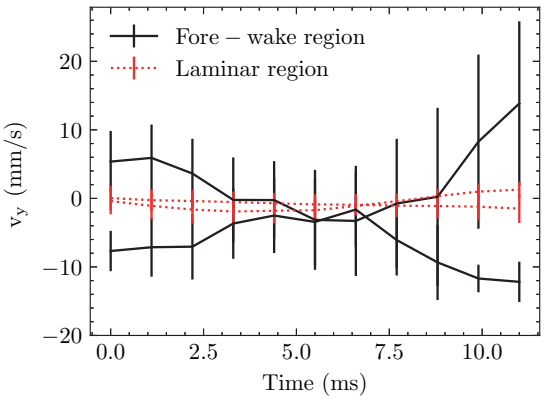

Figure 5.7: Plot of the mean and standard error of the flow velocity v_y of two sets of five randomly chosen particles within the laminar (red dotted line) and fore-wake (solid black line) region. In the laminar region, particles have a regular and ordered flow with almost no fluid mixing. On the other hand, the fore-wake region shows chaotic flow with increased mixing and intermittency.

Chaotic fluid mixing

There is increased mixing of the fluid in turbulent flow, compared to almost none in laminar flow. Two time series of the particle velocities perpendicular to the bulk flow direction averaged over five random particles are given in Fig. 5.7. The flow in the laminar region is shown by the red dotted line. The standard error of the particle velocities in the laminar region is very low, and the average velocity consistently stays very close to zero. This implies that the flow is smooth, ordered, and predictable. The particles flow in parallel sheets with very little mixing between the layers, as is exemplary of laminar flow.

On the other hand, the motion of the particles in the fore-wake region is not so smooth, as shown by the solid black line. The standard error of the velocities is very high, implying that different particles have very different velocity vectors and the flow is disordered. The average velocity undergoes abrupt changes in a short time characteristic of intermittency in fully developed turbulence [112, 116]. The flow is, therefore, chaotic, and satisfies Condition 2. The high amplitude of the velocity vectors in the direction perpendicular to the bulk flow velocity also implies increased mixing of the fluid, thus satisfying Condition 3.

Increased drag

Turbulence creates drag. This means that for the same external driving force, a laminar flow of particles will be accelerated a lot more than a turbulent flow. As the driving force increases, the increase in particle velocity increases the frictional force too, thus reducing the net acceleration of the microparticles. An external driving force is applied to the particles uniformly over the simulation box. This force drives the flow of particles along the x-axis. The resulting kinetic energy distribution of the particles is shown in Fig. 5.8. The figure plots the normalised kinetic energy, $(\mathrm{ke} - \mu_{\mathrm{ke}})/\sigma_{\mathrm{ke}}$, of the particles averaged over 1 s in bins of size $0.03 \times 0.03 \times 0.2$ mm^3. Here, μ_{ke} and σ_{ke} are the global mean and standard deviation of the particle kinetic energy at a given time. The kinetic energy in the laminar region is approximately the same as the global mean, however, it is much smaller in the fore-wake region. The driving force applied in both regions is equivalent, and yet the driven kinetic energy is higher in the laminar region than in the fore-wake region. This indicates an increased flow resistance in the fore-wake region, satisfying Condition 4 of the hallmarks of turbulence.

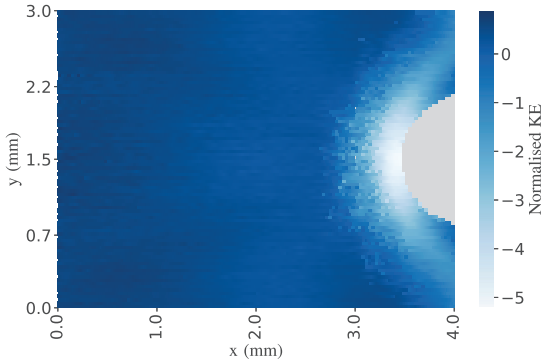

Figure 5.8: Normalised kinetic energy averaged over 1 s. The external driving force is applied uniformly throughout the simulation box. The drop in kinetic energy values in the fore-wake region compared to the laminar region indicates increased drag and increased flow resistance in the fore-wake.

Energy cascade

The most well-known feature of turbulence is the energy cascade. As shown in Fig. 5.6, the regions with vortices are the only regions with non-zero values of kinetic energy in the rest-frame of the flow. As new vortices generate and decay over time, they carry kinetic energy with them from larger scales to smaller scales. This is the characteristic energy cascade of turbulence.

To calculate the power spectra of this energy cascade, I followed the procedure as described in Section 2.6.2. I performed a Reynolds decomposition of the particle velocities. This works by decomposing the velocity $\mathbf{v}$ into a Reynolds-averaged part $\overline{\mathbf{v}}$ and a fluctuating part $\mathbf{v}'$ such that $\mathbf{v} = \overline{\mathbf{v}} + \mathbf{v}'$, $\overline{\mathbf{v}} = \langle \mathbf{v} \rangle$, and $\langle \mathbf{v} \rangle' = 0$. I then calculated the turbulent kinetic energy using $\mathbf{v}'$ and used the Wiener-Khintchine theorem to calculate the power spectra. The one-dimensional power spectra of energy cascade along x, y, and z are given in Fig. 5.9. All three power spectra show a power law dependence of $E(k) \propto k^n$ with $n = -5/3$, which is characteristic of turbulent flow. This also shows that the system is isotropic and turbulent in three dimensions. The power spectra in 3D space and time are given in Fig. 5.10. They too show an $n = -5/3$ power law. This satisfies Condition 5 by showing that the turbulent kinetic energy cascade in time and space follows the power law according to Kolmogorov's theory.

The Kolmogorov power law is valid for frequencies from $\mathrm{f} \sim 110$ Hz to $\mathrm{f} \sim 660$ Hz, and from spatial scales of roughly $200\ \mu$m to 1.26 mm. These values are consistent with the estimated Kolmogorov microscales [116, 125]. The Kolmogorov dissipation length is $\eta \sim 228\ \mu$m, and the Kolmogorov dissipation time $1/\tau_n \sim 80$ Hz. They are an estimate for the theoretical minimum length and frequency scale for which the power spectra follow the power law. They were calculated using the local viscosity, ν, and the mean rate of kinetic energy transfer, ε. The local viscosity was estimated using the average interparticle distance as the mean-free path. A numerical value of ε was determined using $\frac{1}{2}\frac{\partial \langle \mathrm{v}^2 \rangle}{\partial t}$.

For turbulence in damped systems, it is also important to determine whether the rate of energy transfer between scales is higher than the rate at which vortices are damped out. If the vortices die out faster than they can transfer energy from larger to smaller scales, then turbulence can never develop in principle [111]. For the power spectra plots in space, Figures 5.10 and 5.9 clearly show that the rate of energy cascade, $\omega_{cas} = k\sqrt{2kE(k)}$, is greater than the rate of damping, $\gamma_{Ep} = 36$ Hz, given by the Epstein damping coefficient. The cascade rate is higher than the damping rate $\omega_{cas} \geq \gamma_{Ep}$ up to $k = 5\ \mathrm{mm}^{-1}$, corresponding to distances smaller than 1.26 mm. This thereby shows that the system is in the regime where it is physically possible for turbulence to develop, as vortices transfer energy from larger to smaller scales until the length of the vortices reaches the Kolmogorov length scale.

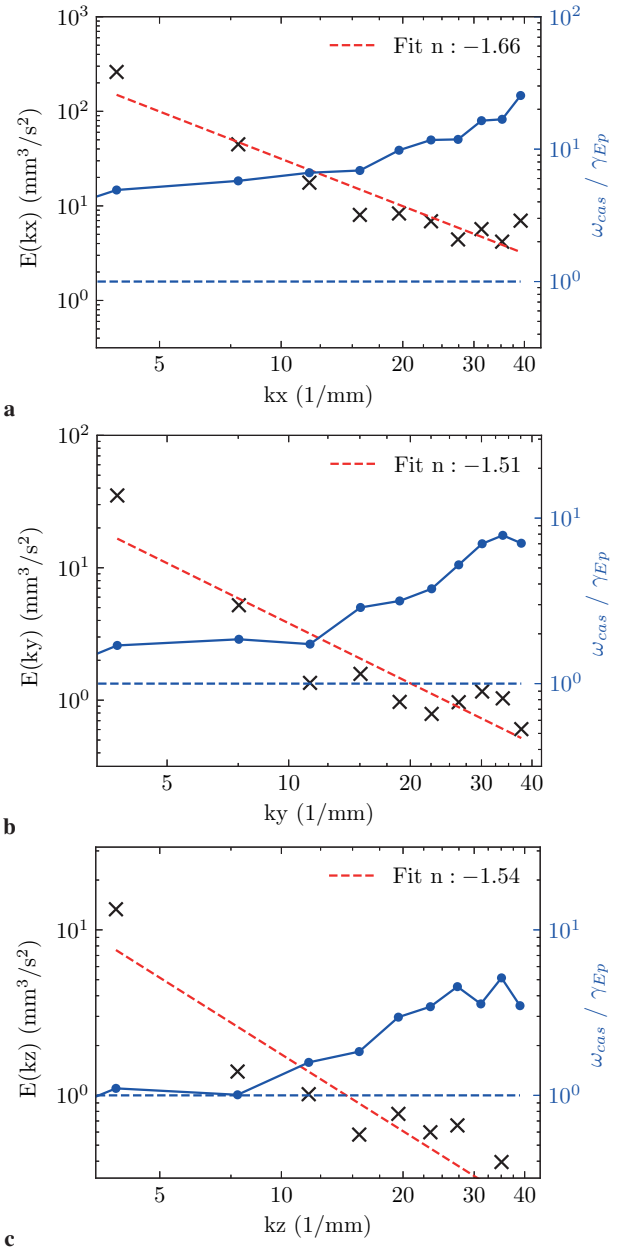

Figure 5.9: One-dimensional power spectra along the **a**) x-axis, **b**) y-axis, and **c**) z-axis. All three show a power law similar to $n = -5/3$ and are in the regime where the cascade rate is higher than damping rate.

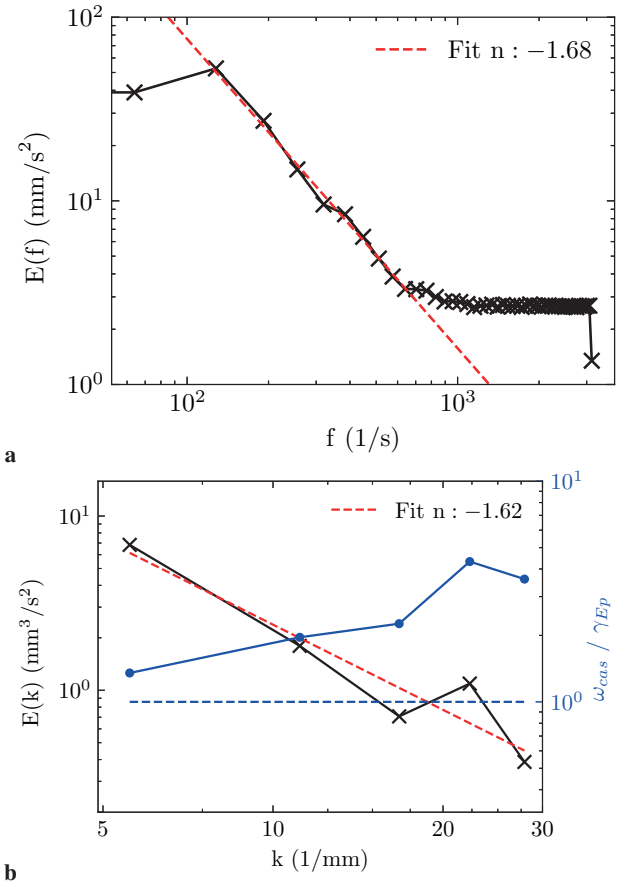

Figure 5.10: Power spectra plots in **a**) time and **b**) space corresponding to the simulation in Fig. 5.6. Both subplots show the $n = -5/3$ power law characteristic of turbulent flows. The cascade rate is higher than the damping rate indicating the system is in a regime where it is feasible to study turbulence.

v_{flow} (mm/s)	Z_d	C_s^{Th} (mm/s)	C_s^{N} (mm/s)	$\mathcal{M}$	ν_{GK} (mm^2/s)	$\Re_{GK}$	Normalised n
26.17	2000	42.54	30.89	0.85	1.65	22.20	0.77
52.44	2000	42.54	30.89	1.70	1.65	44.49	0.99
36.50	3481	56.12	50.30	0.73	19.11	2.67	0.51
83.90	3481	56.12	50.30	1.67	19.11	6.15	1.02
54.80	5000	67.27	78.80	0.70	24.75	3.10	0.50
117.30	5000	67.27	78.80	1.49	24.75	6.63	0.99

Table 5.1: Table showing the dependence of viscosity (ν_{GK}), speed of sound (C_s), Mach number ($\mathcal{M}$), Reynolds number ($\Re_{GK}$), and the power spectra slope on parameters like bulk flow speed and particle charge. The power spectra slope is normalised such that a value of 1.0 denotes a slope of $-5/3$.

I have now shown that the five conditions for turbulence as defined above, including an additional condition specific to damped systems, have been satisfied. I can now reasonably conclude that the system is turbulent, and can continue investigating the factors affecting the onset of the turbulence.

5.2.2 Onset of turbulence

In this section, I will discuss results from multiple simulations in the context of the onset of turbulence. I found that the main parameters to affect whether or not turbulence was triggered were the particle charge and the flow speed. Keeping one of these parameters constant and changing the other could trigger turbulence in an otherwise non-turbulent simulation. This is because both of these parameters directly affect $\mathcal{M}$ and $\Re$. The dependence of $\mathcal{M}$ and $\Re$ on the flow speed is straightforward due to their definitions. As the flow speed increases, so does $\mathcal{M}$ and $\Re$. However, the effect of changing the particle charge is less direct. The charge of the particles affects the viscosity of the fluid, and thereby affects $\Re$. The particle charge also affects the speed of sound $C_s = \sqrt{Z_d k_B T_d / m_d}$, and therefore $\mathcal{M}$. I could not determine a way to disentangle the two and only increase one of $\mathcal{M}$ or $\Re$. This prevented me from performing controlled tests of their individual impact on the onset of turbulence in these simulations.

The effect of changing these parameters is presented in Table 5.1. The table shows how viscosity, $\mathcal{M}$, $\Re$, speed of sound, and the power spectra slope change depending on the flow speed and particle charge. I use the Green-Kubo relation (as described in Section 3.3.4) instead of the local viscosity in this case as it is an equilibrium method of viscosity calculation and here I am interested in finding the effect of changing just the particle charge on the fluid viscosity and $\Re$. The corresponding Reynolds number calculated using this viscosity, ν_{GK}, is thus labelled $\Re_{GK}$.

For supersonic simulations, the Mach number and the speed of sound are both calculated numerically using the position of the Mach cone as outlined in Section 5.1. For subsonic simulations, the value of the numerically determined speed of sound from the supersonic simulations, C_s^{N}, was used to determine the Mach number, since the speed of sound in the system is independent of the particle bulk flow velocity. The theoretically determined speed of sound C_s^{Th} is calculated using $C_s^{Th} = \sqrt{Z_d k_B T_d / m_d}$. The numerical and theoretical values of the speed of sound are comparable, but not the same. This is unsurprising. The definition given above is not a very close approximation and often disagrees with experimental observations, albeit can be used as a good estimate.

A few trends can be noticed in Table 5.1. As the particle charge, Z_d, is increased, the speed of sound also increases. This is straightforward and predictable, as by its definition $C_s \propto Z_d^{1/2}$. This directly leads to a negative correlation between the Mach number and the particle charge, $\mathcal{M} \propto Z_d^{-1/2}$, as for a flow speed of roughly $53\ \mathrm{mm/s}$, simply increasing Z_d from 2000 to 5000 decreases $\mathcal{M}$ from 1.70 to 0.70 with all other parameters held constant. On the other hand, the reason for the positive correlation between Z_d and viscosity is less simple. The viscosity of a fluid measures the shear

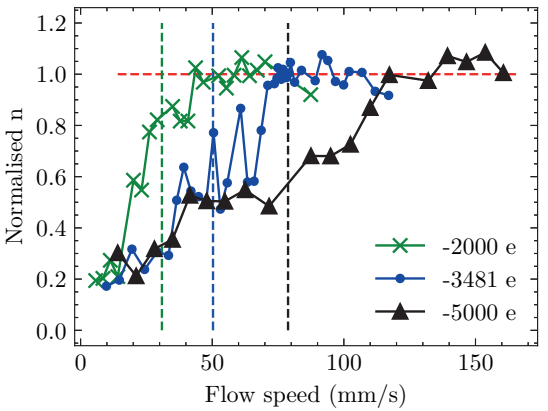

Figure 5.11: Dependence of the power spectra slope on the bulk flow speed and the particle charge. Increasing charge decreases $\mathcal{M}$ and $\Re$. Increasing flow speed increases $\mathcal{M}$ and $\Re$. Turbulence is observed in these damped simulations only in the presence of shocks. If $\Re$ is too low when $\mathcal{M} \geq 1$, the flow speed needs to be increased further until $\Re$ is high enough for turbulence to develop.

stress or internal friction between the molecules of the fluid itself. With all else constant, if the particles have a higher charge then they will exert a stronger interparticle force - thereby creating a greater shear stress force and higher viscosity. Particles with a lower charge will have weaker interparticle interactions, and hence weaker shear stress leading to lower viscosity. This positive correlation between ν and Z_d leads to a negative correlation between Z_d and $\Re$. It can be seen in the table that simulations with higher charges have consistently lower Reynolds numbers. Increasing the particle charge, therefore, decreases both $\mathcal{M}$ and $\Re$, whereas increasing the bulk flow speed increases both $\mathcal{M}$ and $\Re$. This is an important observation to take note of in order to understand the onset of turbulence.

The dependence of the power spectra slope (normalised by $-5/3$) on the bulk flow speed and the particle charge is also interesting. For a given flow speed, turbulence could be triggered by decreasing the particle charge. As an example, for a flow speed of roughly $53\ \mathrm{mm/s}$ in Table 5.1, the power spectra slope changes from 0.50 to 0.99 when the particle charge is decreased from 5000 to 2000, with all else constant. This also decreases the speed of sound such that the flow is now supersonic and can form shock fronts. Similarly, for a given particle charge, turbulence could be triggered by increasing the flow speed past the point of shock front formation.

As previously established, shock fronts were essential for the onset of turbulence in my simulations with damping. In these simulations, no turbulence was observed without the presence of shock fronts. Turbulence was observed in the fore-wake region when particles flowed directly into the bow shock, and in the wake region when particles deflected from the obstacle flowed into the Mach cone. The presence of both bow shocks and Mach cones was significant for the onset of turbulence, and this can be seen in Fig. 5.11. The figure plots the dependence of the normalised power spectra slope on the bulk flow speed for three different particle charges with all else constant. The speed of sound is marked by the vertical dashed lines, coloured according to the respective particle charge. A few important points should be noted here. Firstly, for all cases, the normalised slope reaches a value of unity if and only if the flow is supersonic. Secondly, once the slope reaches a value of unity, it flattens and stops increasing with increasing flow speed. For each value of particle charge, the flow speed was increased as much as possible until the simulations became unstable and lost particles due to high particle accelerations. Finally, the gradient of the plot decreases with increasing particle charge.

The reason why the gradient of the plot is negatively correlated with particle charge is not clear. A possible explanation is that this mimics the negative correlation between particle charge and both $\mathcal{M}$ and $\Re$. Higher flow velocities are needed to create a supersonic flow, and so the plots get flatter.

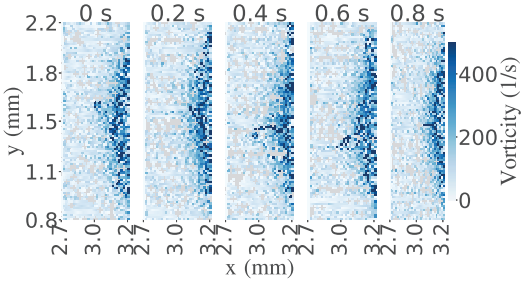

Figure 5.12: Vorticity heatmap showing intermittent switching between laminar and turbulent regions as transient turbulent puffs form and decay over space and time. This process is led by individual particle trajectories moving in a vortex and getting damped out before an energy cascade can take place.

However, how quickly the flow becomes turbulent after becoming supersonic is determined by $\Re$. For a particle charge of -2000 e, $\Re \sim O(10)$ which is high enough for turbulence to develop. Thus, as soon as the flow becomes supersonic with $\mathcal{M} > 1$, turbulence is triggered. On the other hand, for a particle charge of -5000 e, $\Re \sim O(1)$ which is too low for turbulence. In this case, when the flow becomes supersonic, it cannot become turbulent. The flow speed increases until $\Re$ is high enough to allow for the onset of turbulence. The figure thus clearly shows that in this system turbulence can reliably be triggered by either changing the flow speed or particle charge such that the flow is supersonic with low viscosity.

For supersonic flow velocities during the transition to turbulence, intermittent switching between laminar and turbulent regions was also observed. This is shown in Fig. 5.12. The flow in the fore-wake region was observed to switch from laminar to turbulent and back to laminar as transient turbulent puffs were created over time. This is characteristic of intermittent turbulence which appears during the transition to turbulence [109, 207].

The necessity of shock fronts for the onset of turbulence is presumably due to the presence of damping in the simulation. To confirm this, I performed 3D simulations in a practically undamped system with supersonic flow, with a pressure corresponding to 10^{-5} Pa and repeated the same analysis steps as before.

5.2.3 Turbulence without damping

For low-pressure simulations, I doubled the simulation box along the x-axis to 20 mm in order to give the disturbances enough time to die out before encountering the obstacle again as I expect a larger travel distance for the vortices at lower pressures. In order to keep the number density and the average interparticle distance consistent, I also doubled the number of particles to 48450 with a charge of -3481 e. I generated the obstacle with the same charge at $(x, y, z) = (2, 1.5, 2.0)$ mm. The pressure was reduced to 10^{-5} Pa, and all other parameters were kept constant.

At a pressure this low, the particle motion is practically undamped. This can be confirmed by comparing the Epstein damping rate to the rate of energy redistribution in the system given by the Einstein frequency. At a pressure of 10^{-5} Pa, the damping rate is $\gamma_{Ep} = 3 \times 10^{-5}$ Hz, whereas the Einstein frequency is $\Omega_E = 320$ Hz. In complex plasmas, the Einstein frequency is at most one to two order of magnitude larger than the Epstein frequency [86, 87], however in this case, it is larger by seven orders of magnitude. This shows that the system is undamped. The driving force was therefore switched off for the duration of data collection so the particles could continue moving at a constant flow speed. I observed turbulence in these simulations for both supersonic and subsonic flow velocities. For supersonic flow, turbulence was triggered near the presence of shock fronts, similar to the damped simulations. However, in contrast to the damped case, turbulence was also triggered in the wake-region for subsonic flow velocities. In this section, I will discuss an example of an undamped simulation with a subsonic bulk flow velocity of 30 mm/s to showcase that the flow was indeed turbulent, consistent with the working definition.

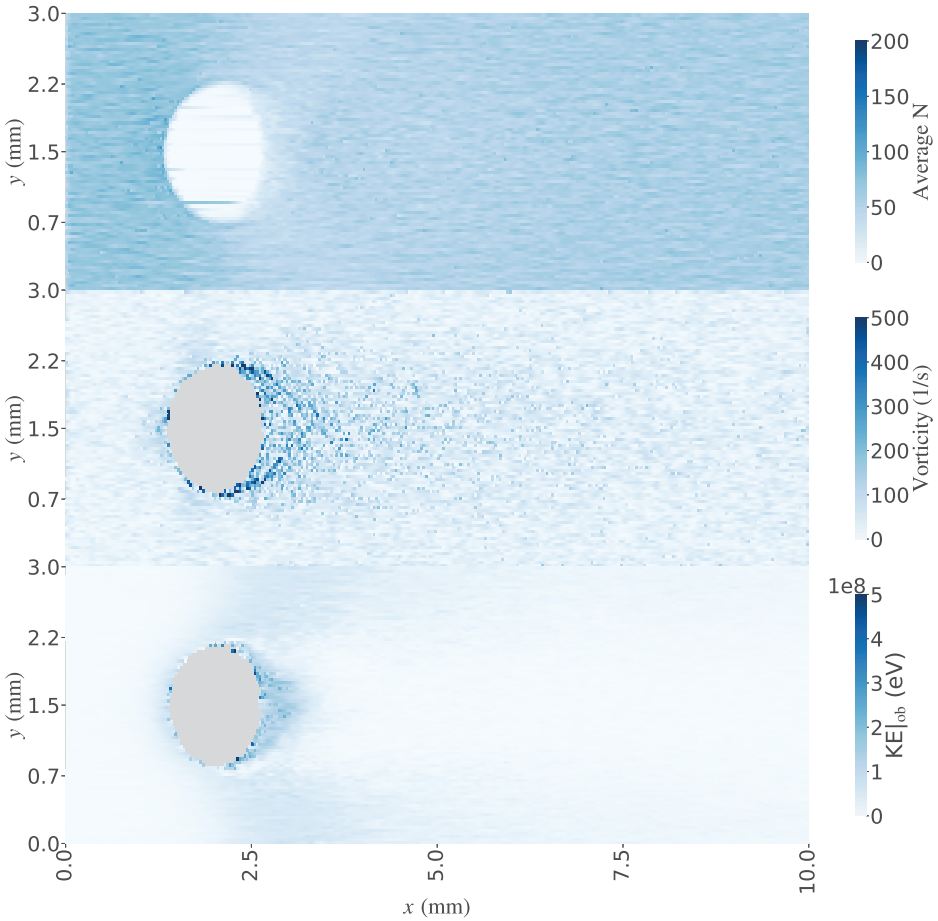

Figure 5.13: An example turbulent simulation showing (top) number of particles, (middle) z vorticity component, and (bottom) kinetic energy in the frame where the obstacle is moving averaged in bins of size $0.03 \times 0.03 \times 0.2\ \mathrm{mm}^3$. Empty pixels coloured in grey to mark the obstacle and the void around it. Turbulence is observed in the wake without the presence of shocks in this undamped simulation. This implies that the shocks are necessary in the damped simulations for the onset of turbulence since the increased microparticle density and strength of interactions are necessary for generating a cascade rate higher than the damping rate.

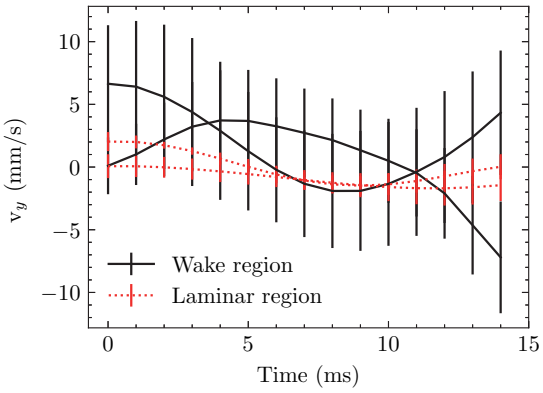

Figure 5.14: Plot of the mean and standard error of the flow velocity v_y (perpendicular to the bulk flow direction) of two sets of five randomly chosen particles within the laminar (red dotted line) and wake (black solid line) region during 0.1 s in simulation time for a practically undamped simulation at 10^{-5} Pa. The results are qualitatively similar to the simulation with damping.

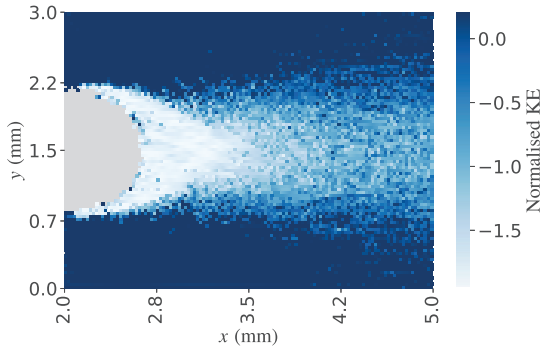

Figure 5.15: Normalised kinetic energy averaged over 1 s. The drop in kinetic energy values in the wake region indicates increased drag and increased flow resistance in the wake. The regions with a reduced energy correlate with the regions of high vorticity, suggesting that the turbulent vortices are the cause of the increased flow resistance and thus drop in energy.

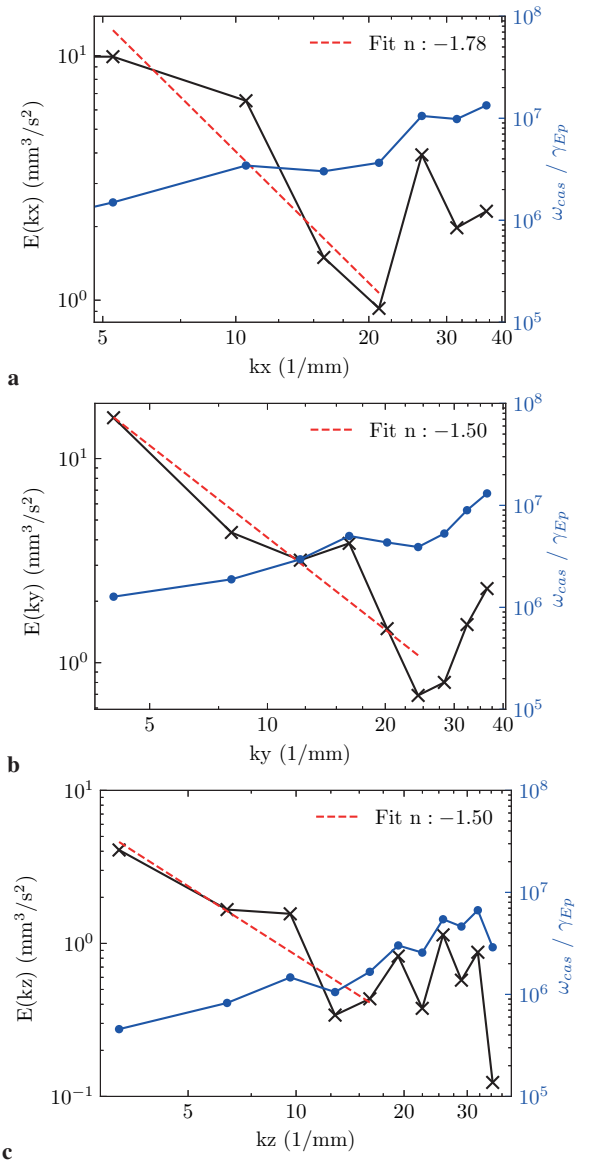

Figure 5.16: One-dimensional power spectra along **a**) x, **b**) y, and and **c**) z for a low pressure simulation at 10^{-5} Pa. The power spectra show a power law of $n = -5/3$, and the cascade rate is higher than the damping rate in all cases by many orders of magnitude.

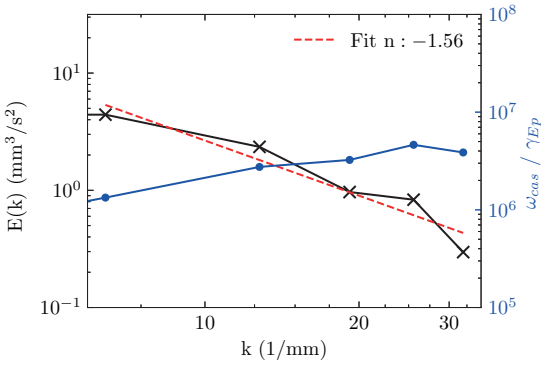

Figure 5.17: Power spectra plots in 3D space for a low pressure simulation showing the $n = -5/3$ power law characteristic of turbulent flows. The cascade rate is many orders of magnitude higher than the damping rate, implying that the regime is suitable to study turbulence in.

The results from the simulation are shown in Fig. 5.13. The plots of number density (top), z vorticity component (middle), and kinetic energy (bottom) clearly show the presence of vortices in the wake-region of the obstacle without the presence of shock fronts. The kinetic energy plot shows the average kinetic energy value in the rest frame of the flow. This plot correlates with the vorticity plot, implying that vortices are the carriers of kinetic energy excitations due to turbulence.

This satisfies Condition 1 of the signatures of turbulence. Additionally, these plots look similar to turbulence in conventional fluids such as air or water. This is unsurprising, as such systems are usually undamped.

The turbulent region was defined similar to the damped case, from $2.5-3.5$ mm in x, $0.8-2.2$ mm in y, and $0.8-2.2$ mm in z, corresponding the the wake region of the obstacle. The flow perpendicular to the bulk flow direction in both regions is shown in Fig. 5.14. The figure plots the flow velocity v_y in two sets of five randomly chosen particles in the given region. Similar to the damped fluid, the flow in the laminar region is smooth and ordered with the mean velocity close to zero and low standard error. The flow in the turbulent region is chaotic with high standard error implying disordered velocity vectors, along with an increased amplitude of the mean velocity implying an increased rate of fluid mixing. This satisfies Conditions 2 and 3 for turbulence.

The flow in the turbulent region also shows an increased flow resistance in the wake of the obstacle. This can be seen in Fig. 5.15, where the kinetic energy due to the driving force is lower in the turbulent region. This satisfies Condition 4.

The power spectra for the undamped simulations are similar to the ones with damping. The one dimension spectra can be seen in Fig. 5.16 to have a power law similar to n = $-5/3$, thereby demonstrating that the turbulence is three dimensional and isotropic in this system. This satisfies Condition 5 for the evidence of turbulence. The power law is followed from spatial scales of roughly 1.3 mm to 200 μm, which is consistent with the Kolmogorov microscale $\eta = 250$ μm.

All the hallmarks of turbulence as described previously are shown to be satisfied for an undamped simulation of complex plasma flow past an obstacle. Turbulence was clearly observed in the wake of the obstacle without the presence of any shock fronts. This is directly in contrast with the damped simulations where no turbulence was observed without shock fronts. This emphasises the importance of shock fronts for the onset and development of turbulence in the damped system in these simulations.

5.3 Summary of results

In order to investigate the formation of shocks and the onset of turbulence, I simulated a 3D flow of microparticles past a spherical obstacle in a complex plasma. I found that simulations with supersonic flows produced Mach cones and bow shocks, which often displayed a multi-part structure in the form of multiple Mach cones with different opening angles, bow shocks with multiple fronts, as well as secondary bow shocks that are 'reflected' and smaller versions of the primary bow shock. Bow shocks with multiple fronts (*double* bow shocks) appeared in the transition regime during the formation of a main bow shock. The two shock fronts appeared first and then collapsed into a single bow shock as the speed was increased. To the best of my knowledge, this is the first time double bow shocks have been reported in complex plasmas. They have previously been observed in astrophysical plasmas, but have yet to be seen in complex plasma experiments. Besides this, the observation of shock fronts was noteworthy for two other reasons. Firstly, Mach cones can be used to determine the speed of sound in the system by measuring their opening angle. Secondly, the development of shock fronts in the damped simulations led to the onset of turbulence.

I found that the formation of shocks in the simulations with damping was essential to the onset of turbulence. This work is one of the first systematic particle-resolved investigations of turbulence. In it, I study turbulence in a variety of conditions such as in subsonic, supersonic, damped, and undamped systems. In the simulations with damping, I observed turbulence in the regions where there was a direct flow of particles into a shock front. As shock fronts are regions of high compression and increased microparticle density, the strength of interparticle interactions is much stronger too. Thus, a flow of particles directly into a shock front can generate vortices strong enough to overcome damping and start an energy cascade, thereby triggering the onset of turbulence.

As turbulence has no exact definition, I compared the simulation results against a list of common hallmarks of turbulence. I checked that the flow was rotational, chaotic, diffusive, resistive, and self-similar, and thus concluded that the flow was indeed turbulent according to the working definition used in this thesis.

Once I had established that these simulations were turbulent, I investigated how to reliably trigger the onset of turbulence. I was able to do this by changing two main parameters. The first was the bulk flow speed, and the second was the particle charge. Increasing the bulk flow speed increased both the Mach number, $\mathcal{M}$, and the Reynolds number, $\Re$. On the other hand, increasing the particle charge decreased both $\mathcal{M}$ and $\Re$. I then showed that the necessity of shock fronts for the onset of turbulence in these simulations was due to the presence of damping in the system. By reducing the gas pressure to the point where the fluid was practically undamped, I was able to recreate turbulence in the simulations without the presence of shock fronts. This demonstrated that shock fronts were necessary only because the fluid was damped. The strength of damping given by the gas pressure along with the particle charge and the bulk flow speed are parameters that can be reproduced and controlled in complex plasma experiments. By changing one of these parameters, turbulence could be triggered in the simulations in a reproducible manner. These simulations can, therefore, help predict and control the onset of turbulence in experiments. This work can thus inform future experimental investigations of turbulence at the level of individual particles using complex plasmas, as well as open up new avenues for research and simulation-based studies of turbulence.

Chapter 6

Formation of string-like clusters

"It doesn't matter how beautiful your theory is, it doesn't matter how smart you are. If it doesn't agree with experiment, it's wrong."

Richard P. Feynman

The formation of microparticle string-like clusters (SLCs) is emblematic of electrorheological (ER) effects in complex plasmas [44]. The application of an external electric field induces the buildup of positive wake charges directly behind the particle downstream from the ion flow. At short interparticle distances of the order of the distance between the wake and the particle, the interparticle potential is of course attractive. Often, it is assumed that this is true at long-range as well, similarly to conventional ER fluids. Here, the range of the interparticle interactions is defined with respect to the size of the dipole as the characteristic length, which in this system would be the size of the ion shielding cloud in the direction of the electric field. In the simulations, this length is modelled as the distance between the microparticle and the positive ion wake[1]. An interaction is considered *long-range* if it occurs at interparticle distances much larger than this characteristic length.

If the assumption of long-range attraction between microparticles was correct, then a characteristic interparticle distance would emerge in the microparticle suspension in the direction parallel to the electric field corresponding to the position of the potential well minimum. On the other hand, this characteristic distance would not appear in the microparticle suspension in the direction perpendicular to the electric field as the interparticle distance only depends on the balance between repulsive and confinement forces along that direction. Recently, experiments in the PK-4 laboratory have shown that the interparticle distances both parallel and perpendicular to the external electric field are comparable [47, 48]. If the distance between the particles within an SLC is similar to the inter-string distance, then the need for an attractive interparticle potential well for SLC formation is called into question.

In the following work, I use a new MD simulation method by Schwabe et al. [60] to simulate the formation of SLCs **without long-range attraction**. In conjunction with the experiments performed by my colleagues, I showed for the first time that SLC formation can occur with a repulsive interparticle potential, thereby demonstrating that long-range attraction is not a necessity. Simply reducing the repulsion along the direction of the electric field was enough to produce strings aligned in that direction. The results of this study are published in [208].

This was achieved by using `LAMMPS` to perform 3D MD simulations of negatively charged microparticles with two positive wakes to mimic the effect of alternating ion flow in experiments. I

[1] The interparticle distances in this system of strongly charged microparticles would never get small enough to be of the same order as the wake distance, unlike conventional ER fluids.

demonstrate that SLCs can be produced in simulations with long-range reduced repulsion similarly to experimental observations, and report that simulations with long-range attraction became unstable as the microparticles experienced an acceleration strong enough to escape the simulation box. I compare the results from the experiment conducted on the PK-4 facility on board the ISS [70] with the results from the 3D MD simulation, and report an excellent qualitative agreement between them.

6.1 Experiment on the ISS

6.1.1 Setup and procedure

The experiment was performed in the PK-4 facility on board the ISS by cosmonaut A. Ivanishin as instructed by Pustylnik et al. from the ground. The experimental setup is detailed in Section 3.5.2.

The following experimental procedure similar to [209–211] was used. For this experiment, a DC glow discharge was used with argon as the working gas at a pressure of $11\ \mathrm{Pa}$. MF particles with a diameter of $3.38\ \mu\mathrm{m}$ were injected into the chamber. They were transported into the working area by a DC discharge of $0.5\ \mathrm{mA}$ current. The discharge regime was then changed to polarity-switching to trap the microparticles. The polarity of the active electrode was switched with a frequency of $500\ \mathrm{Hz}$, which provided the ion flow for producing SLCs in the experiment. This frequency is too high for the microparticles to react to, and so they experience the time-averaged zero electric field. Not only does this polarity switching trap the microparticles, but it also creates an ion drift relative to them since the ions are fast enough to follow the periodic variations of the electric field, leading to wake formation on either side of the particles.

Once the microparticle suspension was in equilibrium showing clear SLCs, a 3D scan of the structure of the suspension was performed. Afterwards, the gas discharge was switched off for a given duration of time completely destroying any order or structure in the system. A fraction of a second later the discharge was switched on again, leading to the formation of SLCs once more. Once the microparticles had relaxed back into an equilibrium state, another 3D scan was performed. This experimental procedure was only possible in microgravity conditions since on the ground the particles would fall under the influence of gravity during the plasma-off time.

6.1.2 Observations and techniques

A video camera with a field of view of $1600 \times 600\ \mathrm{pixels}$ and a frame rate of $60\ \mathrm{FPS}$ was used to record images of the microparticles during the experiment. The particles were illuminated in a quasi-2D plane by a laser sheet. When possible, a 3D scan was performed to observe the 3D structure of the microparticle suspension with a range of $14\ \mathrm{mm}$ at a velocity of $0.9\ \mathrm{mm/s}$. During the part of the experiment where the camera was static only 2D information is available. The particle data such as position and velocity could be retrieved directly from the 2D images, whereas the algorithm used to determine the 3D positions of the particles from the scanning is described in [47].

The microparticle suspension displayed a string-like structure in the experiment, as seen previously [47, 48]. This is shown in Fig. 6.1, where the suspension is **a** in a disordered state and **b** crystallised into SLCs.

6.2 Molecular dynamics simulations

The simulation was initialised at thermodynamic equilibrium as a Yukawa fluid with 3430 point-like particles of charge $q = -3481\ \mathrm{e}$ in a simulation box with periodic boundary conditions of size $4.5 \times 3 \times 3\ \mathrm{mm}^3$. The microparticles had a mass of $3 \times 10^{-14}\ \mathrm{kg}$ consistent with a particle diameter and density of $3.38\ \mu\mathrm{m}$ and $1510\ \mathrm{kg/m}^3$ respectively. The timestep for the simulations was set to $10\ \mu\mathrm{s}$

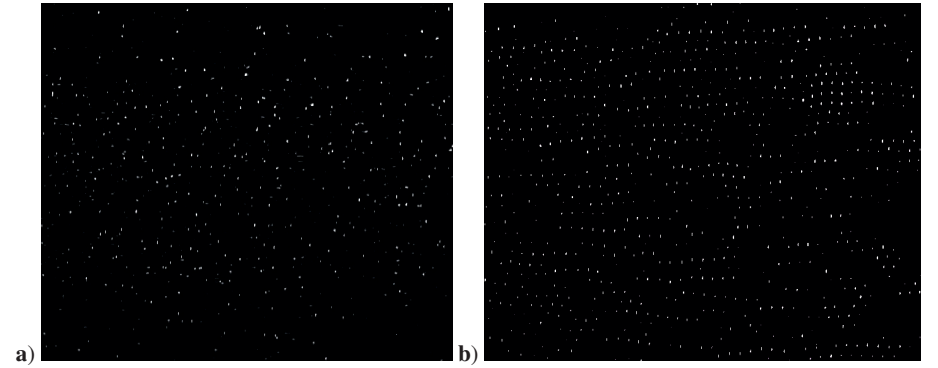

Figure 6.1: Images from the experiment showing **a**) disordered particles with no discernible structure, and **b**) particles crystallised into SLCs. The contrast of the image has been artificially enhanced for visual clarity. Modified from [212].

with a data acquisition rate of $1000\ \mathrm{FPS}$. Periodic boundary conditions were used in all directions to mimic the effects of a net-zero ambipolar electric field. Assuming periodic boundary conditions implies that the plasma density is so low that the microparticle cloud is radially stable only if the ambipolar electric field vanishes as the ionsation balance localises, as previous plasma simulations suggest [213–215]. The forces acting on the particles other than the interparticle force are just those from the Langevin dynamics thermostat and the friction with the background gas determined by the Epstein damping coefficient corresponding to argon gas at a pressure of $11\ \mathrm{Pa}$.

At the start of the simulation, a Yukawa interparticle potential was used with a Debye length of $\lambda_D = 190\ \mu\mathrm{m}$ and a cutoff distance of $7\ \lambda_D$ for the potential. The Yukawa interparticle potential was used only during the initialisation of the simulation until the microparticle ensemble reached thermodynamic equilibrium at $1200\ \mathrm{K}$ and an average interparticle distance of $227\ \mu\mathrm{m}$. Once the particles reached thermodynamic equilibrium, the interparticle potential was modified by placing a positive ion wake charge on either side of the microparticle along the x-axis. The details of how the potential was modified are given in the next section.

6.2.1 Modified interparticle potential

One characteristic of MD simulations is that they only simulate the dynamics of microparticles without simulating the dynamics of electrons and ions in the plasma. The impact of the ion flow is mimicked by the modification of the microparticle interaction potential. In the past, MD simulations of ER complex plasmas have mimicked the effect of a directional ion flow by incorporating a positive wake charge on one side of the particles [59, 133, 216]. These simulations build on this approach by modifying the Yukawa interparticle potential by placing two ion wakes of charge $-w_\mathrm{c}\ q$ around the particle $\pm r_\mathrm{w}\ \mu\mathrm{m}$ away (one on each side) along the x-axis [60] of the simulation box as shown in Fig. 6.2. This mimics the effect of alternating ion flow due to an alternating electric field with a duty cycle of 50%. The code for the modified potential is made available via GitHub at [146].

The modified interparticle potential has the form

$$\phi = \phi_\mathrm{Y} + \phi_{\mathrm{w}+} + \phi_{\mathrm{w}-}, \tag{6.1}$$

with

$$\phi_\mathrm{Y} = \frac{q}{4\pi\epsilon_0 r}\exp(-\kappa r) \tag{6.2}$$

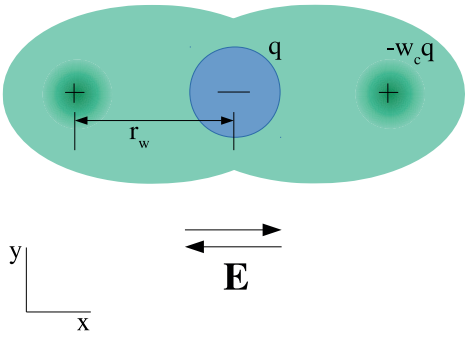

Figure 6.2: Sketch (not to scale) defining the simulation parameters used to model the deformation of the ion cloud from the AC electric field. The electric field, **E**, is applied along the x-axis of the simulation box, which dictates the direction of SLC formation. For a microparticle with charge q, a positive wake charge $-w_c\, q$ is positioned $\pm r_w\ \mu$m away to mimic the deformation of the ion cloud.

and

$$\phi_{\mathrm{w}\pm} = \frac{-w_{\mathrm{c}} q}{4\pi\epsilon_0 |\mathbf{r} \mp \mathbf{r}_{\mathrm{w}}|} \exp(-\kappa_{\mathrm{eff}} |\mathbf{r} \mp \mathbf{r}_{\mathrm{w}}|), \tag{6.3}$$

where

$$\kappa_{\mathrm{eff}} = \sqrt{\frac{\kappa^2}{(1 + \mathcal{M}_{\mathrm{th}}^2 \cos^2\zeta)} + \kappa_{\mathrm{e}}^2}. \tag{6.4}$$

Here, $\mathcal{M}_{\mathrm{th}}$ is the ion thermal Mach number, $\zeta = \pi$ rad is the angle between the ion flow and the vector connecting the microparticles, $\kappa = 1/\lambda_D$ is the interparticle screening parameter, and κ_{e} is the electron screening parameter. An effective screening parameter is required here instead of κ as the screening of the electric field due to the wakes is affected by the ion flow. It depends on the direction and speed of the ion flow, hence its dependence on $\mathcal{M}_{\mathrm{th}}$ and ζ. As the bulk of the plasma contains subthermal ions, we used $\mathcal{M}_{\mathrm{th}} = 0.7$, which is higher than the critical value found for SLC formation [21, 217]. The wake charge[2], w_{c}, and wake distance, r_{w}, can be thought of as the main free parameters that can be changed to modify the interparticle potential in order to produce SLCs.

An example of how this modifies the potential is given in Fig. 6.3, which plots the axial profiles of the original Yukawa and the effective interparticle potential. The black dashed line signifies the Yukawa potential, whereas the solid red line signifies the combined interparticle potential ϕ. The inset given on the top right of the figure shows very clearly that the combined potential is no longer attractive after $x \approx 75\ \mu$m. The inset not only shows that the combined effective interparticle potential is repulsive at long-range, but also shows that it is *less* repulsive when compared to the Yukawa potential.

The two main parameters that can affect the interparticle potential are the wake charge, w_c, and the wake distance, r_w. To understand how they do so, consider the potential experienced by a test particle inside a string due to its nearest neighbours on either side. This potential is shown in Fig. 6.4, for an interparticle distance of 200 μm, and wakes of charge $-0.2\ q$ placed $\pm 55\ \mu$m away from each microparticle. The test microparticle and the potential experienced by it is coloured red, whereas the nearest neighbours fixed in their positions at $x = \pm 200\ \mu$m are coloured blue. The test particle in a string is located at the bottom of a local minimum. The depth of this locally-minimum potential well depends on factors such as the average interparticle distance, wake charge, and wake distance. In this

[2]Please note that the 'wake charge' w_{c} is a dimensionless number representing the charge of the wake as a fraction of the microparticle charge.

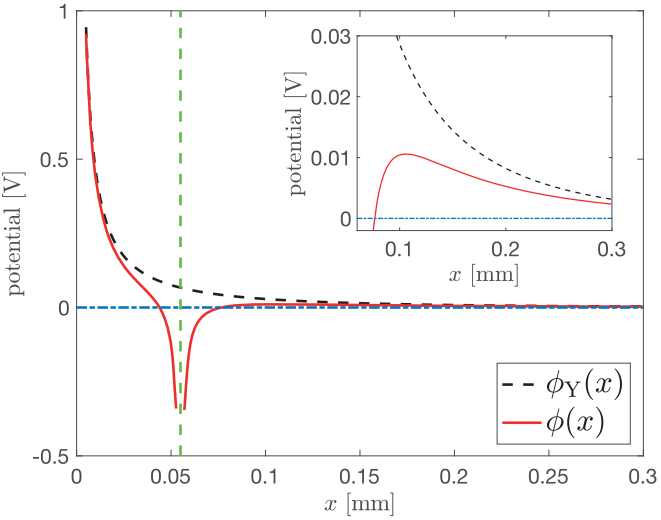

Figure 6.3: Axial profiles of the Yukawa potential ϕ_Y (black dashed line) and the modified potential ϕ (solid red line) along the direction of wake formation. A positive wake charge with $w_c = 0.2$ is placed at $x = 0.055$ mm, marked by a vertical dashed line. The inset on the top right is an enlarged version of the figure showing the long-range tail of both potentials. It shows that the modified potential is less repulsive than the Yukawa potential at distances larger much larger than r_w, and not attractive. From [208]

example, the depth of the well is ~ 10 eV, which is 200 times larger than the average particle kinetic energy at equilibrium of ~ 0.05 eV.

Changing the wake distance moves the positive wake charges along the x-axis, thereby moving the location of the asymptotes and changing the width and depth of the local potential well. Similarly, changing the wake charge would change the gradient of the asymptote. A higher charge would produce a flatter or wider asymptote and thereby result in a narrower but deeper local potential well. The higher the wake charge and the further away it is from the microparticle, the more the repulsion is reduced compared to the Yukawa potential. Keeping the wake distance constant, increasing the wake charge would continue to deepen this potential minimum until the interparticle potential is attractive at long-range. In the simulations, this resulted in particles being accelerated so strongly that the simulations became 'unstable' as the particles often escaped the simulation box. This is consistent with previous MD simulations [59, 60]. Furthermore, the time taken for SLC formation was highly sensitive to changes in r_w and w_c.

In order to determine how strong the SLC formation was in the simulations, the 'stringiness' of the system is used as an order parameter. This, in essence, is a measure of how many nearest neighbours of a particle are a part of an SLC. This can be determined by counting how many particles lie within the width of the peak in the pair correlation function. The various pair correlation functions are discussed in detail in Section 6.4. If a particle is not in an SLC, this value is zero. If a particle is at the edge of an SLC, it will have only one nearest neighbour. If a particle is in the middle of an SLC, it will have two nearest neighbours and no more. The spatially-averaged value of this number at a given time is the *stringiness* of the system. The stringiness of the system is therefore a dimensionless number between zero and two.

The stringiness at equilibrium can be used in order to estimate the minimum deviation needed from the Yukawa potential for SLC formation. Fig. 6.5 plots how the equilibrium stringiness depends

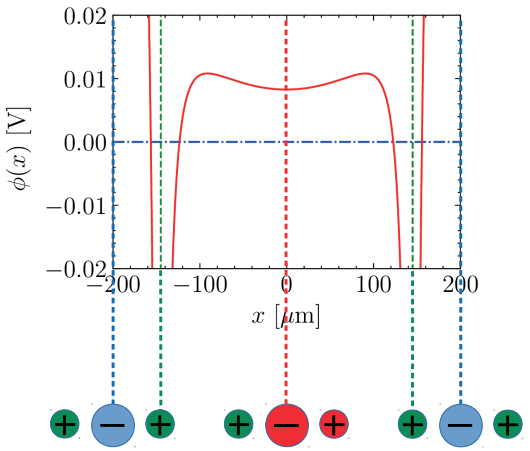

Figure 6.4: Axial profile of the interparticle potential experienced by a microparticle in a string due to its nearest neighbours. Each negatively charged microparticle has a positive wake of charge $-0.2\ q$ on either side $\pm 55\ \mu\mathrm{m}$ away. Changing the wake charge and distance changes the depth and width of the local minimum that the test particle in the string is trapped in.

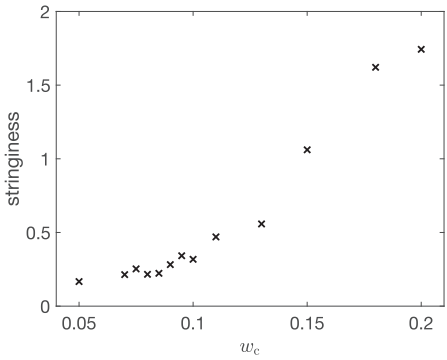

Figure 6.5: Dependence of equilibrium stringiness on wake charge with all other parameters constant. Changing the wake charge changes the depth and width of the potential well. The threshold in wake charge needed to form a significant number of strings is around $w_c \sim 0.15$. I use a value of $w_c = 0.2$ for the simulations due to its high stringiness value, implying the formation of strong and stable strings. From [208].

on the wake charge when all other parameters are kept constant, with $r_w = 55\ \mu\mathrm{m}$. It shows that for small wake charges, the stringiness is very low and increases slowly. As the wake charge increases and reaches around $w_\mathrm{c} \sim 0.15$, the stringiness rises rapidly. As the deviation from the Yukawa potential increases, the value of stringiness increases. For this work, I chose a value of $w_\mathrm{c} = 0.2$ with $r_w = 55\ \mu\mathrm{m}$ since it produced strong and stable SLCs consistently. Higher values of wake charge caused the interparticle potential to become attractive at long-range and led to numerical instabilities, such as high particle accelerations that led to lost atoms.

6.3 Recrystallisation

6.3.1 In the experiment

One of the aims of the experiment was to destroy the structure of the microparticle suspension and then watch how it reformed, in a process known as *recrystallisation*. To achieve this, the plasma discharge was switched off for a fraction of a second, which was long enough to destroy any structure in the system as the particles decharged and heated up. This technique of switching the plasma off has been used previously in an experiment by Nosenko et al. [152] when they intended to determine the spatial profile of a manipulation laser beam *in situ*. This was only possible to do after upgrading the PK-4 hardware with the '*Experimental Interface*', gaining ability to perform experiments without any residual gas flow.

Once the plasma was switched off, the particles were seen to quickly decharge and heat up. The particles decharge due to surface recombination of charges as well as the decaying plasma density. On the other hand, the reasons for the particle heating are unclear. The particles continued to stay suspended due to microgravity for much longer than the plasma was switched off for in this particular experiment. They also experienced a slow residual drift, which was presumably a thermophoretic effect. This 'plasma-off' procedure was repeated multiple times for the same microparticle suspension at the same discharge conditions. The plasma was switched off for varying lengths of time without a major difference in results. For the purposes of this study, it was sufficient to switch the plasma off for long enough to completely destroy the SLC structure. As such, my colleagues and I decided to concentrate on an example with the plasma-off time of $0.3\ \mathrm{s}$. This is much shorter than the timescale of a few seconds required to reform the structure.

6.3.2 In the simulations

As specified earlier, for the simulations, I used the modified interparticle interaction potential given in Equation 6.1 with $w_\mathrm{c} = 0.2$ and $r_\mathrm{w} = 55\mu\mathrm{m}$. The data used in the following analysis can be found in [212], and the `LAMMPS` input file I wrote for the simulation is given in Appendix B. The arrangement of the microparticles during the recrystallisation process is visualised in Fig. 6.6.

Once the simulation was at thermal equilibrium at $1200\ \mathrm{K}$ and the interparticle potential was changed to the modified potential, the crystallisation was initialised by reducing the microparticle temperature down to $300\ \mathrm{K}$. The microparticles crystallised into SLCs, as seen in Fig. 6.6**a**, which is very similar to what was observed in the experiments in Fig. 6.1**b**. Upon reaching equilibrium, the structure in the system was destroyed completely (as seen in Figs. 6.6**b** and **c**) by mimicking the 'plasma-off' conditions from the experiment: Firstly, I reduced the particle charge dramatically, as particles were experimentally observed to decharge when no longer located in a plasma. And secondly, I increased particle temperature back to $1200\ \mathrm{K}$, as particles were observed to heat up during this time. I set the microparticle charge during the 'plasma-off' stage to be $-10\ \mathrm{e}$ instead of zero as it is common for particles to have a residual charge in the afterglow [218, 219]. However, there was no noticeable difference in the results of this study between simulations with zero residual charge and $-10\ \mathrm{e}$ during the plasma-off stage. Due to the particle decharging, a temperature of $1200\ \mathrm{K}$ was

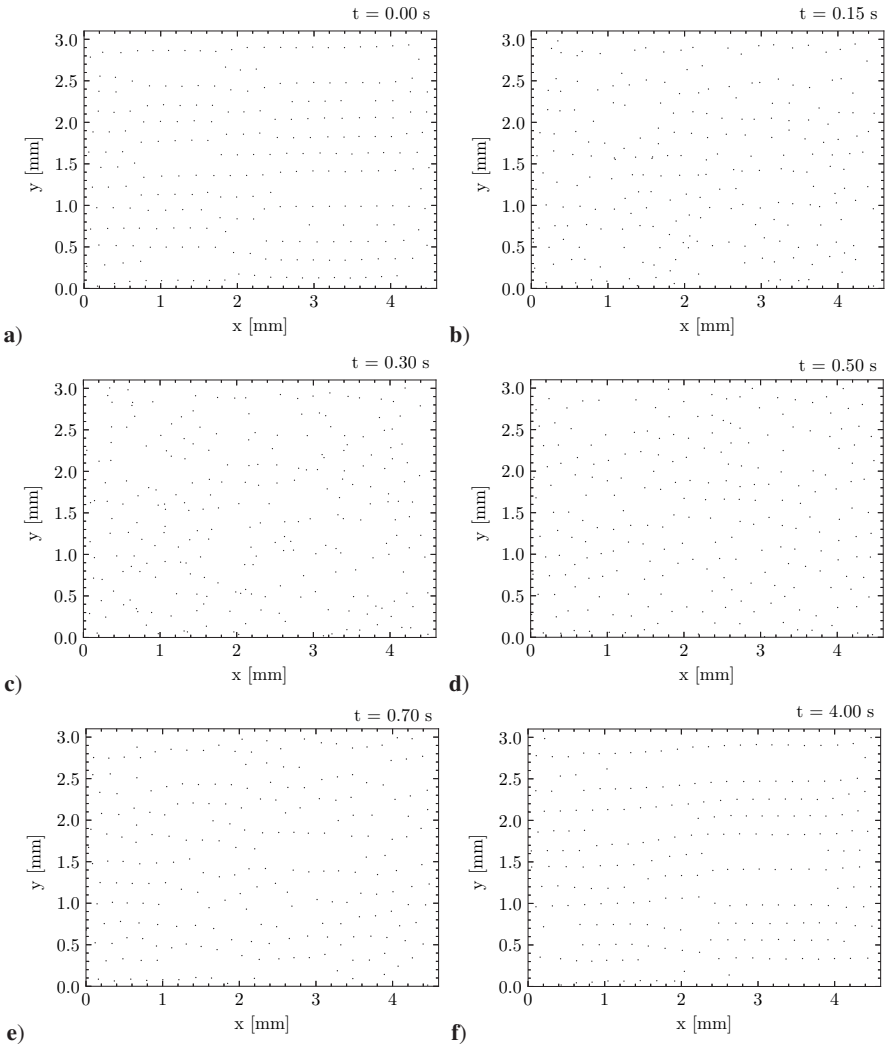

Figure 6.6: Visualisation of the simulated microparticles in a 2D slice from $1.0 - 1.2$ mm in z during the recrystallisation process. The figure shows **a**) the equilibrium state of the particles at the instance of time when the plasma was turned off at $t = 0.00$ s, **b**) the system during the plasma-off phase, **c**) the system immediately before the plasma was turned on again at $t = 0.30$ s, **d**) the disordered system after plasma was turned on, **e**) the system as the particles recrystallise into strings, and **f**) the equilibrium state of the particles.

enough to destroy the SLC structure in the simulations. After a duration of 0.30 s, these changes were reverted in order to mimic the plasma being turned on again. The state of the system after this at $t = 0.50$ s is shown in Fig. 6.6**d**, which is still disordered. The particles slowly recrystallised into SLCs as shown in Fig. 6.6**e**, and returned to an equilibrium state, i.e. the stringiness of the system stabilised at a constant value. The new equilibrium reached by the system is shown in Fig. 6.6**f**, which looks nearly identical to the previous equilibrium in Fig. 6.6**a**.

The structural change to the microparticle suspension during recrystallisation can be determined by tracking how the radial distribution function (RDF) changes. The RDF, as discussed earlier in Section 3.3.3, displays the probability of finding a particle at a given radial distance away from a reference microparticle. The changes to the RDF during the recrystallisation process in the simulation are shown in Fig. 6.7, calculated with a resolution of $\delta r = 0.1\ \lambda_D$. The RDF at equilibrium before the plasma has been turned off, shown in Fig. 6.7**a**, displays an unusual structure. The large initial peak in the RDF - signifying the average interparticle distance - is split into a smaller secondary peak at a lower value of r and a larger primary peak at a higher value of r. The secondary peak corresponds to the interparticle distance within a string, and the primary peak corresponds to the inter-string distance in the simulation. The primary peak is positioned at approximately $r = 0.26$ mm with an amplitude of $g(r) = 3.28$. The secondary peak, on the other hand, is positioned at approximately $r = 0.21$ mm with an amplitude of $g(r) = 1.46$. The difference in distance between the two peaks, $\Delta r = 50\ \mu$m corresponds to the wake distance, $r_w = 55\ \mu$m. The position of both the secondary and primary peaks (hence the interparticle and inter-string distances respectively) are comparable, consistent with recent experiments in the PK-4 facility [47, 48]. The peak splitting occurs due to the reduced repulsion in the direction of string formation, as the interparticle distance is slightly lower within a string compared to the inter-string distance. The ratio between the amplitude of the two peaks as well as the ratio of the first minima to the primary peak amplitude is approximately 0.45 and 0.16 respectively, which do not seem to correspond to any input parameters.

Once the plasma was turned off, this secondary peak merged back with the primary peak as shown in Fig. 6.7**b** - implying that the SLC structure was destroyed. Initially, the RDF of the microparticles resembled that of a liquid (red dashed line), but over time it changed to resembling a gas (solid black line). This is because in a liquid the particles are weakly interacting with each other whereas in a gas the particles undergo hard sphere collisions. As the microparticle structure was destroyed completely and the particles were decharged, the suspension of microparticles behaved more like a gas.

The RDF of the simulated system after the plasma was turned on again and the particles were given enough time to relax back to equilibrium ($t = 4.00$ s) is shown in Fig. 6.7**c**. This figure looks almost identical to the RDF at equilibrium before recrystallisation as shown in Fig. 6.7**a**. The secondary peak is visible once more. The location of both the primary and secondary peaks is unchanged at $r = 0.26$ mm with $g(r) = 3.09$ and $r = 0.21$ mm with $g(r) = 1.39$, respectively. The distance between the two peaks still corresponds to the wake distance, and the ratio of their amplitudes is still 0.45. The ratio of the first minima to the primary peak, however, is slightly reduced to 0.13.

After recrystallisation into SLCs, some particles got close enough to their neighbours to be trapped in the potential well created by their positive wake. As a result the particles became attached to their neighbours in agglomerate-like clusters. This can be seen in Fig. 6.7**c** as the small peak at $r = 55\ \mu$m, which corresponds to the wake distance. A hypothesis for why this happened is that during the plasma-off stage, the particles approached each other much closer than they would otherwise. As the plasma was turned on again and their charges restored, they experienced strong accelerations and had a kinetic energy high enough to escape the local minimum of the potential well and instead get trapped in the attractive potential well due to the positive wakes. This is a limitation of the simulation as I saw no way to completely eliminate this effect, though reducing the timestep seemed to mitigate it slightly.

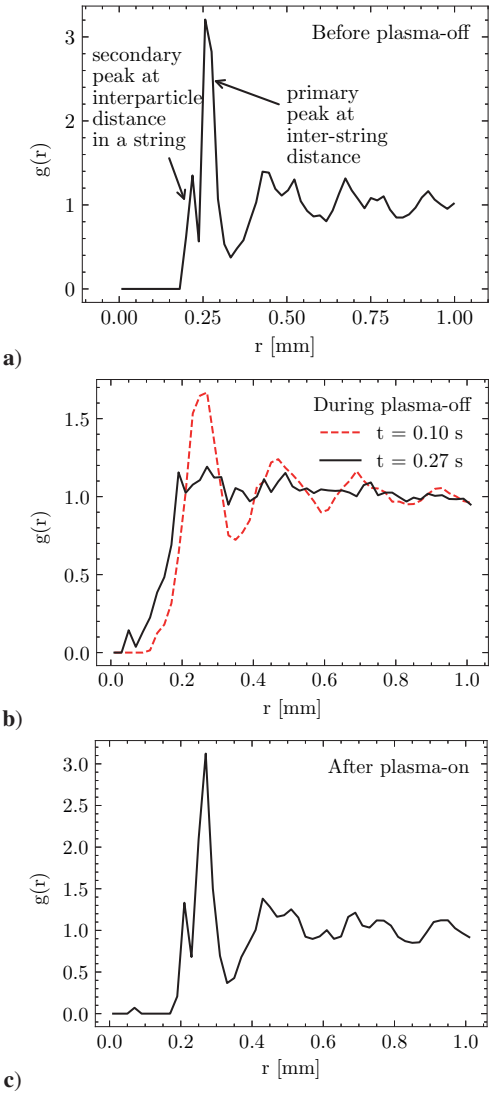

Figure 6.7: RDF of the microparticle suspension **a**) before, **b**) during, and **c**) after the plasma-off process in the simulation calculated with $\delta r = 0.1\ \lambda_D$. The structure before and after is nearly identical, with a small secondary peak (at interparticle distance in a string) accompanying the large primary peak (at inter-string distance). The secondary peak disappears during the plasma-off stage, signifying the total destruction of SLCs. During the plasma-off stage, the particle suspension at first appears similar to a liquid (red dashed line). As the particles decharge and heat up, the ensemble resembles a gaseous state instead (solid black line).

6.4 Structure and stability

To gain insight into the structure of the microparticle suspension, it is important to look at how the particles are distributed in 3D space with respect to each other. This can be done by calculating the *3D pair correlation function*. This is a three dimensional version of the RDF, calculated in spherical coordinates of r, θ and ϕ, defined as [47, 48]:

$$G(r,\theta,\phi) = \frac{1}{n_{\mathrm{d}} N} \sum_{\substack{i,j=1 \\ i \neq j}}^{N} \frac{\delta\left(r_{\mathrm{i,j}} - r\right) \delta\left(\theta_{\mathrm{i,j}} - \theta\right) \delta\left(\phi_{\mathrm{i,j}} - \phi\right)}{4\pi r^2 \cos\theta}. \tag{6.5}$$

Here, the distance between two microparticles i and j along the different coordinates is given by r_{ij}, θ_{ij} and ϕ_{ij} representing the length, polar angle and azimuthal angle respectively. The number of particles is given by N, and n_{d} is the macroscopic microparticle number density. This function measures the probability of finding particle i at a given displacement of (r_{ij}, θ_{ij}, ϕ_{ij}) away from particle j. The location of peaks in the pair correlation function thus specifies the preferential interparticle distances at which particles are more likely to be found, and indicates the presence and direction of ordering or clustering phenomena. The position of the peaks can thus provide information about the structure of SLCs and the arrangement of particles inside them.

As displaying $G(r,\theta,\phi)$ in a figure would require four dimensions to represent it, it is simpler to use its angular integrals. These are defined as:

$$G_{\phi}(r,\theta) = \int_{0}^{2\pi} G(r,\theta,\phi) d\phi \tag{6.6}$$

and

$$G_{\theta}(r,\phi) = \int_{-\frac{\pi}{2}}^{\frac{\pi}{2}} G(r,\theta,\phi) \cos\theta d\theta, \tag{6.7}$$

and allow us to qualitatively characterise the 3D order in the suspension by focusing on two dimensions at a time.

The pair correlation function was used to analyse the 3D structure of the microparticle suspension in both experiment and simulation. Simulated data is available in 3D during the entire simulation, however 3D experimental data is only available during equilibrium when the particle motion was slow enough to make 3D scans possible. This means that there is no 3D experimental data available during the recrystallisation process. As such, a 2D pair correlation function in polar coordinates along ρ and α can be used to determine the 2D structure of the microparticle suspension during recrystallisation. This is defined as:

$$g_{\mathrm{2D}}(\rho,\alpha) = \frac{1}{\sigma_{\mathrm{d}} N} \sum_{\substack{i,j=1 \\ i \neq j}}^{N} \frac{\delta\left(\rho_{\mathrm{i,j}} - \rho\right) \delta\left(\alpha_{\mathrm{i,j}} - \alpha\right)}{\rho}, \tag{6.8}$$

where the interparticle distances between particle i and j are given by $\rho_{\mathrm{i,j}}$ and $\alpha_{\mathrm{i,j}}$ representing the length and polar angle respectively. Here, N is the total number of particles in the illuminated plane, and σ_{d} is the '2D number density' of particles in the image. For this 2D analysis, the direction with $\alpha = 0$ rad is defined to be directed along the axis of the plasma chamber.

As the pair correlation functions describe the probability of finding particles a given interparticle distance away, the radial and angular widths of the peaks determine which neighbours formed an SLC together [48]. The peaks in the correlation functions indicate the preferred interparticle distances in the cluster, and so they are also referred to as '*string peaks*'. Particles lying within this preferred interparticle distance (or 'within a string peak') were identified as 'string neighbours' [47, 48]. As

specified in Section 6.2.1, the average number of string neighbours at a given time was used as a measure of the order in the system, the *stringiness*.

6.4.1 In the experiment

The 3D SLC structure at equilibrium for the experimental data is shown in Fig. 6.8 for $G_\phi(r,\theta)$ (left) and $G_\theta(r,\phi)$ (right) **a** before and **b** after recrystallisation. The equilibrium structure is practically identical in both cases before and after the recrystallisation process. Only the initial and final conditions are shown because of the lack of 3D data during recrystallisation. Both subfigures of $G_\phi(r,\theta)$ show strong string peaks directed along $\theta = \pm\pi/2$ rad, indicating that as the direction of SLC formation. The arches in this correlation plot signify the inter-string correlations. Similarly, both subfigures of $G_\theta(r,\phi)$ show equidistant peaks representing the angular distance between strings. In all subfigures, the peaks along r suggest that the interparticle distance within an SLC is $r \sim 0.2$ mm on average.

On the other hand, the evolution of the microparticle structure during recrystallisation was determined using the 2D pair correlation function, as shown in Fig. 6.9. The figure shows how the order in the system changes over time. The spatial distribution of the particles are coloured according to the number of string neighbours they have (left) and the corresponding 2D pair correlation function (right). The particles are coloured blue if they have zero string neighbours, green if they have one, and red if they have two. The correlation function for the equilibrium structure in Fig. 6.9**a** shows that SLCs are aligned along the direction of $\alpha = \pi$ rad and $\alpha = 0$ rad with an average interparticle distance of $\rho \simeq 0.2$ mm in the SLC. The inter-string correlation arches are also visible here. The plasma was switched off at $t = 0.00$ s, and turned on again at $t = 0.30$ s. The equilibrium structure is shown to be destroyed entirely in Fig. 6.9**b** after $t = 0.26$ s, before the plasma was switched on again. Here, the particles were moving like hard spheres with almost no charge and interparticle force, as reflected in the complete lack of peaks in the pair correlation function. The number of red-coloured particles (two string neighbours) is dramatically reduced as the number of blue-coloured particles (zero string neighbours) is dramatically increased. At $t = 0.50$ s, Fig. 6.9**c** shows that the particles were starting to reform some structure as the number of red (and green) particles starts increasing again. However, SLCs had not yet formed. This is also reflected in the corresponding pair correlation function, which has no peaks along α, but its peaks along ρ resemble the RDF of a fluid, similar to the simulation data in Fig. 6.7**b**. At $t = 4.00$ s, the system returned back to equilibrium as Fig. 6.9**d** is qualitatively identical to Fig. 6.9**a**. During the recrystallisation process, the equilibrium order of the particles was rapidly destroyed and took much longer to reform. The peaks in this 2D pair correlation function, $g_{2\mathrm{D}}(\rho,\alpha)$, were used to determine the stringiness of the system in order to study how it evolved during the recrystallisation process.

6.4.2 In the simulations

A 3D SLC structure was observed in the simulations similar to the experimental data, as shown in Fig. 6.10 for $G_\phi(r,\theta)$ (left) and $G_\theta(r,\phi)$ (right). The equilibrium structure before recrystallisation (at $t = -1.00$ s) is shown in Fig. 6.10**a**, showing SLCs along the direction of $\theta = \pm\pi/2$ rad with an average interparticle distance of $r \simeq 0.2$ mm within the SLCs. Inter-string correlation arches are visible in the $G_\phi(r,\theta)$, as well as the peaks corresponding to the preferred inter-string angular distance along ϕ in the $G_\theta(r,\phi)$ correlation plot. This figure shows excellent qualitative agreement with Fig. 6.8, suggesting a qualitatively identical SLC structure in both simulations and experiment. The radial and angular widths of the string peaks in this figure were used to determine the string neighbours to calculate the stringiness in the simulation.

The plasma-off condition was simulated at $t = 0.00$ s and the plasma was switched on again at $t = 0.30$ s. The 3D structure of the system during recrystallisation at $t = 0.30$ s is shown in Fig. 6.10**b**.

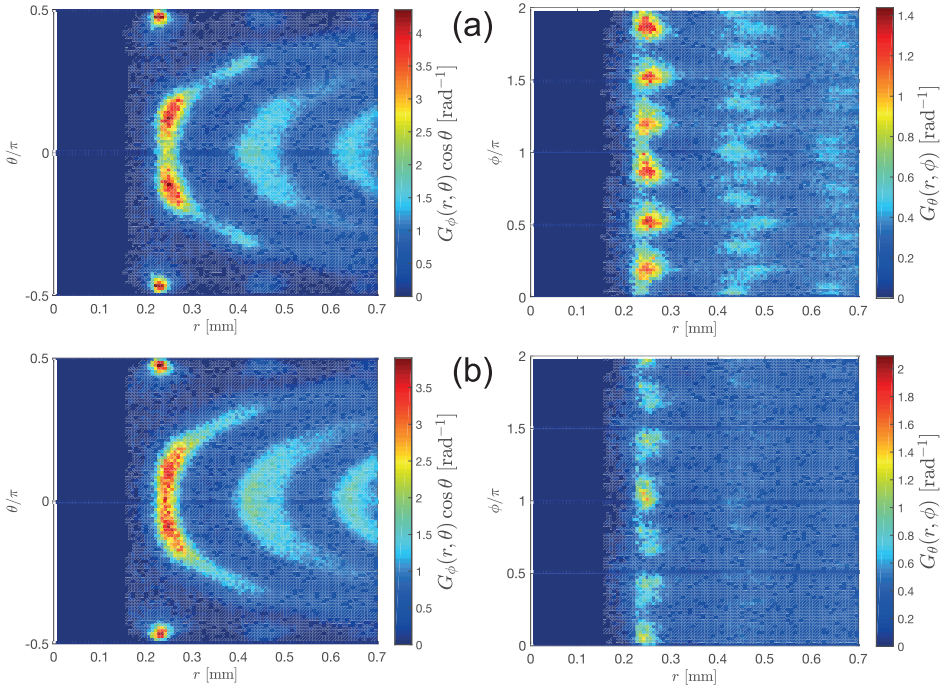

Figure 6.8: Angular integrals of the pair correlation function, $G_\phi(r,\theta)$ (left) and $G_\theta(r,\phi)$ (right) for the experimental system at equilibrium **a**) before and **b**) after recrystallisation while forming SLCs. The subfigures are nearly identical before and after recrystallisation, showing clear string peaks as well as inter-string arches. From [208].

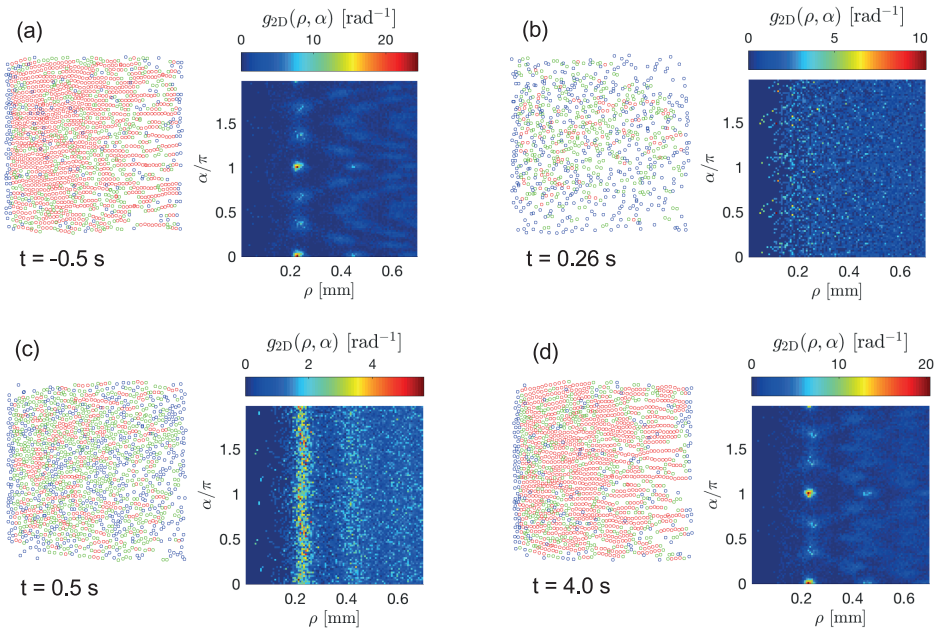

Figure 6.9: Spatial arrangement of particles (left) and the corresponding pair correlation function (right) for the 2D experimental data before, during, and after the plasma-off phase. In the spatial plots, the particle colour reflects the number of string neighbours: red for 2, green for 1, and blue for 0. The highly stringy structure in **a**) was destroyed in **b**), slowly reformed in **c**), and had fully reformed by **d**). From [208].

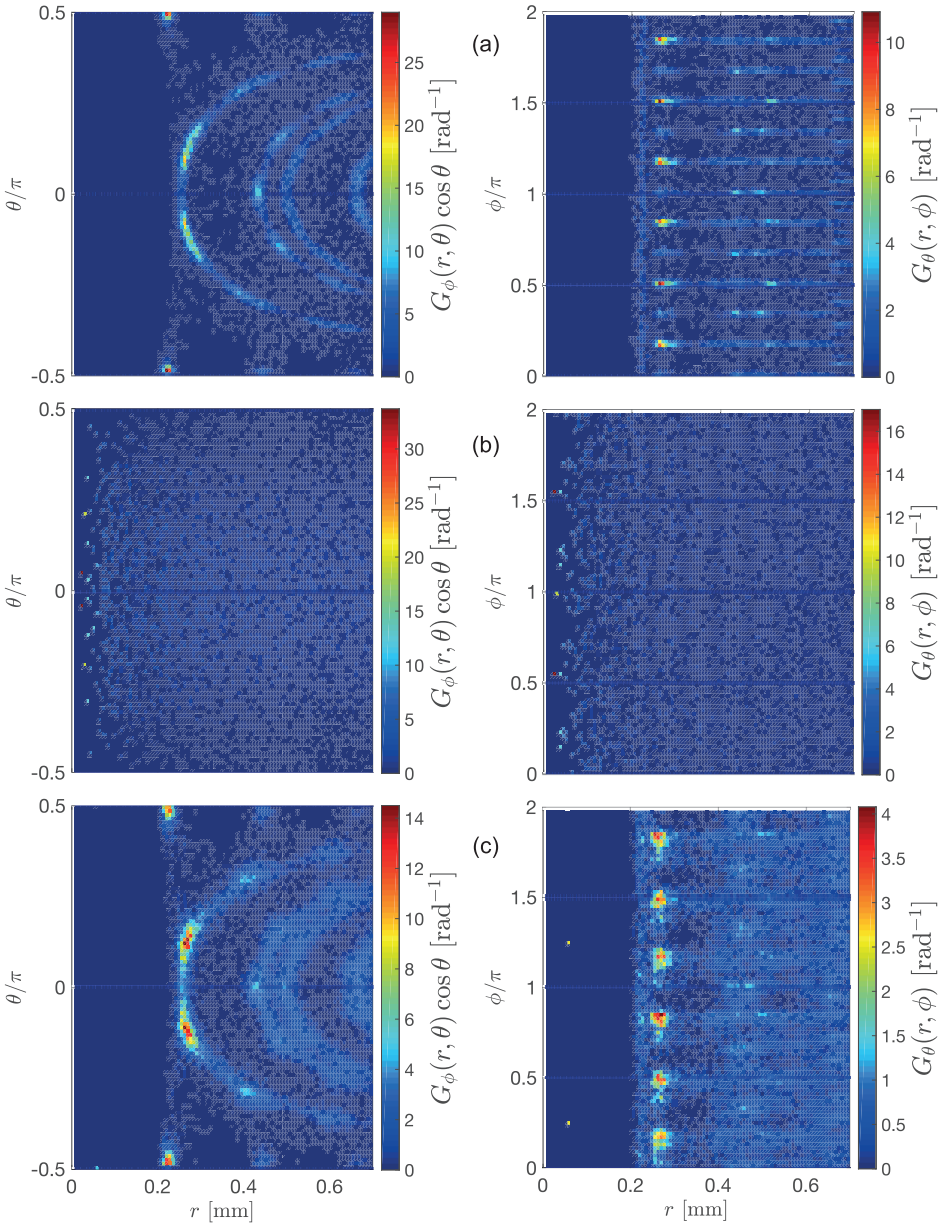

Figure 6.10: Angular integrals of the pair correlation function, $G_\phi(r,\theta)$ (left) and $G_\theta(r,\phi)$ (right) for the simulated data at **a**) equilibrium before recrystallisation at $t = -1.00$ s, **b**) after the structure was destroyed and immediately before the plasma was turned back on at $t = 0.30$ s, and **c**) after the particles relaxed back to equilibrium at $t = 5.00$ s. The SLC structure in **a**) was completely destroyed in **b**) and had fully reformed in **c**). From [208].

It can be seen very clearly that all structure and order in the system was thoroughly destroyed by the time the plasma was switched on again. Though the 3D correlations of the experiment are not available for a direct comparison, the figure is very similar to the 2D correlations in the experiment during recrystallisation. A few seconds after the plasma was turned on again, the correlation functions at $t = 5.00$ s shown in Fig. 6.10**c** look qualitatively identical to those in Fig. 6.10**a**. The SLC structure observed in simulations shows excellent qualitative agreement with the structure observed in experiments, including how the system relaxed back to an equilibrium SLC structure after complete destruction of order.

Similar to the RDF plots, a slight difference between the interparticle distance within a string and the inter-string distance can be noted in the $G_\phi(r, \theta)$ plots. For the case of effective long-range attraction, the difference would be a lot more exaggerated than it is here for both numerical and experimental data. In Fig. 6.8 as well as Fig. 6.10, the inter-string arches lie at slightly higher distances than the string peaks. This effect is more pronounced in the simulation data than experimental data as the peaks in the experimental data seem to smear due to the integration. In both cases, the slightly larger value of the inter-string distance compared to the interparticle distance within a string is indicative of a reduced repulsion along the direction of string formation.

6.4.3 Relaxation timescale

The stringiness calculated as a function of time using the correlation functions from Figs. 6.9 and 6.10 is shown in Fig. 6.11**a** over the duration of the recrystallisation process[3]. The figure shows excellent qualitative agreement between the experimental and simulated results as the evolution of the stringiness looks remarkably similar in both cases. The time interval in which the plasma was switched off is marked by vertical dashed lines. It can be seen clearly that both the simulated and experimental stringiness was constant before the plasma was switched off and decayed rapidly during the plasma-off phase. After the plasma was turned on again, the stringiness in both cases returned slowly to a constant value at equilibrium[4]. It can be observed that the original and final value of stringiness at equilibrium is different for the simulated data. This is because the order in the system was destroyed entirely. For a purely qualitative comparison, the two values do not have to be the same - it is sufficient that they are similar.

The corresponding particle velocities during recrystallisation are given in Fig. 6.11**b**. For the simulation, only the average particle velocity as a function of time is considered. However, for the experiment, the average difference between the microparticle velocity and the local drift velocity is considered for the directions perpendicular and parallel to the ion flow. The particle velocities in both simulation and experiment were constant before the plasma was turned on, rise instantaneously to a new value during the plasma-off stage, and then very quickly decayed back to the original value over a few milliseconds after the plasma was turned on again. In both cases, the velocities rose dramatically immediately after the plasma was turned back on. This instantaneous rise in velocity can be explained by considering the particle charges during this process. During the plasma-off phase, the particles had a very low residual charge. This allowed them to approach each other a lot more closely than they otherwise would. Almost as soon as the plasma is turned back on, the particles regained their charges and were strongly repelled by each other, leading to high accelerations and velocities. The peak in velocity is thus just a result of the particle charge being restored after the plasma was turned back on.

[3]This work can only provide *qualitative* agreement between experiment and simulation, and that is sufficient to show that a repulsive interparticle potential can explain experimental observations and an attractive potential is not required.

[4]The system is at 'equilibrium' if the stringiness (as the parameter used to measure order in the system) stops changing and stabilises at a constant value.

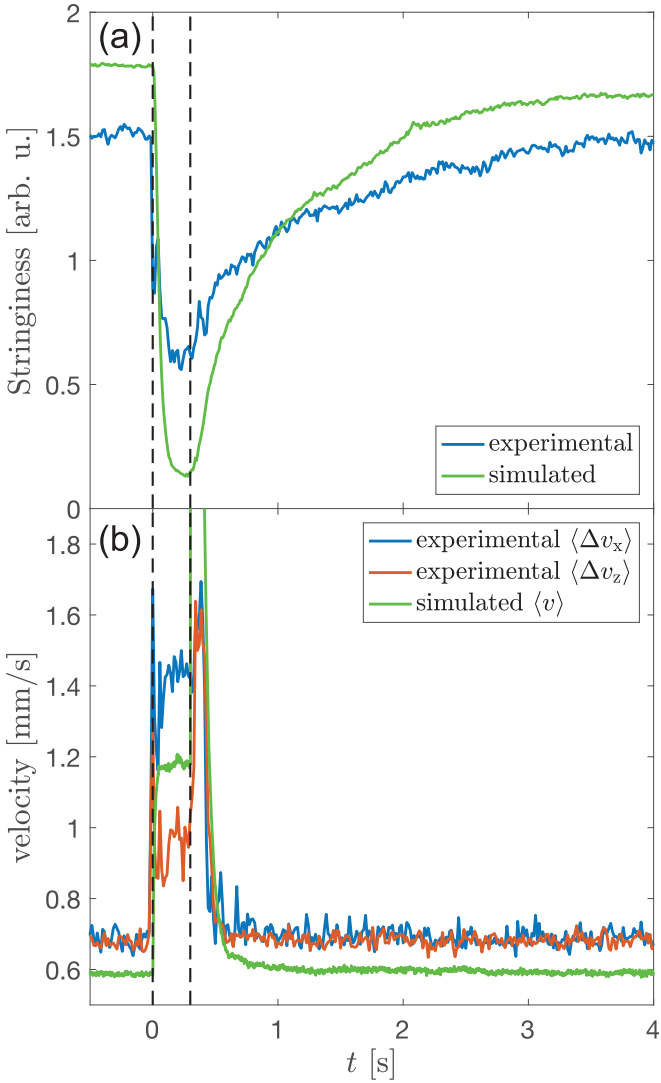

Figure 6.11: Variation of the **a**) stringiness and **b**) microparticle velocities with time during the recrystallisation process showing good qualitative agreement between experiment and simulation. For the simulation, spatially-averaged particle velocities were considered, however for the experiment, the difference between microparticle velocity and the local drift velocity was used. From [208].

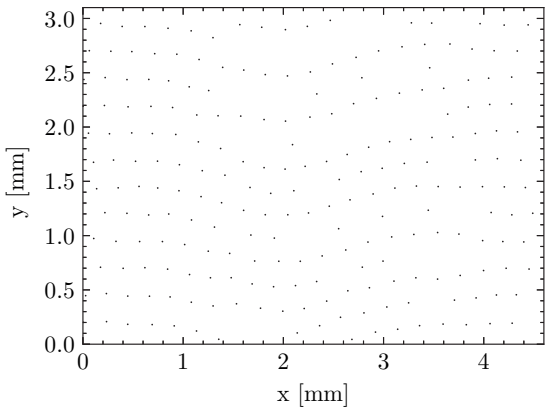

Figure 6.12: Deformation of SLCs due to a simulated laser perpendicular to the direction of ion flow applied at $x = 2$ mm visualised in a '2D' slice in $(1.0 - 1.2)$ mm in z. The laser had a Gaussian profile with a standard deviation of 0.5 mm and applied a force of 3×10^{-14} N to the particles for a duration of 0.5 s.

Particle Diffusion

There is an interesting thing to note in Fig. 6.11. The relaxation time needed for the stringiness to return to equilibrium is many orders of magnitude longer than the time needed to destroy the SLC structure for both experiment and simulation. Furthermore, the time needed for the velocities to return to a constant value is much shorter than the relaxation time for stringiness. Changes in stringiness happen on a much longer timescale than changes to particle velocity, which implies that the mechanism for SLC formation does not entirely depend on particle temperature. Once the microparticles have already cooled back down, the rising value of stringiness implies that they continue diffusing towards their equilibrium positions in the SLCs. This can be checked by comparing a theoretical estimate for the diffusion time of the particles with the observed recrystallisation time.

Assuming a weak coupling coefficient, the diffusion coefficient is given by $D = lv_T/3$, where l is the microparticle mean free path and v_T is the microparticle thermal velocity. The mean free path is defined to be $l = (\sigma n_\mathrm{d})^{-1}$, with n_d being the microparticle number density and σ the cross sectional area. For very low particle velocities after cooling, the cross-section σ is independent of particle velocity and depends only on the geometry of the ion cloud. The shielding cloud of ions is not spherical, but ellipsoidal in shape as represented in Fig. 6.2. The semi-axes of the Debye 'ellipsoid' are given by λ_D in the direction perpendicular to the ion flow, and $\lambda_D + r_w$ parallel to it. The cross-sectional area can then be estimated by averaging the area of the three projections of the ellipsoid:

$$\sigma = \frac{1}{3}\left[\pi\lambda_\mathrm{D}^2 + 2\pi\lambda_\mathrm{D}\left(\lambda_\mathrm{D} + r_\mathrm{w}\right)\right]. \tag{6.9}$$

Using this expression and the parameters used in the simulation, the mean free path is evaluated to be $l = 87$ μm and the diffusion coefficient can thereby be estimated to be $D = 1.6 \times 10^{-8}$ m^2/s, consistent with (the lower end of) previous estimates of diffusion coefficients in complex plasmas [220, 221]. Finally, by defining the relaxation time to be the time needed for a particle to diffuse by an average interparticle distance of $\Delta \approx 200$ μm, we can estimate the time to be $t_\mathrm{diff} \sim \Delta^2/D \approx 2.5$ s, consistent with both simulation and experiment. As a comparison, using the average interparticle distance as the mean free path, $l \sim \Delta \sim 200$ μm, results in a diffusion coefficient of $D = 3.7 \times 10^{-8}$ m^2/s. It results in a relaxation time of $t_\mathrm{diff} \approx 1.1$ s which is much faster than experimental and numerical observations. This implies that the geometry of the ion wakes plays a significant role in the process of particle diffusion towards an equilibrium SLC structure.

6.4.4 Deformation

Another method to test the stability of an SLC structure is to deform it slightly. An external laser can be applied perpendicular to the direction of SLC formation with enough force to deform the structure without immediately breaking it. I simulated SLCs with the modified interparticle potential using $w_c = 0.2$ and $r_w = 55\ \mu\mathrm{m}$ for 3430 particles in neon gas at $60\ \mathrm{Pa}$ and $1000\ \mathrm{K}$, with mass consistent with a particle diameter of $3.4\ \mu\mathrm{m}$. To this system, I applied a laser of force of $F_{\mathrm{ext}} = 3 \times 10^{-14}$ N directed along the $-y$-axis for a duration of 0.5 s. A Gaussian laser-profile was used centered at $x = 2\ \mathrm{mm}$ with a standard deviation of $0.5\ \mathrm{mm}$, and produced a 'U-shaped' deformation in the structure as seen in Fig. 6.12. Once this external laser was switched off, the SLC structure took $t \simeq 1.5$ s to return back to its equilibrium shape.

As yet, there are no experimental results to compare with this simulation data for the relaxation time after deformation. Though, similar parabolic flight experiments using the PK-4 setup have been performed recently by Kretschmer et al. [222]. In principle, testing the stability of an SLC structure observed in experiments by measuring the minimum force needed to break it, as well as recording the relaxation time needed for the microparticles to return to equilibrium, might be one way to calibrate the simulation parameters in order to aim for a quantitative agreement.

6.5 Summary of results

Complex plasmas have been observed to exhibit electrorheological (ER) properties by the formation of string-like clusters (SLCs) in microgravity conditions. In conventional ER fluids, SLCs are formed due to a long-range effective attraction between the polarised particles. The interparticle interactions are known as 'long-range' if the interparticle distances are much greater than the characteristic dipole length.

In complex plasmas, the directed ion flow causes the formation of wake charges directly behind the particles, thereby modifying the interparticle potential. It was often believed that this resulted in effective attraction between the like-charged particles, analogous to conventional ER fluids. However, the findings in this study revealed that the process is not necessarily driven by attraction but rather by the reduced repulsion acting along the direction of ion flow.

Using an interparticle potential modified to include two wake charges (one on either side of the microparticle) to mimic an alternating ion flow, particles crystallised into SLCs in the simulations without the presence of long-range attraction. It was sufficient for the interparticle potential to be less repulsive than Yukawa in order to generate SLCs similar to those observed in experimental setups. Interestingly, simulations with long-range attraction led to instability issues (such as particles escaping the simulation box) due to strong particle accelerations.

Furthermore, I examined the destruction and recrystallization of SLCs in the 3D MD simulation in comparison with the experimental observations made using the PK-4 facility aboard the ISS. The experimental and simulated data were remarkably similar, thereby showing that long-range attraction is not necessary for SLC formation. Both simulated and experimental data also showed a slightly higher inter-string distance compared to the interparticle distance in a string, indicating a reduced repulsion along the direction of string formation. Additionally, estimates of the relaxation time suggest that the process of SLC formation is led by the diffusion of particles to their equilibrium positions, heavily influenced by the geometry of the shielding ion cloud.

The excellent qualitative agreement between the experimental and simulation results suggests that reducing repulsion along the direction of ion flow is a sufficient condition for the formation of SLCs in complex plasmas. So far, my colleagues and I have only aimed for a qualitative agreement as we are missing the method to calibrate the simulation parameters. Future experiments into the stability and deformation of SLCs could be used to calibrate the simulation parameters such as wake charge and distance in order to aim for quantitative results.

Chapter 7

Concluding remarks: overview and outlook

"There's more to explore here."

Outer Wilds Ventures

Ionised gases with micrometre-sized particles immersed in them are known as complex plasmas. The microparticles embedded in the plasma collect high numbers of electrons on their surfaces to become strongly negatively charged, which can cause them to become strongly coupled with each other. The interactions between individual particles can lead to the onset of collective behaviour, such as self-ordering and pattern formation. The suspension of microparticles in complex plasmas is optically thin, and each particle is large enough to be imaged directly. The observation technique of using an illumination laser and a high speed camera is non-disruptive to the microparticle dynamics, which not only allows for direct measurements of chaotic behaviour such as turbulence, but also enables experimental studies at the level of individual particles. This makes complex plasmas particularly advantageous model systems to study a variety of condensed mater phenomena and fluid effects. The collective motion due to many interactions between individual particles can lead to fascinating emergent behaviour in the whole microparticle suspension. Surface tension effects such as the self-formation of droplets, pattern formation, string formation, phase transitions between crystalline and fluid states, development of shocks, and the onset of turbulence are all forms of emergent phenomena that are discussed in this thesis.

The first collective behaviour of microparticles that I discussed in this thesis was the self-ordering of particles into droplet-like structures. This study was motivated by experimental observations of the self-formation of droplets in both the Zyflex chamber during a parabolic flight and the modified PK-3 Plus thermophoretic chamber on the ground. Both experiments saw the formation of a void in the center of the chamber. When a collection of microparticles was pushed into the void in both experiments, both times the particles condensed into droplets. The process of condensation in complex plasmas is entirely different from that in conventional fluids, such as water. Microparticles are all strongly negatively charged, and so it is surprising that hundreds to thousands of particles would self-condense into a droplet despite the high repulsion. Based on previous work studying the stability of microparticle structures, my colleagues and I suggested a mechanism based on the balance of the ion drag force and the electrostatic repulsion for a stable droplet formation.

This model was founded on the principle of balancing the forces on a particle at the droplet surface to study droplet stability. The model treats the ion drag force (known to lead to an effectively attractive potential between particles and probes in the plasma) as the cohesive force responsible for pushing the microparticles together, and the electrostatic repulsive force responsible for pushing the particles apart. At the equilibrium point where both forces balance, a droplet structure can be said to have formed. This equilibrium was checked to be a stable equilibrium through a thought experiment, and the resulting droplet radius was in agreement with the experimental observations.

This was surprising given the simplicity of the model, specially the assumption of spherical symmetry. The droplet observed during the parabolic flight experiment displayed radial anisotropies, and yet the model returned comparable results given the experimental parameters. Despite the clear limitation of only considering spherical droplets, the model is 'good enough' for a first prediction of the droplet radius.

There are further limitations of the model. The effect of ion shadowing and charge cannibalism was ignored entirely, and so was the impact of particle radius and, thus, mass and charge. A numerical study to compare with the analytical model is also entirely missing. This would be difficult to achieve, as molecular dynamics simulations do not simulate the plasma with the particles. Other simulation methods would be needed, which would still be challenging as the plasma and the microparticles move at vastly different timescales. Nevertheless, a simulation of the two forces acting on a collection of microparticles would be beneficial, and could be used to compare with these results and guide interpretations of the true cause of such surface tension-like effects in complex plasmas.

On the other hand, the strength and novelty of the model lie in the causal link suggested between the plasma parameters and the size of the droplet. Knowing the parameters, such as the electron temperature, the droplet size in an experiment can be predicted. Likewise, by observing a droplet in the experiment, the electron temperature can be estimated. This model therefore enables experimentally observed droplets to be used as a diagnostic tool to estimate the electron temperature in the plasma.

I investigated fluid effects in complex plasmas further in this thesis by studying a flow of microparticles past an obstacle. This study was entirely numerical. Multiple phenomena such as Mach cones, bow shocks, and turbulence were observed in 3D simulations with damping. I used the Mach cone observations to determine the speed of sound in the simulations, and also observed multiple Mach cones with different opening angles, implying that the secondary cones 'see' a smaller speed of sound compared to the primary cone. Bow shocks also showed a multi-part structure, with secondary 'reflected' bow shocks forming behind the obstacles due to recirculation zones as well as double bow shocks forming in front of the obstacle. To the best of my knowledge, this is the first time double bow shocks were reported in complex plasmas. These bow shocks were visually similar to those observed in astrophysical plasmas, although their generation mechanism is different as astrophysical bow shocks are produced due to interactions with magnetic fields instead of electric fields.

In the presence of damping, turbulence only appeared in regions where particles flowed directly into a shock. The increased particle density, and thus increased strength of interparticle interactions, led to the formation of vortices and, eventually, turbulence. The difficulty in studying turbulence in general is partly due to the fact that it does not have an exact definition. In this work, I compiled a list of commonly observed hallmarks of turbulence which I used as a working definition. These hallmarks included the presence of vorticies, a chaotic and disordered flow pattern, increased fluid mixing, increased flow resistance, and an energy cascade with a Kolmogorovian power law. For turbulence in damped systems, there is an additional condition that needs to be fulfilled: the rate of energy cascade needs to be higher than the damping rate. I checked each simulation for these signatures of turbulence, and if it they were all present I could confidently say that the flow is turbulent according to the working definition provided in this study.

In these simulations, I systematically changed flow parameters such as the speed and particle charge to understand their effect on the onset of turbulence. Just by changing one of these parameters, I was able to trigger turbulence in the simulations in a reproducible manner. The ability to consistently and systematically trigger turbulence allowed for a study of the transition from laminar to turbulent flow within a parameter regime available experimentally. The pressures I used in simulations are easily achievable with the COMPACT facility, enabling future experimental investigations based on these simulations. Furthermore, when I reduced the pressure down to 10^{-5} Pa to study undamped turbulence, the simulations produced results similar to turbulence in conventional fluids such as water without the presence of shocks. I also found that the onset of turbulence in complex plasmas follows the same pathway as in conventional fluids, through intermittency in the form of transient turbulent

puffs. This work then opens up a pathway to studying a transition from turbulence in undamped to damped fluids, as well as the transition from laminar to turbulent flow at a particle-resolved level.

Finally, I discussed the emergence of electrorheological effects in complex plasmas. This work was based on the experimental observations in the PK-4 lab on the ISS of microparticles crystallising into SLCs. These experiments formed the basis of the simulations, whose aim was to investigate the cause of the onset of SLC formation. The crystallisation of particles in SLCs occurred in the presence of a directed ion flow relative to the microparticles. This causes a deformation of the ion cloud leading to a buildup of excess positive charge in the wake of the particle, known as a positive ion wake. This ion wake modifies the interparticle potential such that the particles can form SLCs, and it was assumed that the modified interparticle potential due to the wakes would be (effectively) attractive at long-range. As such, the simulations also investigated whether the ion focusing downstream the microparticles due to a directed ion flow led to effective interparticle attraction, and whether that was behind the formation of SLCs.

The simulations demonstrated an excellent qualitative agreement with experiments, and showed that an effective interparticle attraction was not necessary. The simulations simply had a reduced repulsion along the direction of SLC formation, and that proved sufficient. In fact, in simulations where parameters were changed to produce interparticle attraction, particles experienced such high accelerations that they escaped the bounds of the simulation box. This instability had also been found in previous molecular dynamics simulations. Moreover, the timescale of SLC formation in both simulation and experiment was much longer than the timescale of velocity equilibration. This suggests that the process governing the formation of SLCs depends on more than just the temperature of the microparticles. Analysis of the diffusion coefficient suggested that the process is led by particle diffusion and is dependent on the geometry of the deformed ion (wake) cloud.

The excellent qualitative agreement between experimental and numerical data suggests that effective interparticle attraction is not necessary for the formation of SLCs in complex plasmas, and that a reduced repulsion is sufficient. The agreement is qualitative at best, since calibration methods to aim for quantitative results are so far lacking. Future investigations of SLC strength and stability could be used adjust and fine-tune the simulation parameters to match experiments more closely such that a quantitative comparison can be made.

Overall, I studied the emergence of a variety of collective effects in complex plasmas in this thesis within the framework of interparticle interactions. I studied how a multitude of interactions between individual particles can lead to collective behaviour that manifests as pattern formation or phase changes or even turbulence. The studies I presented in this thesis not only provide insight into the fundamental interactions of the microparticles, but also can be used as diagnostic tools for experimental research to either estimate plasma parameters or even trigger and allow better control of the onset of turbulence. The results of my thesis are not just limited to complex plasmas, but can also be used to understand the similarities and differences between complex plasmas and conventional fluids by understanding the onset of emergent phenomena in both. The field of complex plasmas is rich with complex phenomena that emerges naturally as a result of many interparticle interactions. The collective behaviour of particles leads to many more fascinating emergent phenomena that could be the focus of future studies.

Appendix A

LAMMPS input file to initialise 3D obstacle imulation

```
units si
dimension 3
atom_style charge
variable debye equal 100e-6 # m
lattice fcc 50e-6 # m

boundary pp pp pp

region box1 block 0 10e-3 0 3e-3 0 3e-3 units box
region box2 block 0.5e-3 4.5e-3 1e-3 1.5e-3 0.5e-3 0.9e-3 units box
region simbox union 2 box1 box2
create_box 2 simbox

create_atoms 1 region box2
group dust type 1
set type 1 charge -5.57e-16 # -3481 e
mass 1 3.053e-14 # kg

create_atoms 2 single 4.5e-3 1.5e-3 2e-3 # position of obstacle
set type 2 charge +5e-12 # roughly 10,000 times dust charge, +3×10^7 e
mass 2 10 # 16 orders of magnitude higher than dust mass
group obstacle type 2

variable kappa equal 1/v_debye
# cutoff for potential 10 times debye length
variable cutoff equal 10*v_debye
neigh_modify delay 0 every 1 check yes page 5000000 one 500000
pair_style coul/debye $kappa $cutoff
pair_coeff * * $cutoff

variable dust_radius equal 1.69e-6 # m
variable pressure equal 150 # Pa
variable coeff equal 6.0899e-6 # with Tn 300K, rho 1510kg/m3
variable gammaEp equal (v_coeff*v_pressure)/(v_dust_radius)
variable gamma equal 1.0/v_gammaEp
```

```
fix damping dust langevin 5000 5000 $gamma 38533 tally yes
fix_modify damping energy yes # adds to potential energy

timestep 1e-5
run 50000 # 0.5 s

# melt the lattice
fix melting dust temp/berendsen 5000 10000 1e-2

fix moveatoms all nve

thermo_style custom step temp pe ke epair etotal
thermo 100

# output visual images if needed
#dump visuals all image 100 im.*.png type type adiam 5e-5 zoom 1.6

run 50000 # 0.5 s

timestep 1e-4
run 30000 # 3 s

unfix melting

timestep 1e-3
unfix damping

variable pressure equal 30

fix damping_2 dust langevin 3000 3000 $gamma 298 tally yes
fix_modify damping_2 energy yes

run 20000 # 20 s

unfix damping_2
variable pressure equal 5
fix damping_3 dust langevin 1000 1000 $gamma 298 tally yes
fix_modify damping_3 energy yes

run 20000 # 20 s

# save current state of particles to a binary restart file
write_restart 3d_obstacle.restart

# save position and velocity data for the current state of particles
# and use it to check if equilibrium has been reached
# dump eql all custom 1 eql.csv id x y z vx vy vz
# run 0
```

Appendix B

LAMMPS input file for recrystallisation

```
# read previously saved particle states in a string
read_restart string_simulation.restart

variable Te equal 7.9
variable lambda_d equal 190e-6 # κ ∼ 1.2
variable pressure equal {gaspress}
variable dust_radius equal 1.9e-6
variable base_temp equal 300
variable kappa equal 1/v_lambda_d

# electron screening length
variable kappae equal v_kappa*sqrt(v_base_temp/(v_Te*11600))

# cutoff distance for potential
variable cutoff equal 7*v_lambda_d
variable Mth equal 0.7
variable wd equal {wake_d} # 55 used
variable wake_delta equal v_wd*1e-6 # 55e-6 m, or 55 um
variable wake_z equal {wake_c} # 0.2 used
pair_style coul/string $kappa $kappae $cutoff $wake_z $wake_delta $Mth
$dust_radius
pair_coeff * * $cutoff

neighbor 1e-4 bin
neigh_modify one 1000000
neigh_modify delay 0 every 1 check yes page 100000 one 10000

# final_temp to be reached during plasma off
variable final_temp equal {temp} # 1200 K used

# equilibrium temp for plasma on
variable eq_temp equal 300
variable coeff equal 6.0899e-6 # Tn 300K, rho 1510kg/m3

# epstein damping coefficient
variable gammaep equal (v_coeff*v_pressure)/v_dust_radius
variable gamma equal 1.0/v_gammaep # damping coeff with units of time
```

```
fix damping all langevin ${eq_temp} ${eq_temp} $gamma 38533 tally yes
fix_modify damping energy yes # adds to potential energy


# output information to screen every 100 timesteps
thermo_style custom step temp press pe ke epair etotal
thermo 100
fix moveatoms all nve
timestep 1e-5 # equal to 10 μs

# particle charge during plasma on -3481e
variable q equal -1.6e-19*3481

# rate of data collection is 1000 fps
dump data all custom 100 output.csv id x y z vx vy vz

# run for 1s
run 100000

# plasma gets turned off now
# increase thermostat temperature to final_temp during plasma off phase
unfix damping
fix heating all langevin ${final_temp} ${final_temp} $gamma 3248 tally
yes
fix_modify heating energy yes

# particle charge during plasma off -10e
variable q1 equal -1.6e-19*10
set atom * charge $q1

# simulate plasma off for 0.3s by heating the particles and reducing
particle charge
# run for 0.3s
run 30000

# plasma gets turned back on now
# reduce temperature and reset particle charge to -3481e
set atom * charge $q
unfix heating
fix new_damping all langevin ${eq_temp} ${eq_temp} $gamma 8973 tally yes
fix_modify new_damping energy yes

# run for 4.7s for a total run time of 5s
run 470000
```

List of Symbols

Constants

Symbol	Name	Value
ϵ_0	Vacuum permittivity	$8.85 \times 10^{-12}\ \mathrm{F/m}$
e	Elementary charge	$1.60 \times 10^{-19}\ \mathrm{C}$
g	Acceleration due to gravity on Earth	$9.81\mathrm{m/s^2}$
k_B	Boltzmann's constant	$1.38 \times 10^{-23}\ \mathrm{J/K}$

Abbreviations

Acronym	Description
2D	Two Dimensional
3D	Three Dimensional
AC	Alternating Current
DC	Direct Current
DML	Direct Motion Limited
FCC	Face-Centered Cubic
FPS	Frames Per Second
FWHM	Full Width at Half Maximum
ISS	International Space Station
LAMMPS	Large-scale Atomic/Molecular Massively Parallel Simulator
MD	Molecular Dynamics
MF	Melamine Formaldehyde
OML	Orbital Motion Limited
PIC	Particle In Cell
PK	Plasmakristall
PO	Particle Observation
RDF	Radial Distribution Function

RF	Radio Frequency
VDF	Velocity Distribution Function

Greek symbols

Symbol	Name	Units
α	Plasma ionisation fraction	-
χ	Measure of the ion streaming velocity in terms of the Mach number	-
ΔT	Temperature difference	K
δt	Timestep	s
Δ	Average interparticle distance	μm
δ	Duty cycle, $\delta = t_+/\mathcal{T}$	%
δ_{Ep}	Reflection parameter for neutral gas atoms	-
η	Kolmogorov length scale	μm
Γ	Coupling parameter	-
γ_{Ep}	Epstein damping coefficient	Hz, s
κ	Screening parameter, $\kappa = 1/\lambda_D$	$\mu\mathrm{m}^{-1}$
λ_{De}	Electron Debye length	μm
λ_{Di}	Ion Debye length	μm
λ_D	(Linearised) Debye length	μm
λ_s	Interpolated screening length	μm
$\ln\Lambda$	Coulomb logarithm	-
∇T_n	Temperature gradient of the gas	K/m
ν	Viscosity	mm^2/s
ω_{cas}	Cascade rate	Hz, s
Ω_E	Einstein frequency	Hz, s
ω_{px}	Plasma frequency, with $x \in i,\ e,\ d$ referring to ions, electrons, and dust	Hz, s
ϕ	Electric potential	V
Φ_C	Coulomb potential	V
Φ_Y	Yukawa potential	V
ρ_d	Microparticle mass density	$\mathrm{kg/m}^3$
σ	Cross section	$\mu\mathrm{m}^2$

τ	Ratio of electron to ion temperatures	-
τ_n	Kolmogorov time scale	s
τ_{px}	Time scale $1/\omega_{px}$, with $x \in i,\ e,\ d$ referring to ions, electrons, and dust	s
θ	Mach cone opening angle	rad
ε	Mean rate of energy dissipation per unit mass	$\mathrm{mm}^2/\mathrm{s}^3$
ξ	Collisionality parameter for DML theory	-
ζ	Angle between ion flow and vector connecting the microparticles	rad

Latin symbols

Symbol	Name	Units
a	Radius of dust particle	μm
A	Neutral gas atom	-
A^+	Positive gas ion	-
b	Impact parameter	μm
$b_{\pi/2}$	Impact parameter for a 90° deflection angle	μm
C	Capacitance	F
C_s	Sound speed	mm/s
D	Diffusion coefficient	m^2/s
e^-	Electron	-
E	Energy	eV
$\mathbf{E}$	Electric field	V/m
f	Frequency	Hz, s
F	Force (acting on the microparticles)	N
$g(r)$	Radial distribution function	-
g_{2D}	2D Pair correlation function	-
G	3D Pair correlation function	-
G_ϕ	Angular integral of $G(r, \theta, \phi)$	rad^{-1}
G_θ	Angular integral of $G(r, \theta, \phi)$	rad^{-1}
I	Current	A
k	Wave-vector	mm^{-1}
k_n	Thermal conductivity	W/mK

l	Mean free path	μm
L	Angular momentum	$\mathrm{kg\,m^2/s}$
m_x	Mass with $x \in i,\ e,\ d$ referring to ions, electrons, and dust	kg
$\mathcal{M}$	Mach number	-
$\mathcal{M}_{th}$	Ion thermal Mach number	-
n_x	Number density with $x \in i,\ e,\ d$ referring to ions, electrons, and dust	$\mathrm{m^{-3}}$
N	Number of dust particles	-
P	Pressure	Pa
q	Microparticle charge	C
r	Interparticle distance	μm
r_w	Wake distance	μm
R	Radius of droplet	mm
$\Re$	Reynolds number	-
t_+	Time duration where AC current is positive	s
T_x	Temperature with $x \in i,\ e,\ d$ referring to ions, electrons, and dust	K
$\mathcal{T}$	Period of AC current	s
v_i	Ion velocity	mm/s
v_x	Microparticle velocity along x-axis, similarly for y, and z	mm/s
w	Vorticity	$\mathrm{s^{-1}}$
w_c	Wake charge	-
Z_d	Number of electrons collected by a particle; Particle charge / e	-

List of Figures

List of Tables

References

[1] Thorne, K. & Blandford, R. *Plasma Physics: Volume 4 of Modern Classical Physics* (Princeton University Press, 2021). URL https://ui.adsabs.harvard.edu/abs/2021ppv..book.....T. Provided by the SAO/NASA Astrophysics Data System.

[2] Piel, A. *Definition of the Plasma State*, 29–43 (Springer Berlin Heidelberg, Berlin, Heidelberg, 2010). URL https://doi.org/10.1007/978-3-642-10491-6_2.

[3] Fridman, G. *et al.* Applied plasma medicine. *Plasma Processes and Polymers* **5**, 503–533 (2008). URL https://doi.org/10.1002/ppap.200700154.

[4] Laroussi, M. Plasma medicine: A brief introduction. *Plasma* **1**, 47–60 (2018). URL https://doi.org/10.3390/plasma1010005.

[5] Chizoba Ekezie, F.-G., Sun, D.-W. & Cheng, J.-H. A review on recent advances in cold plasma technology for the food industry: Current applications and future trends. *Trends in Food Science & Technology* **69**, 46–58 (2017). URL https://doi.org/10.1016/j.tifs.2017.08.007.

[6] Cullen, P. J. *et al.* Translation of plasma technology from the lab to the food industry. *Plasma Processes and Polymers* **15**, 1700085 (2018). URL https://doi.org/10.1002/ppap.201700085.

[7] Gomez, E. *et al.* Thermal plasma technology for the treatment of wastes: A critical review. *Journal of Hazardous Materials* **161**, 614–626 (2009). URL https://doi.org/10.1016/j.jhazmat.2008.04.017.

[8] Poulsen, R. G. Plasma etching in integrated circuit manufacture—a review. *Journal of Vacuum Science and Technology* **14**, 266–274 (1977). URL https://doi.org/10.1116/1.569137.

[9] Misra, S., Yu, L., Chen, W., Foldyna, M. & i Cabarrocas, P. R. A review on plasma-assisted vls synthesis of silicon nanowires and radial junction solar cells. *Journal of Physics D: Applied Physics* **47**, 393001 (2014). URL https://dx.doi.org/10.1088/0022-3727/47/39/393001.

[10] Winter, J. Dust: A new challenge in nuclear fusion research? *Physics of Plasmas* **7**, 3862–3866 (2000). URL https://doi.org/10.1063/1.1288911.

[11] Dap, S. *et al.* Agglomeration processes in carbonaceous dusty plasmas, experiments and numerical simulations. *New Journal of Physics* **12**, 093014 (2010). URL https://dx.doi.org/10.1088/1367-2630/12/9/093014.

[12] Winter, J. Dust in fusion devices - experimental evidence, possible sources and consequences. *Plasma Physics and Controlled Fusion* **40**, 1201 (1998). URL https://dx.doi.org/10.1088/0741-3335/40/6/022.

[13] Winter, J. Dust in fusion devices—a multi-faceted problem connecting high- and low-temperature plasma physics. *Plasma Physics and Controlled Fusion* **46**, B583 (2004). URL https://dx.doi.org/10.1088/0741-3335/46/12B/047.

[14] Blum, J. & Wurm, G. The growth mechanisms of macroscopic bodies in protoplanetary disks. *Annual Review of Astronomy and Astrophysics* **46**, 21–56 (2008). URL https://doi.org/10.1146/annurev.astro.46.060407.145152.

[15] Blum, J. Dust growth in protoplanetary disks — a comprehensive experimental/theoretical approach. *Research in Astronomy and Astrophysics* **10**, 1199 (2010). URL https://dx.doi.org/10.1088/1674-4527/10/12/002.

[16] Kimura, H., Mann, I. & Jessberger, E. K. Composition, structure, and size distribution of dust in the local interstellar cloud. *The Astrophysical Journal* **583**, 314 (2003). URL https://dx.doi.org/10.1086/345102.

[17] Sykes, M. V., Lebofsky, L. A., Hunten, D. M. & Low, F. The discovery of dust trails in the orbits of periodic comets. *Science* **232**, 1115–1117 (1986). URL https://doi.org/10.1126/science.232.4754.1115.

[18] Beltrán, M. T. & de Wit, W. J. Accretion disks in luminous young stellar objects. *The Astronomy and Astrophysics Review* **24** (2016). URL https://doi.org/10.1007/s00159-015-0089-z.

[19] Cassini-Huygens. Pia10423: Spokes on the wheel (2008). URL https://photojournal.jpl.nasa.gov/catalog/PIA10423. Image credit: NASA, JPL, Space Science Institute.

[20] Hubble. Lagoon nebula (visible-light view) (2018). URL https://www.nasa.gov/feature/goddard/2018/lagoon-nebula-visible-light-view. Image credit: NASA, ESA, and STScI.

[21] Yaroshenko, V. & Pustylnik, M. Possible mechanisms of string formation in complex plasmas at elevated pressures. *Molecules* **26** (2021). URL https://doi.org/10.3390/molecules26020308.

[22] Farine, D. R. Collective action in birds. *Current Biology* **32**, R1140–R1144 (2022). URL https://doi.org/10.1016/j.cub.2022.08.035.

[23] Bialek, W. *et al.* Statistical mechanics for natural flocks of birds. *Proceedings of the National Academy of Sciences* **109**, 4786–4791 (2012). URL https://doi.org/10.1073/pnas.1118633109.

[24] Usachev, A. D. *et al.* Formation of a boundary-free dust cluster in a low-pressure gas-discharge plasma. *Physical Review Letters* **102**, 045001 (2009). URL https://doi.org/10.1103/PhysRevLett.102.045001.

[25] Schwabe, M. *et al.* Formation of bubbles, blobs, and surface cusps in complex plasmas. *Physical Review Letters* **102**, 255005 (2009). URL https://doi.org/10.1103/PhysRevLett.102.255005.

[26] Schwabe, M. *Dynamical effects in fluid complex plasmas*. Ph.D. thesis, Ludwig-Maximilians-Universität (2009).

[27] Annaratone, B. M. *et al.* Collective effects in complex plasma. *Plasma Sourc. Sci. Techn.* **19**, 065026 (2010). URL https://doi.org/10.1088/0963-0252/19/6/065026.

[28] Asinovskii, E., Kirillin, A. & Markovets, V. Plasma coagulation of microparticles on cooling of glow discharge by liquid helium. *Phys. Lett. A* **350**, 126–128 (2006). URL https://doi.org/10.1016/j.physleta.2005.08.098.

[29] Antipov, S. N., Vasiliev, M. M. & Petrov, O. F. Non-ideal dust structures in cryogenic complex plasmas. *Contrib. Plasma Phys.* **52**, 203–206 (2012). URL https://doi.org/10.1002/ctpp.201100082.

[30] NASA. Supersonic bullet (2007). URL https://www.nasa.gov/mission_pages/galex/20070815/f.html. Image courtesy of Andrew Davidhazy/Rochester Institute of Technology. Accessed 25/02/2023.

[31] photo by Mass Communication Specialist 3rd Class Travis K. Mendoza, U. N. F-a-18c hornet in transonic flight, with condensation cones (2011). URL https://commons.wikimedia.org/wiki/File:F-A-18C_Hornet_in_transonic_flight,_with_condensation_cones.jpg. Public domain, via Wikimedia Commons.

[32] Colagrossi, A., Marrone, S., Colagrossi, P. & Le Touzé, D. Da vinci's observation of turbulence: A french-italian study aiming at numerically reproducing the physics behind one of his drawings, 500 years later. *Physics of Fluids* **33**, 115122 (2021). URL https://doi.org/10.1063/5.0070984.

[33] van Gogh, V. The starry night (1889). URL https://www.ibiblio.org/wm/paint/auth/gogh/starry-night/. Oil on Canvas, 72 x 92 cm (29 x 36 1/4 in); The Museum of Modern Art, New York. Accessed 17/07/2023.

[34] Nazarenko, S. & Lukaschuk, S. Wave turbulence on water surface. *Annual Review of Condensed Matter Physics* **7**, 61–88 (2016). URL https://doi.org/10.1146/annurev-conmatphys-071715-102737.

[35] Falcon, E. & Mordant, N. Experiments in surface gravity–capillary wave turbulence. *Annual Review of Fluid Mechanics* **54**, 1–25 (2022). URL https://doi.org/10.1146/annurev-fluid-021021-102043.

[36] Busch, N. E. & Panofsky, H. A. Recent spectra of atmospheric turbulence. *Quarterly Journal of the Royal Meteorological Society* **94**, 132–148 (1968). URL https://rmets.onlinelibrary.wiley.com/doi/10.1002/qj.49709440003.

[37] Goldstein, M. L., Roberts, D. A. & Matthaeus, W. H. Magnetohydrodynamic turbulence in the solar wind. *Annual Review of Astronomy and Astrophysics* **33**, 283–325 (1995). URL https://doi.org/10.1146/annurev.aa.33.090195.001435.

[38] Pramanik, J., Veeresha, B., Prasad, G., Sen, A. & Kaw, P. Experimental observation of dust-acoustic wave turbulence. *Physics Letters A* **312**, 84–90 (2003). URL https://www.sciencedirect.com/science/article/pii/S0375960103006145.

[39] Tsai, Y.-Y., Chang, M.-C. & I, L. Observation of multifractal intermittent dust-acoustic-wave turbulence. *Physical Review E* **86**, 045402 (2012). URL https://doi.org/10.1103/PhysRevE.86.045402.

[40] Schwabe, M. *et al.* Collective effects in vortex movements in complex plasmas. *Physical Review Letters* **112**, 115002 (2014). URL https://doi.org/10.1103/PhysRevLett.112.115002.

[41] Zhdanov, S., Schwabe, M., Räth, C., Thomas, H. M. & Morfill, G. E. Wave turbulence observed in an auto-oscillating complex (dusty) plasma. *Europhysics Letters* **110**, 35001 (2015). URL https://doi.org/10.1209/0295-5075/110/35001.

[42] Schwabe, M., Zhdanov, S. & Räth, C. Instability onset and scaling laws of an auto-oscillating turbulent flow in a complex plasma. *Physical Review E* **95**, 041201 (2017). URL https://doi.org/10.1103/PhysRevE.95.041201.

[43] Schwabe, M., Zhdanov, S. & Räth, C. Turbulence in an auto-oscillating complex plasma. *IEEE Transactions on Plasma Science* **46**, 684–687 (2018). URL https://doi.org/10.1109/TPS.2017.2744682.

[44] Ivlev, A. V. *et al.* First observation of electrorheological plasmas. *Physical Review Letters* **100**, 095003 (2008). URL https://doi.org/10.1103/PhysRevLett.100.095003.

[45] Wörner, L. *et al.* String structures in driven 3d complex-plasma clusters. *Europhysics Letters* **100**, 35001 (2012). URL https://dx.doi.org/10.1209/0295-5075/100/35001.

[46] Mitic, S., Klumov, B. A., Khrapak, S. A. & Morfill, G. E. Three dimensional complex plasma structures in a combined radio frequency and direct current discharge. *Physics of Plasmas* **20**, 043701. URL https://doi.org/10.1063/1.4798418.

[47] Pustylnik, M. Y. *et al.* Three-dimensional structure of a string-fluid complex plasma. *Physical Review Research* **2**, 033314 (2020). URL https://doi.org/10.1103/PhysRevResearch.2.033314.

[48] Mitic, S. *et al.* Long-term evolution of the three-dimensional structure of string-fluid complex plasmas in the pk-4 experiment. *Physical Review E* **103**, 063212 (2021). URL https://doi.org/10.1103/PhysRevE.103.063212.

[49] Adriani, P. M. & Gast, A. P. A microscopic model of electrorheology. *Physics of Fluids* **31**, 2757 (1988). URL https://doi.org/10.1063/1.866983.

[50] Chen, T., Zitter, R. N. & Tao, R. Laser diffraction determination of the crystalline structure of an electrorheological fluid. *Physical Review Letters* **68**, 2555–2558 (1992). URL https://doi.org/10.1103/physrevlett.68.2555.

[51] Dassanayake, U., Fraden, S. & van Blaaderen, A. Structure of electrorheological fluids. *J. Chem. Phys.* **112**, 3851–3858 (2000). URL https://doi.org/10.1063/1.480933.

[52] Liu, Y. D. & Choi, H. J. Electrorheological fluids: smart soft matter and characteristics. *Soft Matter* **8**, 11961 (2012). URL https://doi.org/10.1039/c2sm26179k.

[53] Aoyama, T. & Inasaki, I. Application of electrorheological fluid dampers to machine tool elements. *CIRP Annals* **46**, 309–312 (1997). URL https://doi.org/10.1016/S0007-8506(07)60832-4.

[54] Oh, H.-U., Onoda, J. & Minesugi, K. Semiactive Isolator With Liquid-Crystal Type ER Fluid for Momentum-Wheel Vibration Isolation . *Journal of Vibration and Acoustics* **126**, 272–277 (2004). URL https://doi.org/10.1115/1.1646418.

[55] Tan, K., Stanway, R. & Bullough, W. Braking responses of inertia/load by using an electro-rheological (er) brake. *Mechatronics* **17**, 277–289 (2007). URL https://doi.org/10.1016/j.mechatronics.2007.04.005.

[56] Han, Y.-M. & Choi, S.-B. Control of an er haptic master in a virtual slave environment for minimally invasive surgery applications. *Smart Materials and Structures* **17**, 065012 (2008). URL https://dx.doi.org/10.1088/0964-1726/17/6/065012.

[57] Hwang, Y.-H., Kang, S.-R., Cha, S.-W. & Choi, S.-B. An electrorheological spherical joint actuator for a haptic master with application to robot-assisted cutting surgery. *Sensors and Actuators A: Physical* **249**, 163–171 (2016). URL https://doi.org/10.1016/j.sna.2016.08.033.

[58] Madeja, J., Kesy, Z. & Kesy, A. Application of electrorheological fluid in a hydrodynamic clutch. *Smart Materials and Structures* **20**, 105005 (2011). URL https://dx.doi.org/10.1088/0964-1726/20/10/105005.

[59] Hammerberg, J., Lemons, D., Murillo, M. & Winske, D. Molecular dynamics simulations of plasma crystal formation including wake effects. *IEEE Transactions on Plasma Science* **29**, 247–255 (2001). URL https://doi.org/10.1109/27.923702.

[60] Schwabe, M. *et al.* Slowing of acoustic waves in electrorheological and string-fluid complex plasmas. *New Journal of Physics* **22**, 083079 (2020). URL https://dx.doi.org/10.1088/1367-2630/aba91b.

[61] Rothermel, H., Hagl, T., Morfill, G. E., Thoma, M. H. & Thomas, H. M. Gravity compensation in complex plasmas by application of a temperature gradient. *Physical Review Letters* **89**, 175001 (2002). URL https://doi.org/10.1103/PhysRevLett.89.175001.

[62] Schablinski, J., Wieben, F. & Block, D. An optical tweezer for complex plasmas. *Physics of Plasmas* **22**, 043703 (2015). URL https://doi.org/10.1063/1.4916969.

[63] Samsonov, D., Zhdanov, S., Morfill, G. & Steinberg, V. Levitation and agglomeration of magnetic grains in a complex (dusty) plasma with magnetic field. *New Journal of Physics* **5**, 24 (2003). URL https://dx.doi.org/10.1088/1367-2630/5/1/324.

[64] Nefedov, A. P. *et al.* Pke-nefedov*: plasma crystal experiments on the international space station. *New Journal of Physics* **5**, 33 (2003). URL https://dx.doi.org/10.1088/1367-2630/5/1/333.

[65] Thomas, H. M. *et al.* Complex plasma laboratory pk-3 plus on the international space station. *New J. Phys.* **10**, 033036 (2008). URL https://doi.org/10.1088/1367-2630/10/3/033036.

[66] Thoma, M. H. *et al.* Pk-4: Complex plasmas in space—the next generation. *IEEE Transactions on Plasma Science* **35**, 255–259 (2007). URL https://doi.org/10.1109/TPS.2007.893750.

[67] Knapek, C. A. *et al.* "zyflex": Next generation plasma chamber for complex plasma research in space. *Review of Scientific Instruments* **92**, 103505 (2021). URL https://doi.org/10.1063/5.0062165.

[68] Knapek, C. A. *et al.* Compact—a new complex plasma facility for the iss. *Plasma Physics and Controlled Fusion* **64**, 124006 (2022). URL https://dx.doi.org/10.1088/1361-6587/ac9ff0.

[69] Thomas, H. M. *et al.* Complex plasma research on the International Space Station. *Plasma Phys. Control. Fusion* **61**, 014004 (2019). URL https://doi.org/10.1088/1361-6587/aae468.

[70] Pustylnik, M. Y. *et al.* Plasmakristall-4: New complex (dusty) plasma laboratory on board the international space station. *Review of Scientific Instruments* **87**, 093505 (2016). URL https://doi.org/10.1063/1.4962696.

[71] Knapek, C. A. *et al.* Ekoplasma - experiments with grid electrodes in microgravity. *AIP Conference Proceedings* **1925**, 020004 (2018). URL https://doi.org/10.1063/1.5020392.

[72] Langmuir, I. Oscillations in ionized gases. *Proceedings of the National Academy of Sciences* **14**, 627–637 (1928). URL https://doi.org/10.1073/pnas.14.8.627.

[73] Bohm, D. The characteristics of electrical discharges in magnetic fields. *Qualitative Description of the Arc Plasma in a Magnetic Field* (1949). URL https://archive.org/details/in.ernet.dli.2015.169225.

[74] Khrapak, S. A. *et al.* Particle flows in a dc discharge in laboratory and microgravity conditions. *Physical Review E* **87** (2013). URL https://doi.org/10.1103/physreve.87.063109.

[75] Heijmans, L. C. J. & Nijdam, S. Triboelectric and plasma charging of microparticles. *Europhysics Letters* **114**, 64004 (2016). URL https://dx.doi.org/10.1209/0295-5075/114/64004.

[76] Melzer, A. *Physics of Dusty Plasmas*, vol. 962 of *Lecture Notes in Physics* (Springer, 2019). URL https://doi.org/10.1007/978-3-030-20260-6.

[77] Morfill, G. E. *et al.* The 'classical tunnelling effect'—observations and theory. *New Journal of Physics* **8**, 7 (2006). URL https://dx.doi.org/10.1088/1367-2630/8/1/007.

[78] Jellum, G. M., Daugherty, J. E. & Graves, D. B. Particle thermophoresis in low pressure glow discharges. *Journal of Applied Physics* **69**, 6923–6934 (1991). URL https://doi.org/10.1063/1.347630.

[79] Vestner, H. & Waldmann, L. Generalized hydrodynamics of thermal transpiration, thermal force and friction force. *Physica A: Statistical Mechanics and its Applications* **86**, 303–336 (1977). URL https://doi.org/10.1016/0378-4371(77)90033-4.

[80] Barnes, M. S., Keller, J. H., Forster, J. C., O'Neill, J. A. & Coultas, D. K. Transport of dust particles in glow-discharge plasmas. *Physical Review Letters* **68**, 313–316 (1992). URL https://doi.org/10.1103/PhysRevLett.68.313.

[81] Khrapak, S. A., Ivlev, A. V., Zhdanov, S. K. & Morfill, G. E. Hybrid approach to the ion drag force. *Phys. Plasmas* **12**, 042308 (2005). URL https://doi.org/10.1063/1.1867995.

[82] Hutchinson, I. H. Collisionless ion drag force on a spherical grain. *Plasma Physics and Controlled Fusion* **48**, 185 (2006). URL https://dx.doi.org/10.1088/0741-3335/48/2/002.

[83] Liu, B., Goree, J., Nosenko, V. & Boufendi, L. Radiation pressure and gas drag forces on a melamine-formaldehyde microsphere in a dusty plasma. *Physics of Plasmas* **10**, 9–20 (2003). URL https://doi.org/10.1063/1.1526701.

[84] Wong, C.-S., Goree, J. & Haralson, Z. Einstein frequency measurement for a strongly coupled dusty plasma. *IEEE Transactions on Plasma Science* **46**, 763–767 (2018). URL https://doi.org/10.1109/TPS.2017.2746012.

[85] Kalman, G. J., Hartmann, P., Donkó, Z. & Rosenberg, M. Two-dimensional yukawa liquids: Correlation and dynamics. *Physical Review Letters* **92**, 065001 (2004). URL https://doi.org/10.1103/PhysRevLett.92.065001.

[86] Ivlev, A. V., Thoma, M. H., Räth, C., Joyce, G. & Morfill, G. E. Complex plasmas in external fields: The role of non-hamiltonian interactions. *Physical Review Letters* **106**, 155001 (2011). URL https://doi.org/10.1103/PhysRevLett.106.155001.

[87] Morfill, G. E. & Ivlev, A. V. Complex plasmas: An interdisciplinary research field. *Rev. Mod. Phys.* **81**, 1353–1404 (2009). URL https://doi.org/10.1103/RevModPhys.81.1353.

[88] Hof, B., van Doorne, C. W. H., Westerweel, J. & Nieuwstadt, F. T. M. Turbulence regeneration in pipe flow at moderate reynolds numbers. *Physical Review Letters* **95**, 214502 (2005). URL https://doi.org/10.1103/PhysRevLett.95.214502.

[89] Smits, A. J., McKeon, B. J. & Marusic, I. High–reynolds number wall turbulence. *Annual Review of Fluid Mechanics* **43**, 353–375 (2011). URL https://doi.org/10.1146/annurev-fluid-122109-160753.

[90] Linkmann, M., Boffetta, G., Marchetti, M. C. & Eckhardt, B. Phase transition to large scale coherent structures in two-dimensional active matter turbulence. *Physical Review Letters* **122**, 214503 (2019). URL https://doi.org/10.1103/PhysRevLett.122.214503.

[91] Hayes, W. *Hypersonic flow theory* (Elsevier, 2012). ISBN (eBook): 9780323148764.

[92] Samsonov, D., Goree, J., Thomas, H. M. & Morfill, G. E. Mach cone shocks in a two-dimensional yukawa solid using a complex plasma. *Physical Review E* **61**, 5557–5572 (2000). URL https://doi.org/10.1103/PhysRevE.61.5557.

[93] Jiang, K. *et al.* Mach cones in a three-dimensional complex plasma. *Europhysics Letters* **85**, 45002 (2009). URL https://dx.doi.org/10.1209/0295-5075/85/45002.

[94] Miloch, W. J. Wake effects and mach cones behind objects. *Plasma Physics and Controlled Fusion* **52**, 124004 (2010). URL https://dx.doi.org/10.1088/0741-3335/52/12/124004.

[95] Charan, H. & Ganesh, R. Supersonic flows past an obstacle in yukawa liquids. *Physics of Plasmas* **25**, 043706 (2018). URL https://doi.org/10.1063/1.5025361.

[96] Usachev, A. *et al.* Externally excited planar dust acoustic shock waves in a strongly coupled dusty plasma under microgravity conditions. *New Journal of Physics* **16**, 053028 (2014). URL https://dx.doi.org/10.1088/1367-2630/16/5/053028.

[97] Jaiswal, S., Bandyopadhyay, P. & Sen, A. Experimental investigation of flow induced dust acoustic shock waves in a complex plasma. *Physics of Plasmas* **23**, 083701 (2016). URL https://doi.org/10.1063/1.4960032.

[98] Marciante, M. & Murillo, M. S. Thermodynamic and kinetic properties of shocks in two-dimensional yukawa systems. *Physical Review Letters* **118**, 025001 (2017). URL https://doi.org/10.1103/PhysRevLett.118.025001.

[99] Lin, W., Murillo, M. S. & Feng, Y. Pressure and energy of compressional shocks in two-dimensional yukawa systems. *Physical Review E* **100**, 043203 (2019). URL https://doi.org/10.1103/PhysRevE.100.043203.

[100] Kananovich, A. & Goree, J. Experimental determination of shock speed versus exciter speed in a two-dimensional dusty plasma. *Physical Review E* **101**, 043211 (2020). URL https://doi.org/10.1103/PhysRevE.101.043211.

[101] Arora, G., Bandyopadhyay, P., Hariprasad, M. G. & Sen, A. Excitation of dust acoustic shock waves in an inhomogeneous dusty plasma. *Physics of Plasmas* **27**, 083703 (2020). URL https://doi.org/10.1063/5.0009397.

[102] Lin, W., Murillo, M. S. & Feng, Y. Universal relationship of compression shocks in two-dimensional yukawa systems. *Physical Review E* **101**, 013203 (2020). URL https://doi.org/10.1103/PhysRevE.101.013203.

[103] Havnes, O., Hartquist, T. W., Brattli, A., Kroesen, G. M. W. & Morfill, G. Dynamic mach cone as a diagnostic method in reactive dusty plasma experiments. *Physical Review E* **65**, 045403 (2002). URL https://doi.org/10.1103/PhysRevE.65.045403.

[104] Zhdanov, S. K., Morfill, G. E., Samsonov, D., Zuzic, M. & Havnes, O. Origin of the curved nature of mach cone wings in complex plasmas. *Physical Review E* **69**, 026407 (2004). URL https://doi.org/10.1103/PhysRevE.69.026407.

[105] Saitou, Y., Nakamura, Y., Kamimura, T. & Ishihara, O. Bow shock formation in a complex plasma. *Physical Review Letters* **108**, 065004 (2012). URL https://doi.org/10.1103/PhysRevLett.108.065004.

[106] Zhao, X. & Seyler, C. E. Computational extended magneto-hydrodynamical study of shock structure generated by flows past an obstacle. *Physics of Plasmas* **22**, 072102 (2015). URL https://doi.org/10.1063/1.4923426.

[107] Pandey, V., Perlekar, P. & Mitra, D. Clustering and energy spectra in two-dimensional dusty gas turbulence. *Physical Review E* **100**, 013114 (2019). URL https://doi.org/10.1103/PhysRevE.100.013114.

[108] Hu, H.-W., Wang, W. & I, L. Multiscale coherent excitations in microscopic acoustic wave turbulence of cold dusty plasma liquids. *Physical Review Letters* **123**, 065002 (2019). URL https://doi.org/10.1103/PhysRevLett.123.065002.

[109] Gogia, G., Yu, W. & Burton, J. C. Intermittent turbulence in a many-body system. *Physical Review Research* **2**, 023250 (2020). URL https://doi.org/10.1103/PhysRevResearch.2.023250.

[110] Kostadinova, E. G. *et al.* Fractional Laplacian spectral approach to turbulence in a dusty plasma monolayer. *Physics of Plasmas* **28**, 073705 (2021). URL https://doi.org/10.1063/5.0047649.

[111] Bajaj, P., Ivlev, A., Räth, C. & Schwabe, M. Studying turbulence in a fluid with background damping. *Physical Review E* **107**, 064603 (2023). URL https://doi.org/10.1103/PhysRevE.107.064603.

[112] Carter, T. A. Intermittent turbulence and turbulent structures in a linear magnetized plasma. *Physics of Plasmas* **13** (2006). URL https://doi.org/10.1063/1.2158929.

[113] Boffetta, G. & Ecke, R. E. Two-dimensional turbulence. *Annual Review of Fluid Mechanics* **44**, 427–451 (2012). URL https://doi.org/10.1146/annurev-fluid-120710-101240.

[114] Boer, G. J. & Shepherd, T. G. Large-scale two-dimensional turbulence in the atmosphere. *Journal of Atmospheric Sciences* **40**, 164 – 184 (1983). URL https://doi.org/10.1175/1520-0469(1983)040<0164:LSTDTI>2.0.CO;2.

[115] Chavanis, P.-H. Statistical mechanics of geophysical turbulence: application to jovian flows and jupiter's great red spot. *Physica D: Nonlinear Phenomena* **200**, 257–272 (2005). URL https://doi.org/10.1016/j.physd.2004.11.004.

[116] Frisch, U. *Turbulence: The Legacy of A.N. Kolmogorov* (Cambridge University Press, 1995). URL https://doi.org/10.1017/CBO9781139170666.

[117] Isichenko, M. B. Percolation, statistical topography, and transport in random media. *Rev. Mod. Phys.* **64**, 961–1043 (1992). URL https://doi.org/10.1103/RevModPhys.64.961.

[118] Mullin, T. Experimental studies of transition to turbulence in a pipe. *Annual Review of Fluid Mechanics* **43**, 1–24 (2011). URL https://doi.org/10.1146/annurev-fluid-122109-160652.

[119] Brown, R. L. & Bolt, R. H. The Measurement of Flow Resistance of Porous Acoustic Materials. *The Journal of the Acoustical Society of America* **13**, 337–344 (1942). URL https://doi.org/10.1121/1.1916184.

[120] Reynolds, O. Iii. an experimental investigation of the circumstances which determine whether the motion of water shall be direct or sinuous, and of the law of resistance in parallel channels. *Proceedings of the Royal Society of London* **35**, 84–99 (1883). URL https://royalsocietypublishing.org/doi/abs/10.1098/rspl.1883.0018.

[121] Kolmogorov, A. N. Equations of turbulent motion in an incompressible fluid. *Dokl. Akad. Nauk SSSR* **30**, 299–303 (1941).

[122] Kolmogorov, A. N., Levin, V., Hunt, J. C. R., Phillips, O. M. & Williams, D. Dissipation of energy in the locally isotropic turbulence. *Proceedings of the Royal Society of London. Series A: Mathematical and Physical Sciences* **434**, 15–17 (1991).

[123] Aragón, J. L., Bai, M., Torres, M. & Maini, P. K. Turbulent luminance in impassioned van gogh paintings. *Journal of Mathematical Imaging and Vision* **30**, 275–283 (2008). URL https://doi.org/10.1007/s10851-007-0055-0.

[124] Beattie, J. & Kriel, N. Is the starry night turbulent? (2019). URL https://doi.org/10.48550/arXiv.1902.03381. 1902.03381.

[125] Landahl, M. & Mollo-Christensen, E. *Turbulence and Random Processes in Fluid Mechanics*. Turbulence and Random Processes in Fluid Mechanics (Cambridge University Press, 1992). URL https://books.google.de/books?id=kuEbVysviOMC.

[126] Burgers, J. A mathematical model illustrating the theory of turbulence. vol. 1 of *Advances in Applied Mechanics*, 171–199 (Elsevier, 1948). URL https://doi.org/10.1016/S0065-2156(08)70100-5.

[127] Wiener, N. Generalized harmonic analysis. *Acta Mathematica* **55**, 117 – 258 (1930). URL https://doi.org/10.1007/BF02546511.

[128] Khintchine, A. Korrelationstheorie der stationären stochastischen prozesse. *Mathematische Annalen* **109**, 604–615 (1934). URL https://doi.org/10.1007/BF01449156.

[129] Dietz, C., Budak, J., Kamprich, T., Kretschmer, M. & Thoma, M. H. Phase transition in electrorheological plasmas. *Contributions to Plasma Physics* **61**, e202100079 (2021). URL https://doi.org/10.1002/ctpp.202100079.

[130] Molotkov, V. I., Nefedov, A. P., Torchinskii, V. M., Fortov, V. E. & Khrapak, A. G. Dust acoustic waves in a dc glow-discharge plasma. *Journal of Experimental and Theoretical Physics* **49**, 477–480 (1999). URL https://doi.org/10.1134/1.559006.

[131] Ivlev, A. V. *et al.* Electrorheological complex plasmas. *IEEE Transactions on Plasma Science* **38**, 733–740 (2010). URL https://doi.org/10.1109/TPS.2009.2037716.

[132] Park, C. & Robertson, R. E. Alignment of particles by an electric field. *Materials Science and Engineering: A* **257**, 295–311 (1998). URL https://doi.org/10.1016/S0921-5093(98)00848-X.

[133] Kana, D., Dietz, C. & Thoma, M. H. Simulation of electrorheological plasmas with superthermal ion drift. *Physics of Plasmas* **27**, 103703 (2020). URL https://doi.org/10.1063/5.0010021.

[134] Ishihara, O. & Vladimirov, S. V. Wake potential of a dust grain in a plasma with ion flow. *Physics of Plasmas* **4**, 69–74 (1997). URL https://doi.org/10.1063/1.872112.

[135] Takahashi, K., Oishi, T., Shimomai, K.-i., Hayashi, Y. & Nishino, S. Analyses of attractive forces between particles in coulomb crystal of dusty plasmas by optical manipulations. *Phys. Rev. E* **58**, 7805–7811 (1998). URL https://doi.org/10.1103/PhysRevE.58.7805.

[136] Hrabovsky, G. & Susskind, L. *Classical mechanics: the theoretical minimum* (Penguin UK, 2020).

[137] Plimpton, S. Fast parallel algorithms for short-range molecular dynamics. *Journal of Computational Physics* **117**, 1–19 (1995). URL https://doi.org/10.1006/jcph.1995.1039.

[138] Thompson, A. P. *et al.* Lammps - a flexible simulation tool for particle-based materials modeling at the atomic, meso, and continuum scales. *Computer Physics Communications* **271**, 108171 (2022). URL https://doi.org/10.1016/j.cpc.2021.108171.

[139] Schwabe, M. & Graves, D. B. Simulating the dynamics of complex plasmas. *Physical Review E* **88**, 023101 (2013). URL https://doi.org/10.1103/PhysRevE.88.023101.

[140] Tiwari, S. K. & Sen, A. Fore-wake excitations from moving charged objects in a complex plasma. *Physics of Plasmas* **23**, 100705 (2016). URL https://doi.org/10.1063/1.4964908.

[141] Du, C.-R. *et al.* Slow dynamics in a quasi-two-dimensional binary complex plasma. *Physical Review Letters* **123**, 185002 (2019). URL https://doi.org/10.1103/PhysRevLett.123.185002.

[142] Huang, H., Schwabe, M., Thomas, H. M., Lipaev, A. M. & Du, C.-R. Penetration of a supersonic particle at the interface in a binary complex plasma. *Physical Review E* **103**, 013205 (2021). URL https://doi.org/10.1103/PhysRevE.103.013205.

[143] Fu, Z.-C., Zampetaki, A., Huang, H. & Du, C.-R. Dispersion relation of square lattice waves in a two-dimensional binary complex plasma. *Physics of Plasmas* **28**, 014502 (2021). URL https://doi.org/10.1063/5.0026106.

[144] Singh, S., Bandyopadhyay, P., Kumar, K. & Sen, A. Square lattice formation in a monodisperse complex plasma. *Physical Review Letters* **129**, 115003 (2022). URL https://doi.org/10.1103/PhysRevLett.129.115003.

[145] Lammps (2003). URL https://github.com/lammps/lammps. Copyright Sandia Corporation, GNU General Public License version 2 (GPLv2).

[146] Joshi, E. & Schwabe, M. Strings extension [computer software] (2022). URL https://github.com/EshitaJoshi/strings_extension.

[147] Li, B. *et al.* Effects of dust particle number on the structure and dynamics in a binary complex plasma system by langevin dynamics simulation. *Computer Physics Communications* **284**, 108612 (2023). URL https://doi.org/10.1016/j.cpc.2022.108612.

[148] Schneider, T. & Stoll, E. Molecular-dynamics study of a three-dimensional one-component model for distortive phase transitions. *Physical Review B* **17**, 1302–1322 (1978). URL https://doi.org/10.1103/PhysRevB.17.1302.

[149] Verlet, L. Computer "experiments" on classical fluids. i. thermodynamical properties of lennard-jones molecules. *Physical Review* **159**, 98–103 (1967). URL https://doi.org/10.1103/PhysRev.159.98.

[150] Swope, W. C., Andersen, H. C., Berens, P. H. & Wilson, K. R. A computer simulation method for the calculation of equilibrium constants for the formation of physical clusters of molecules: Application to small water clusters. *The Journal of Chemical Physics* **76**, 637–649 (1982). URL https://doi.org/10.1063/1.442716.

[151] Feng, Y., Goree, J., Liu, B. & Cohen, E. G. D. Green-kubo relation for viscosity tested using experimental data for a two-dimensional dusty plasma. *Physical Review E* **84**, 046412 (2011). URL https://doi.org/10.1103/PhysRevE.84.046412.

[152] Nosenko, V. *et al.* Shear flow in a three-dimensional complex plasma in microgravity conditions. *Physical Review Research* **2**, 033404 (2020). URL https://doi.org/10.1103/PhysRevResearch.2.033404.

[153] Melzer, A. *et al.* Finite dust clusters in dusty plasmas. *Plasma Phys. Control. Fusion* **52**, 124028 (2010). URL https://doi.org/10.1088/0741-3335/52/12/124028.

[154] Petrov, O. F. & Fortov, V. E. Collective phenomena in strongly coupled dissipative systems of charged dust: from ground to microgravity experiments. *Contributions to Plasma Physics* **53**, 767–777 (2013). URL https://doi.org/10.1002/ctpp.201310052.

[155] Miloshevsky, G. V. & Hassanein, A. Self-confinement of finite dust clusters in isotropic plasmas. *Physical Review E* **85**, 056405 (2012). URL https://doi.org/10.1103/PhysRevE.85.056405.

[156] Tsytovich, V. A possibility of attraction of negative charges and formation of a new state of matter in plasma. *Comm. Plasma Phys. Control. Fusion* **15**, 349–358 (1994).

[157] Ignatov, A. M. Lesage gravity in dusty plasmas. *Plasma Phys. Rep.* **22**, 585–589 (1996).

[158] Khrapak, S. A. & Morfill, G. E. A note on the binary interaction potential in complex (dusty) plasmas. *Phys. Plasmas* **15**, 084502 (2008). URL https://doi.org/10.1063/1.2967483.

[159] Lampe, M. & Joyce, G. Grain-grain interaction in stationary dusty plasma. *Phys. Plasmas* **22**, 023704 (2015). URL https://doi.org/10.1063/1.4907649.

[160] Tsytovich, V. N. & Morfill, G. E. Collective attraction of equal-sign charged grains in plasmas. *Plasma Phys. Rep.* **28**, 171–176 (2002). URL https://doi.org/10.1134/1.1458982.

[161] Lisina, I. I., Lisin, E. A., Vaulina, O. S. & Petrov, O. F. Self-confined particle pairs in complex plasmas. *Physical Review E* **95** (2017). URL https://doi.org/10.1103/physreve.95.013202.

[162] Morfill, G. E. *et al.* Condensed plasmas under microgravity. *Physical Review Letters* **83**, 1598–1601 (1999). URL https://doi.org/10.1103/physrevlett.83.1598.

[163] Goree, J., Morfill, G. E., Tsytovich, V. N. & Vladimirov, S. V. Theory of dust voids in plasmas. *Physical Review E* **59**, 7055–7067 (1999). URL https://doi.org/10.1103/physreve.59.7055.

[164] Khrapak, S. A., Ivlev, A. V., Morfill, G. E. & Thomas, H. M. Ion drag force in complex plasmas. *Physical Review E* **66**, 046414 (2002). URL https://doi.org/10.1103/physreve.66.046414.

[165] Lipaev, A. M. *et al.* Void closure in complex plasmas under microgravity conditions. *Physical Review Letters* **98**, 265006 (2007). URL https://doi.org/10.1103/physrevlett.98.265006.

[166] Law, D. A., Steel, W. H., Annaratone, B. M. & Allen, J. E. Probe-induced particle circulation in a plasma crystal. *Physical Review Letters* **80**, 4189–4192 (1998). URL https://doi.org/10.1103/PhysRevLett.80.4189.

[167] Thompson, C. O., D'Angelo, N. & Merlino, R. L. The interaction of stationary and moving objects with dusty plasmas. *Phys. Plasma* **6**, 1421 (1999). URL https://doi.org/10.1063/1.873392.

[168] Samsonov, D., Ivlev, A. V., Morfill, G. E. & Goree, J. Long-range attractive and repulsive forces in a two-dimensional complex (dusty) plasma. *Physical Review E* **63**, 025401(R) (2001). URL https://doi.org/10.1103/PhysRevE.63.025401.

[169] Thomas, Jr., E., Avinash, K. & Merlino, R. L. Probe induced voids in a dusty plasma. *Phys. Plasmas* **11**, 1770–1774 (2004). URL https://doi.org/10.1063/1.1688333.

[170] Klindworth, M., Arp, O. & Piel, A. Langmuir probe system for dusty plasmas under microgravity. *Rev. Sci. Instrum.* **78**, 033502 (2007). URL https://doi.org/10.1063/1.2714036.

[171] Harris, B. J., Matthews, L. S. & Hyde, T. W. Dusty plasma cavities: probe-induced and natural. *Physical Review E* **91**, 063105 (2015). URL https://doi.org/10.1103/PhysRevE.91.063105.

[172] Schwabe, M. *et al.* Observation of metallic sphere - complex plasma interactions in microgravity. *New J. Phys.* **19**, 103019 (2017). URL https://doi.org/10.1088/1367-2630/aa868c.

[173] Khrapak, S. *et al.* Theory of a cavity around a large floating sphere in complex (dusty) plasma. *Physical Review E* **99**, 053210 (2019). URL https://doi.org/10.1103/physreve.99.053210.

[174] Joshi, E. *et al.* Formation of droplets in weightless complex plasmas. *Contributions to Plasma Physics* **61**, e202100081 (2021). URL https://doi.org/10.1002/ctpp.202100081.

[175] Mitic, S. *et al.* Convective dust clouds driven by thermal creep in a complex plasma. *Physical Review Letters* **101**, 235001 (2008). URL https://doi.org/10.1103/PhysRevLett.101.235001.

[176] Schwabe, M. *et al.* Convection in a dusty radio-frequency plasma under the influence of a thermal gradient. *New J. Phys.* **13**, 083034 (2011). URL https://doi.org/10.1088/1367-2630/13/8/083034.

[177] Booth, J. P., Cunge, G., Sadeghi, N. & Boswell, R. W. The transition from symmetric to asymmetric discharges in pulsed 13.56 mhz capacitively coupled plasmas. *Journal of Applied Physics* **82**, 552–560 (1997). URL https://doi.org/10.1063/1.365614.

[178] Verboncoeur, J. P., Langdon, A. B. & Gladd, N. T. An object-oriented electromagnetic PIC code. *Computer Physics Communications* **87**, 199–211 (1995). URL https://doi.org/10.1016/0010-4655(94)00173-Y. Provided by the SAO/NASA Astrophysics Data System.

[179] Lieberman, M. & Lichtenberg, A. *Principles of Plasma Discharges and Materials Processing* (Wiley, 2005). URL https://doi.org/10.1002/0471724254.

[180] Yaroshenko, V. V. *et al.* Measurements of the dust-ion momentum transfer frequency and ion drag force in complex plasmas. *Contributions to Plasma Physics* **45**, 223–228 (2005). URL https://doi.org/10.1002/ctpp.200510024.

[181] Yaroshenko, V. *et al.* Determination of the ion-drag force in a complex plasma. *Physics of Plasmas* **12** (2005). URL https://doi.org/10.1063/1.1947027. 093503.

[182] Haakonsen, C. B. & Hutchinson, I. H. Ion Collection by a Sphere in a Drifting Collisional Plasma. *AIP Conference Proceedings* **1397**, 269–270 (2011). URL https://doi.org/10.1063/1.3659797.

[183] Hirt, M., Block, D. & Piel, A. Measurement of the ion drag force on free falling microspheres in a plasma. *Physics of Plasmas* **11**, 5690–5696 (2004). URL https://doi.org/10.1063/1.1809642.

[184] Lifshitz, E. & Pitaevskii, L. *Physical Kinetics: Volume 10*. Course of theoretical physics (Elsevier Science, 1981).

[185] Khrapak, S. A. & Morfill, G. E. Dusty plasmas in a constant electric field: Role of the electron drag force. *Physical Review E* **69**, 066411 (2004). URL https://doi.org/10.1103/physreve.69.066411.

[186] Cravero, C. & Marsano, D. Computational investigation of the aerodynamics of a wheel installed on a race car with a multi-element front wing. *Fluids* **7** (2022). URL https://doi.org/10.3390/fluids7060182.

[187] Hayashida, H. & Iwasa, Y. Aerodynamic shape effects of tall building for vortex induced vibration. *Journal of Wind Engineering and Industrial Aerodynamics* **33**, 237–242 (1990). URL https://doi.org/10.1016/0167-6105(90)90039-F.

[188] Kawai, H. Vortex induced vibration of tall buildings. *Journal of Wind Engineering and Industrial Aerodynamics* **41**, 117–128 (1992). URL https://doi.org/10.1016/0167-6105(92)90399-U.

[189] Wang, S.-y., Tian, F.-b., Jia, L.-b., Lu, X.-y. & Yin, X.-z. Secondary vortex street in the wake of two tandem circular cylinders at low reynolds number. *Physical Review E* **81**, 036305 (2010). URL https://doi.org/10.1103/PhysRevE.81.036305.

[190] Ku, D. N. Blood flow in arteries. *Annual Review of Fluid Mechanics* **29**, 399–434 (1997). URL https://doi.org/10.1146/annurev.fluid.29.1.399.

[191] Joshi, E., Thoma, M. H. & Schwabe, M. Particle-resolved study of the onset of turbulence (2023). URL https://doi.org/10.48550/arXiv.2306.07711. Accepted for publication in PRResearch., 2306.07711.

[192] Epstein, P. S. On the resistance experienced by spheres in their motion through gases. *Physical Review* **23**, 710–733 (1924). URL https://doi.org/10.1103/PhysRev.23.710.

[193] Meyer, J. K., Merlino, R. L., Heinrich, J. R. & Kim, S.-H. Flow of dusty plasma around an obstacle. *IEEE Transactions on Plasma Science* **42**, 2690–2691 (2014). URL https://doi.org/10.1109/TPS.2014.2302374.

[194] Jaiswal, S., Schwabe, M., Sen, A. & Bandyopadhyay, P. Experimental investigation of dynamical structures formed due to a complex plasma flowing past an obstacle. *Physics of Plasmas* **25**, 093703 (2018). URL https://doi.org/10.1063/1.5042497.

[195] Bailung, Y. *et al.* Vortex formation in a strongly coupled dusty plasma flow past an obstacle. *Physics of Plasmas* **27**, 123702 (2020). URL https://doi.org/10.1063/5.0022356.

[196] Samsonov, D. *et al.* Mach cones in a coulomb lattice and a dusty plasma. *Physical Review Letters* **83**, 3649–3652 (1999). URL https://doi.org/10.1103/PhysRevLett.83.3649.

[197] Melzer, A., Nunomura, S., Samsonov, D., Ma, Z. & Goree, J. Laser-excited mach cones in a dusty plasma crystal. *Physical Review E* **62**, 4162–4176 (2000). URL https://doi.org/10.1103/PhysRevE.62.4162.

[198] Mackey, J., Mohamed, S., Neilson, H. R., Langer, N. & Meyer, D. M.-A. Double bow shocks around young, runaway red supergiants: Application to betelgeuse. *The Astrophysical Journal Letters* **751**, L10 (2012). URL https://dx.doi.org/10.1088/2041-8205/751/1/L10.

[199] Kobulnicky, H. A., Lundquist, M. J., Bhattacharjee, A. & Kerton, C. R. Iras 03063+5735: A bowshock nebula powered by an early b star. *The Astronomical Journal* **143**, 71 (2012). URL https://dx.doi.org/10.1088/0004-6256/143/3/71.

[200] Henney, W. J. & Arthur, S. J. Bow shocks, bow waves, and dust waves – III. Diagnostics. *Monthly Notices of the Royal Astronomical Society* **489**, 2142–2158 (2019). URL https://doi.org/10.1093/mnras/stz2283.

[201] Zhang, H., Fey, U., Noack, B. R., König, M. & Eckelmann, H. On the transition of the cylinder wake. *Physics of Fluids* **7**, 779–794 (1995). URL https://doi.org/10.1063/1.868601.

[202] Dynnikova, G. Y., Dynnikov, Y. A. & Guvernyuk, S. V. Mechanism underlying kármán vortex street breakdown preceding secondary vortex street formation. *Physics of Fluids* **28**, 054101 (2016). URL https://doi.org/10.1063/1.4947449.

[203] Haakonsen, C. B. & Hutchinson, I. H. The electron forewake: Shadowing and drift-energization as flowing magnetized plasma encounters an obstacle. *Physics of Plasmas* **22**, 102103 (2015). URL https://doi.org/10.1063/1.4932006.

[204] Groisman, A. & Steinberg, V. Elastic turbulence in a polymer solution flow. *Nature* **405**, 53–55 (2000). URL https://doi.org/10.1038/35011019.

[205] Mathieu, J. & Scott, J. *An Introduction to Turbulent Flow* (Cambridge University Press, 2000). URL https://doi.org/10.1017/CBO9781316529850.

[206] Nazarenko, S. *Wave Turbulence as a Part of General Turbulence Theory*, 17–28 (Springer Berlin Heidelberg, Berlin, Heidelberg, 2011). URL https://doi.org/10.1007/978-3-642-15942-8_2.

[207] Eckhardt, B., Schneider, T. M., Hof, B. & Westerweel, J. Turbulence transition in pipe flow. *Annual Review of Fluid Mechanics* **39**, 447–468 (2007). URL https://doi.org/10.1146/annurev.fluid.39.050905.110308.

[208] Joshi, E., Pustylnik, M. Y., Thoma, M. H., Thomas, H. M. & Schwabe, M. Recrystallization in string-fluid complex plasmas. *Physical Review Research* **5**, L012030 (2023). URL https://doi.org/10.1103/PhysRevResearch.5.L012030.

[209] Knapek, C., Samsonov, D., Zhdanov, S., Konopka, U. & Morfill, G. E. Structural properties and melting of 2d-plasma crystals. *AIP Conference Proceedings* **799**, 231–234 (2005). URL https://doi.org/10.1063/1.2134607.

[210] Knapek, C. A., Samsonov, D., Zhdanov, S., Konopka, U. & Morfill, G. E. Recrystallization of a 2d plasma crystal. *Physical Review Letters* **98**, 015004 (2007). URL https://doi.org/10.1103/PhysRevLett.98.015004.

[211] Nosenko, V., Zhdanov, S. K., Ivlev, A. V., Knapek, C. A. & Morfill, G. E. 2d melting of plasma crystals: Equilibrium and nonequilibrium regimes. *Physical Review Letters* **103**, 015001 (2009). URL https://doi.org/10.1103/PhysRevLett.103.015001.

[212] Joshi, E. Data for paper 'Recrystallization in String-Fluid Complex Plasmas' (2022). URL https://doi.org/10.5281/zenodo.5871983.

[213] Sukhinin, G. I., Fedoseev, A. V., Antipov, S. N., Petrov, O. F. & Fortov, V. E. Dust particle radial confinement in a dc glow discharge. *Physical Review E* **87**, 013101 (2013). URL https://doi.org/10.1103/PhysRevE.87.013101.

[214] Sukhinin, G. I. *et al.* Influence of ion drag force on radial distribution of dust particles and void formation in a dc glow discharge. *Europhysics Letters* **103**, 35001 (2013). URL https://dx.doi.org/10.1209/0295-5075/103/35001.

[215] Pustylnik, M. *et al.* Physical aspects of dust–plasma interactions. *Contributions to Plasma Physics* **61**, e202100126 (2021). URL https://doi.org/10.1002/ctpp.202100126.

[216] Ludwig, P., Kählert, H. & Bonitz, M. Ion-streaming induced order transition in three-dimensional dust clusters. *Plasma Physics and Controlled Fusion* **54**, 045011 (2012). URL https://dx.doi.org/10.1088/0741-3335/54/4/045011.

[217] Hutchinson, I. H. Intergrain forces in low-mach-number plasma wakes. *Physical Review E* **85**, 066409 (2012). URL https://doi.org/10.1103/PhysRevE.85.066409.

[218] Ivlev, A. V. *et al.* Decharging of complex plasmas: First kinetic observations. *Physical Review Letters* **90**, 055003 (2003). URL https://doi.org/10.1103/PhysRevLett.90.055003.

[219] Wörner, L. *et al.* The effect of a direct current field on the microparticle charge in the plasma afterglow. *Physics of Plasmas* **20**, 123702 (2013). URL https://doi.org/10.1063/1.4843855.

[220] Vaulina, O. S. & Vladimirov, S. V. Diffusion and dynamics of macro-particles in a complex plasma. *Physics of Plasmas* **9**, 835–840 (2002). URL https://doi.org/10.1063/1.1449888.

[221] Dzhumagulova, K. N., Ramazanov, T. S. & Masheeva, R. U. Velocity autocorrelation functions and diffusion coefficient of dusty component in complex plasmas. *Contributions to Plasma Physics* **52**, 182–185 (2012). URL https://doi.org/10.1002/ctpp.201100070.

[222] Kretschmer, M. & Thoma, M. H. personal communication (13/07/2023). We discussed continuing this work and publishing the experimental and numerical results together after the submission of this thesis.

Acknowledgements

There are a lot of people without whom this work would not be possible. Words cannot convey how grateful and thankful I am to all of you, but I'll give it a try anyway.

First of all, I would like to thank my family for their unwavering support - especially my mother, who worked much harder than me just to get me through school. Papa, thank you for the pride and joy you feel towards me. I love you both, and would not be who I am today without you.

I would like to thank Dr. Mierk Schwabe for giving me the opportunity to do this work and for believing in my capability, sometimes more than I did. I will miss our weekly calls! Thank you for the emotional as well as academic support! It really means a lot.

I would also like to thank Dr. Hubertus Thomas and Prof. Dr. Markus Thoma for their continued support throughout the years. I am very grateful to all three of you for reading my thesis and for all the advice you have given me.

My thanks also to Dr. Philip Born for the helpful comments and cheerful support throughout the years, specially for advising and reviewing my publications. Many thanks also to Dr. Andrey Lipaev and his team (Sasha, Roman, Andrey) without whose kindness and understanding the work discussed in this thesis would not have been published.

I also want to thank my colleagues at DLR, and I wish we had more time together. I owe Dr. Peter Huber and Dr. Daniel Mohr for a lot of their help with computing and getting me started. I have a lot of gratitude toward Dr. Mikhail Pustylnik for many scientific discussions and help and support. Thank you also for reading parts of my thesis! I thank Dr. Christina Knapek, Dr. Sergey Khrapak, Dr. Michael Kretschmer, Dr. Volodymyr Nosenko, and Dr. Alexei Ivlev for the advice and guidance you have provided me. Thanks also to my fellow PhD students, Prapti and Sasha, for their support outside of work. The short amount of time we shared together in the office was very nice!

I am also grateful to DLR for funding this work in the framework of the Nachwuchsgruppenprogramm im DLR-Geschäftsbereich Raumfahrt.

Finally, I would like to thank my friends for fostering a wholesome and supportive environment and always having my back. I would like to especially thank Daniel for everything that you did for me. I really relied on you in all aspects of life and you went above and beyond every time.

I thank you all from the bottom of my heart.

Index

édition scientifique
VVB LAUFERSWEILER VERLAG

VVB LAUFERSWEILER VERLAG
STAUFENBERGRING 15
D-35396 GIESSEN

Tel: 0641-5599888 Fax: -5599890
redaktion@doktorverlag.de
www.doktorverlag.de

ISBN: 978 3 8359 7171 4

Photo cover: Van Gogh - Starry Night @ Google Art Project Wikipedia.com